Scientifica
2014

LUIGI MALAVOLTI

Single molecule magnets sublimated on conducting and magnetic substrates

PREMIO TESI DOTTORATO
FIRENZE UNIVERSITY PRESS – UNIVERSITÀ DEGLI STUDI DI FIRENZE

FIRENZE UNIVERSITY PRESS

PREMIO TESI DI DOTTORATO

Commissione giudicatrice, anno 2014

Luigi Lotti, *presidente della Commissione*

Tito Arecchi, *Area scientifica*
Aldo Bompani, *Area Scienze Sociali*
Franco Cambi, *Area Umanistica*
Paolo Felli, *Area Tecnologica*
Michele Arcangelo Feo, *Area Umanistica*
Roberto Genesio, *Area Tecnologica*
Mario Pio Marzocchi, *Area Scientifica*
Adolfo Pazzagli, *Area Biomedica*
Giuliano Pinto, *Area Umanistica*
Salvatore Ruggieri, *Area Biomedica*
Saulo Sirigatti, *Area Biomedica*
Fiorenzo Cesare Ugolini, *Area Tecnologica*
Vincenzo Varano, *Area Scienze Sociali*
Graziella Vescovini, *Area Umanistica*

Luigi Malavolti

Single molecule magnets sublimated on conducting and magnetic substrates

Firenze University Press
2015

Single molecule magnets sublimated on conducting and magnetic substrates / Luigi Malavolti. – Firenze : Firenze University Press, 2015.
(Premio Tesi di Dottorato; 50)

http://digital.casalini.it/9788866559702

ISBN 978-88-6655-969-6 (print)
ISBN 978-88-6655-970-2 (online)

Peer Review Process
All publications are submitted to an external refereeing process under the responsibility of the FUP Editorial Board and the Scientific Committees of the individual series. The works published in the FUP catalogue are evaluated and approved by the Editorial Board of the publishing house. For a more detailed description of the refereeing process we refer to the official documents published on the website and in the online catalogue of the FUP (www.fupress.com).

Università degli Studi di Firenze
Firenze University Press
Borgo Albizi, 28, 50122 Firenze, Italy
www.fupress.com
Printed in Italy

A Donatella,
alla mia famiglia

"Beyond the horizon of the place we lived when we were
young In a world of magnets and miracles
Our thoughts strayed constantly and without boundary The
ringing of the division bell had begun ..."

"High Hopes", Pink Floyd

Index

Luigi Malavolti, *Single molecule magnets sublimated on conducting and magnetic substrates*,
ISBN 978-88-6655-969-6 (print) ISBN 978-88-6655-970-2 (online)

Section 1
Introduction

Molecular magnetism is an interdisciplinary research field where chemists and physicists work together to design and characterise the magnetic properties of molecular based materials. Among these a central role is played by the so called Single Molecule Magnets (SMMs) (Gatteschi et al. 2006). The evocative name derives from the magnetic property of these molecular systems, which behave as tiny magnets. They are characterised, albeit at cryogenic temperatures, by slow relaxation of the magnetisation, which is molecular in origin (Gatteschi et al. 2006). This behaviour arises from a ground state characterised by the coexistence of two different states separated by an energy barrier; a property known as magnetic bistability. Moreover, the molecular nature leads to the observation of quantum effects in static and dynamic magnetic properties (Gatteschi et al. 2006). SMMs combine the advantages of the molecular scale with the properties of bulk magnetic materials. This makes them attractive, though still at a fundamental level due to low operational temperatures, for high-density information storage, for quantum computing (Leuenberger & Loss 2001; Troiani et al. 2005; Lehmann et al. 2007) and for spintronic applications (Bogani & Wernsdorfer 2008). In the latter research field the electronic and spin degrees of freedom are exploited for technological purposes (Dediu et al. 2009; Bogani & Wernsdorfer 2008; Sanvito 2011; Katoh, Isshiki, et al. 2012).

In order to explore the possibilities offered by SMMs it is mandatory to achieve the control of the magnetic state at the single molecule level. This is typically achieved by creating hybrid nano-architectures, i.e. SMM on a conducting surface or inserted in a nano-gap between electrodes. For this reason in the last decade many efforts have been devoted to prepare and characterise SMMs hybrid surfaces (Cornia et al. 2011). As demonstrated by the first attempts based on the archetypal SMM, a dodecanuclear manganese complex (Mn_{12}) (S. Voss et al. 2008; Mannini et al. 2008), the preparation of such a hybrid surfaces has proved to be a critical issue. In fact, due to structural modifications induced by the substrate, the Mn_{12} molecules lose their SMM behaviour. To overcome such problems more stable SMMs are needed, requir-

Luigi Malavolti, *Single molecule magnets sublimated on conducting and magnetic substrates*,
ISBN 978-88-6655-969-6 (print) ISBN 978-88-6655-970-2 (online)

ing synthetic efforts, as well as a fine control of the deposition method, a task that necessitates competences in surface-science. This work is indeed devoted to the surface-science aspect.

The first relevant result in the preparation of a SMM hybrid surface was achieved by employing a chemical grafting method for the molecular deposition (Mannini et al. 2009). However, this surface preparation requires a specific molecular moiety able to bind the surface. This represents a limitation because it does not allow the functionalization of different surfaces using the same molecule. Moreover, the preparation from solution do not allow a fine control of the surface quality. This hampers the possibility to address the single molecule properties by employing Scanning Tunnelling Microscopy (STM) and its derived techniques. In order to be able to exploit the great potentiality of these techniques, recently demonstrated in the investigation of atomic structures on surfaces (Loth, von Bergmann, et al. 2010; Hirjibehedin et al. 2006; Hirjibehedin et al. 2007; Khajetoorians et al. 2011; Serrate et al. 2010; Loth et al. 2012), other deposition methods must be employed, such as the electrospray beam deposition, employed by Kern's group (Rauschenbach et al. 2009; Kahle et al. 2012), and the more traditional molecular sublimation method. In fact, both methods allow the preparation of the surfaces employing the ultimate controlled conditions provided by the Ultra-High Vacuum (UHV) environment (pressure $< 10^{-10}$ mbar). These methods overcome also the substrate limitation of the chemical grafting procedure allowing the preparation of different hybrid surfaces by using the same SMM. Moreover, highly reactive surfaces, like ferromagnetic 3d metals, can be employed. However, the sublimation procedure requires a high thermal stability of the single molecule magnet that strongly reduces the number of SMMs suitable for this method.

In this work we present a study concerning two sublimable molecular systems. We start by presenting the results of our investigation on one of the most studied class of SMMs: the rare earth ions bis(phthalocyaninato) complexes (Ishikawa et al. 2003). In particular the terbium(III) bis(phathalocyaninato) ($TbPc_2$) has been considered the archetypal of sublimable SMMs. It exhibits slow relaxation of the magnetisation at temperatures as high as 15 K, which is remarkable for a SMM. Due to its flat structure the $TbPc_2$ molecule has proven to be a good candidate for STM and Scanning Tunnelling Spectroscopy (STS) investigations (Schwöbel et al. 2012; Fu et al. 2012; Komeda et al. 2011; Katoh et al. 2009). These studies have provided crucial information about the electron transport properties of the $TbPc_2$ SMM (Katoh, Isshiki, et al. 2012). A keen interest has been also focused on the characterization of hybrid architectures made by magnetic molecules deposited on magnetic substrates (Lodi Rizzini et al. 2011; Lodi Rizzini et al. 2012; Klar et al. 2013). The presence of molecule-substrate magnetic interactions could indeed open new perspectives for

spintronics and data storage applications. Albeit the consistent number of publications on this SMM, some issues concerning its magnetic behaviour when organized in nanostructures, like the strong reduction of its magnetic hysteresis when deposited on conducting substrates, are still open and have been the object of this thesis.

The other SMM investigated here belongs to the Fe_4 SMM class. It has been recently shown that a particular derivative of this family can be sublimated (Margheriti et al. 2009). However, also due to the intrinsic difficulties related to the very low blocking temperature (below 1 K), an accurate picture of the magnetic and structural properties of sublimated Fe_4 hybrid surfaces is still lacking. This despite the fact that in the last years the Fe_4 family has proven to be a good model system for the rationalization of the relationship between the magnetic properties and the chemical structure (Accorsi et al. 2006).

The Fe_4 molecules are robust and chemically stable. They can be chemically functionalised with different moieties to promote the interaction with surfaces or to introduce functionalities able to promote a photomodulation of the magnetic properties (Prasad et al. 2012). Moreover, the magnetic properties of the Fe_4 molecules are less influenced by intermolecular interactions (Schlegel et al. 2010) than the $TbPc_2$ class. This has also allowed to observe in monolayer films the molecular magnetic bistability and the quantum phenomena characterising this SMM, such as the tunnelling of the magnetisation.

In this work we present the results of our study of the two molecular systems mentioned above. Section 3 is devoted to the investigation of the magnetic behaviour of $TbPc_2$ and the correlation of its hysteretic behaviour with the surrounding environment. In particular we focus our attention on the hysteretic loops of $TbPc_2$ molecule during the sublimation process, highlighting some anomalies. In order to shed some light on this phenomenon, in paragraph 3.3 we present the results obtained by exploiting the low energy muons implantation technique to perform depth-resolved investigations of the magnetic properties of $TbPc_2$ thick films. In the last part of section 3 (paragraph 3.4) we report a characterisation of thin films of $TbPc_2$ sublimated on two magnetic substrates, namely lanthanium-strontium manganite and metallic cobalt. Our choice has fallen on these two substrates because they are the most employed ferromagnetic substrates for the realisation of electrodes in organic spin valve (Dediu et al. 2009), thus preparing the ground for future applications.

Section 4 is dedicated to the investigation of hybrid surfaces prepared by sublimation of Fe_4 SMMs. We exploit the UHV techniques to perform a Photoelectron characterisation of Fe_4 deposited on Au(111) surface (section 4 paragraph 4.2). The PhotoElectron Spectroscopy (PES) investigation has allowed to tune the preparation of the hybrid surfaces getting sub-monolayer Fe_4 coverage. This has allowed to investigate low coverage Fe_4 samples on different surfaces by means of STM tech-

niques. Thanks to the effort in the optimization of the preparation procedure and the in depth characterisation of our films it has been possible to perform experiments in one of the most performing STM platform to record inelastic electron tunnelling spectra. This technique is one of the few that allow the investigation of the electronic and magnetic properties of molecules on surface at the single molecule level.

Section 2
Experimental methods

1 Bulk magnetic characterisation

The magnetic characterisation of bulk materials was performed by employing standard magnetometers. These instruments allow the measurement of the magnetisation and the susceptibility of the samples. The susceptibility χ is a second rank tensor which is defined as:

$$\chi = \frac{\delta M}{\delta H} \qquad (1)$$

where M is the molar magnetisation of the sample and H is the magnetic field vector. The susceptibility characterises the interaction of the magnetic moment of the samples with the external magnetic field. By looking at the molecular scale, the magnetic moment can be described as the energy variation of the molecular system (δE) due to the interaction with the magnetic field. The magnetic moment m is defined as:

$$m = -\frac{\delta E}{\delta H} \quad (2)$$

Considering a system characterised by an energy spectrum of n levels E_n(n =1,2,..,n) and introducing the Boltzmann distribution law, the macroscopic magnetisation can be written as:

$$M = \frac{N \sum_n (-\delta E_n/\delta H) exp(-E_n/kT)}{\sum_n exp(-E_n/kT)} \qquad (3)$$

where T is the temperature in K units and k is the Boltzmann constant. This is the general formula which directly relates the energy levels description of the system to its macroscopic magnetic properties.

Luigi Malavolti, *Single molecule magnets sublimated on conducting and magnetic substrates*,
ISBN 978-88-6655-969-6 (print) ISBN 978-88-6655-970-2 (online)

The measurement of magnetisation can be carried out by employing standard magnetometry techniques while for a correct evaluation of the susceptibility the use of alternating magnetic fields is required. These techniques are described in the following paragraphs.

1.1 Standard magnetometry

Most magnetometers are based on the inductive detection. These instruments work with static magnetic field generated by a superconductive magnet. The magnetic flux variation induced by the presence of the sample inside a coil is measured. The flux variation produces in the coil an electromotive force proportional to $-\delta\phi/\delta t$, where ϕ is the magnetic flux through the detection loops. In the coil circuit this generates a current that can be measured. To induce a time change of ϕ the magnetised sample is moved inside the detection coils in a region of homogenous magnetic field. During the measurements the sample is thus assembled on a rod and is moved inside a gradiometer circuit. This circuit is sensitive only to a variation of the gradient of the magnetic field and allows to separate the contribution of the sample from the drift of the homogenous field. In particular, the second order gradiometer circuit employed in our instruments is formed by three coils, a single coil with N windings placed between two coils made of N/2 windings each and wound in the opposite direction (see fig. 1 left). The sample is moved from the centre of the top coil to the centre of the bottom coil. The current induced in the gradiometer circuit changes sign between opposite coils and the difference is assumed to be proportional to the magnetisation of the sample. The proportionality factor is determined through a calibration with standard samples with well-known magnetisation, like metallic Pt.

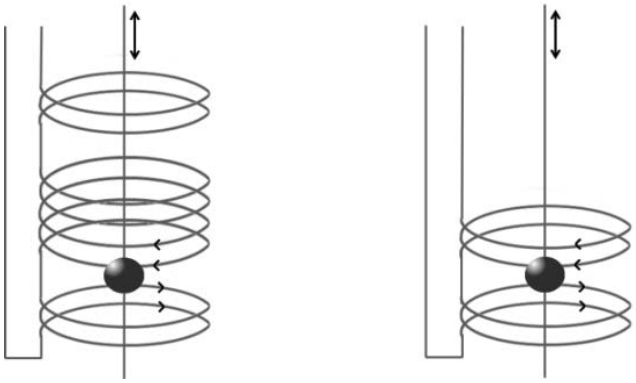

Fig. 1: Schematic representation of a second order gradiometer (left): the windings of the bottom and top coil are wound in the opposite direction respect to windings of the central one. In the magnetic measure the sample is moved up and down inside the gradiometer. A first order gradiometer made by two coils wound in the opposite way (right).

The sensitivity of the system can be enhanced by inductively coupling a Superconductive Quantum Interference Device (SQUID). This device, formed by a superconductive ring with a Josephson junction (Barone & Paternò 1982; Bukel 1991), is the most sensitive detector for the magnetic flux (Clark & Braginski 2004). A comparable, although slightly lower, sensitivity can be reached employing the so called Vibrating Sample Magnetometer (VSM). In this type of magnetometers the sample is moved inside a gradiometer (fig. 1 right) at frequencies in the range of 50-100 Hz. The signal is recorded by means of a lock-in detection system without the necessity of a SQUID. This makes the magnetometer better suited for measurements under fast varying magnetic fields, which would be not compatible with SQUID devices, the latter being very sensitive to the magnetic field. The VSM technique was therefore used to record the magnetic hysteresis presented in section 3 paragraph 2.

It is important to note that these magnetometers measure the magnetisation of the sample. The molar susceptibility χ can be calculated assuming a linear dependence of the magnetisation on the field as:

$$\chi = \frac{M}{N} \cdot H \quad (4)$$

where M is the magnetisation of the sample and N is the number of moles. The assumption of a linear dependence of the magnetisation on the field is not correct under strong magnetic fields. To have access to the susceptibility the so called *ac* susceptometry was employed.

1.2 Ac susceptometry

In these measurements the sample is positioned inside a coil, called primary. A small oscillating magnetic field, few Oe, can be generated by applying an alternate potential to the coil's ends. Inside the coil a first order gradiometer circuit is present, called secondary. Due to the opposite wounding of the two coils no voltage is induced from the primary to the secondary. However, if a sample is inserted in the coils it magnetisation will oscillates with the oscillating field unbalancing the secondary circuit, and generating a voltage that is proportional to the change in sample magnetisation. As the oscillating field is very small, the derivative of the magnetisation *vs.* the oscillating field, i.e. the susceptibility, is directly measured. The sample is moved inside the gradiometer to eliminate possible spurious signal due to a non-perfect balance of the gradiometer's windings.

It is possible to apply a constant field (B_0) along the same direction of the *ac* field. The total field experienced by the sample is thus:

$$B = B_0 + h\cos\omega t \quad (5)$$

where h is the amplitude of the oscillation and ω is the angular frequency of the ac field. Independently from the value of B_0 the oscillating field remains small and thus the susceptibility can be evaluated also for a non-linear dependence of the magnetisation on the applied field.

The application of a tuneable *ac* field allows the study of the dynamic properties of the investigated sample by varying the angular frequency of the field. The magnetisation of the sample experiencing the *ac* field can be described as:

$$M(t) = M_0 + \chi(t)h \quad (6)$$

It is convenient to describe the susceptibility as formed by a real, χ', and imaginary part, χ''. Thus $\chi(t)$ is:

$$\chi(t) = \chi'\cos\omega t + \chi''\sin\omega t \quad (7)$$

the magnetisation is then calculated as:

$$M(t) = M_0 + (\chi'\cos\omega t + \chi''\sin\omega t)h \quad (8)$$

The measurement of the two components can be achieved by using a lock-in detection. The relative value of the two components is determined by the dynamic properties of the investigated material in respect to the employed oscillation frequency. Defining τ as the time needed for a magnetic system to establish the thermal equilibrium in the oscillating field, two limiting cases can be encountered. If the frequency is slow comparing to the relaxation rate $\tau^{-1}(\omega\tau \ll 1)$ the magnetisation of the system is able to follow the oscillating field and no signal will be detected in the quadrature channel. The measured susceptibility is the isothermal one defined as χ_T. On the contrary when the frequency is fast comparing to τ^{-1} $(\omega\tau \gg 1)$ the susceptibility measured is the adiabatic susceptibility, χ_S. In this case the system has no time to exchange energy with surrounding environment. For intermediate ratios between omega and τ^{-1} Casimir and Du Pré (H B G Casimir & du Pré 1938) proposed the following formulae for the definition of the imaginary and real part of the susceptibility:

$$\chi' = \frac{\chi_T - \chi_S}{1+\omega^2\tau^2} + \chi_S \quad (9)$$

$$\chi'' = \frac{(\chi_T - \chi_S)\omega\tau}{1+\omega^2\tau^2} \quad (10)$$

For a system characterised by a distribution of relaxation times the two components of the susceptibility can be calculated as (Cole & Cole 1941):

$$\chi'(\omega) = \chi_S + (\chi_T - \chi_S)\frac{1+(\omega\tau)^{1-\alpha}\sin(\pi\alpha/2)}{1+2(\omega\tau)^{1-\alpha}\sin(\pi\alpha/2)+(\omega\tau)^{2-2\alpha}} \qquad (11)$$

$$\chi''(\omega) = (\chi_T - \chi_S)\frac{1+(\omega\tau)^{1-\alpha}\cos(\pi\alpha/2)}{1+2(\omega\tau)^{1-\alpha}\sin(\pi\alpha/2)+(\omega\tau)^{2-2\alpha}} \qquad (12)$$

where the phenomenological parameter α accounts for the distribution of relaxation times, the higher is α the wider is the distribution. By fitting the frequency dependence of the imaginary susceptibility with equation 12 the relaxation time τ and the α parameter can be evaluated. The procedure can also be repeated on χ', although this one does not show a peak feature. By repeating the measurements at different temperature it is possible to investigate the temperature dependence of the two parameters, τ and α. The same analysis can be repeated for different applied static fields. These studies are crucial for the investigation of the slow relaxation processes of SMM systems.

2 Sublimation process

One of the most clean techniques for the molecular deposition is the molecular sublimation in Ultra-High Vacuum (UHV) environment (pressure of the order of 10^{-10} mbar). The UHV, indeed, allows to prepare clean surfaces by means of sputtering and annealing. Our home-made experimental setup for the sublimation process is illustrated in fig. 2. The powder of the molecular compound fills a quartz crucible housed in the turns of a tantalum wire. By means of Joule effect the crucible can be heated up controlling the temperature by a K type thermocouple immersed in the molecular powder. The heating process is controlled by regulating the current flowing in the tantalum wire by means of an adjustable power supply. The sublimation system is assembled on CF40 feedthrough and it can be assembled in UHV systems. The film preparation is thus achieved by heating up the powder to the sublimation temperature while the sample surface is directly exposed to the incoming flux of molecules.

In order to exploit this process the molecules must be stable to thermal treatment. This is a quite restrictive prerequisite which, for example, limited the study of the Mn_{12} class of SMMs (S. Voss et al. 2008; Mannini et al. 2008). However, as anticipated in section 1, other SMMs are stable enough to be sublimated in UHV, as in the case of the $TbPc_2$ (Margheriti et al. 2010) and Fe_4Ph (Margheriti et al. 2009). One

of the most important advantages of the sublimation process, if compared to solution techniques, is certainly related to its cleanliness, which allows the best exploitation of scanning probe microscopy and related techniques. The possibility to deposit the same molecule on different substrates, including artificial structures not stable in ambient conditions, and the capability of controlling the amount of deposited molecules, are other relevant advantages of this UHV-based preparation technique. In particular in this work we exploited the versatility of the sublimation process to study $TbPc_2$ and Fe_4Ph SMMs on different substrates.

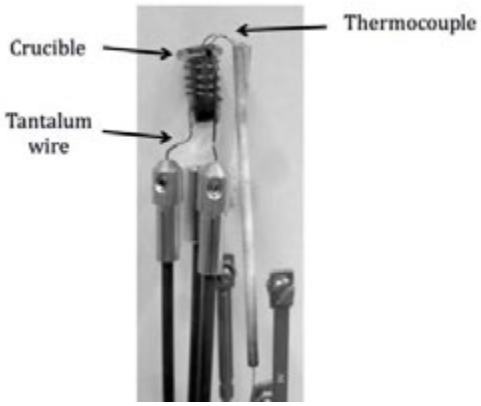

Fig. 2: Picture of the home built sublimating system.

3 Quartz Crystal Microbalance

The Quartz Crystal Microbalance (QCM) is a useful tool for checking the molecular flux during the sublimation process. The sensor, made by a quartz crystal, detects small amounts of sublimated material on its surface by measuring the frequency variation of the crystal resonant oscillation. The relation between the mass of the deposited film and the frequency variation is:

$$\Delta s = \frac{K}{\rho \cdot z \cdot f_c} \tan^{-1}\left\{ z \tan\left[\frac{\pi (f_q - f_c)}{f_q} \right] \right\} \qquad (13)$$

where Δs and ρ are the thickness and the density of the deposited material respectively, f_c and f_q are the frequency before and after the deposition, respectively, and K is a constant including quartz crystal parameters; z is the so called z-factor which is tabulated for many materials, in our experiments we used the value of the graphite.

4 PhotoElectron Spectroscopy (PES)

The chemical characterisation of the sublimated films on conductive substrates can be performed by employing the photoemission technique. The technique is based on the photoemission effect, which was discovered by H. Hertz in the 1887. The effect was then rationalized in the following years by Einstein (1905) (Einstein 1905) and its application in spectroscopic studies was developed only in the '50s and '60s. The technique was refined during the last 60 years to achieve the actual state of the art.

The photoemission effect takes place when a photon transfers enough energy to an electron to overcome the potential barrier (binding energy) holding it to its atom. The exceeding energy imparted by the photon manifests as kinetic energy of the electron. Thus knowing the photon energy ($h\upsilon$) and the kinetic energy (E_{Kin}) of the photoelectron it's possible to calculate the binding energy (E_B) using the following formula:

$$E_B = h\upsilon - E_{Kin} + \phi_{samp.} - \phi_{spec.} \quad (14)$$

where $\phi_{samp.}$ and $\phi_{spec.}$ are respectively the work functions of the sample and the spectrometer (fig. 3). The energy level diagram of the process is depicted in fig. 3 considering the case of a metallic sample electrically connected to the spectrometer and both grounded. This allows for minimising the charging effect maintaining a fixed potential during the photoemission process. The scheme considers a system at 0 K where the Fermi level is the highest occupied energy level. At the equilibrium the sample and the spectrometer have the same Fermi energy due to the electrical contact. When the photoelectron goes from the sample into the spectrometer it feels an accelerating or decelerating potential due to the difference in work function of the two materials ($\phi_{samp.} - \phi_{spec.}$). The work function is defined as the energy difference between the Fermi and the vacuum level and it depends on the material. Although the Fermi levels of the sample and spectrometer are the same they have different work functions. This introduces a shift in the detected kinetic energy of the electrons that must be corrected to be able to compare spectra acquired with different spectrometers.

The PES spectrum is acquired recording the number of electrons detected in function of their kinetic energy. However, since the kinetic energy depends on the radiation energy, the use of the binding energy abscissa is generally preferred. It's important to note that in PES experiments the energy level of the final state is measured, which is lacking one electron, while energy of the initial state can be only obtained by theoretical considerations.

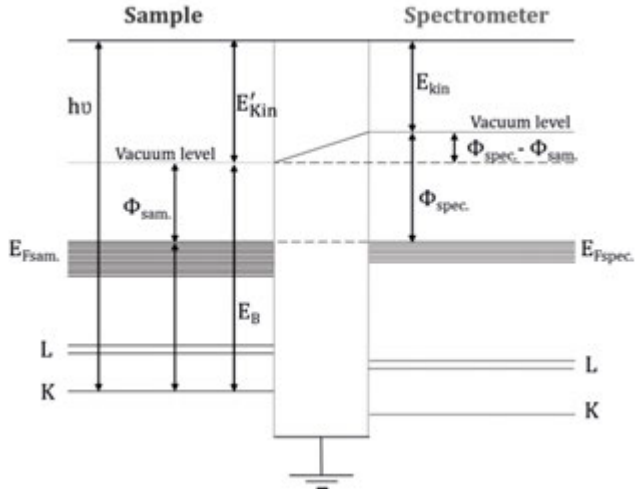

Fig. 3: Sample levels scheme (right) and spectrometer levels (left). The sample and the spectrometer are in direct contact, thus their Fermi energies are equal. When photoelectrons go from the sample to the spectrometer they experience a potential due to the difference of the work functions of the two materials.

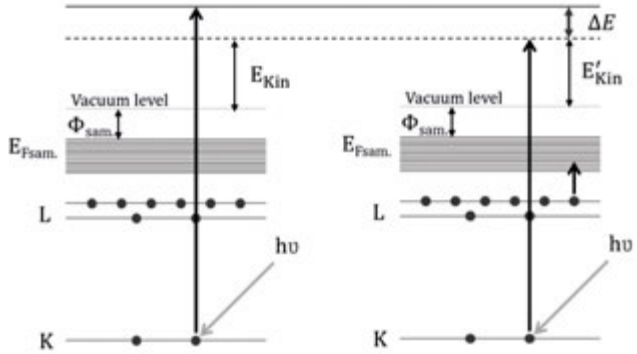

Fig. 4: Scheme of the levels in the description of the shake-up satellite peaks generation; the one electron process (left) and the two electron process (right).

In some cases the photoemission process involves also a transition of a core electron into the valence band. Thus, the final ionised atom is not in its ground state, and the kinetic energy E'_{Kin} of photon resulting from this two electrons process is lower than the expected one (fig. 4) and also depends on the energy of the excited state. It can be calculated as respect to the E_{Kin} of the one electron process as:

$$E'_{Kin} = E_{Kin} - \Delta E \quad (15)$$

which corresponds in binding energy:

$$E'_B = E_B + \Delta E \qquad (16)$$

where ΔE is the energy involved in the transition of the core electron to the valence band. This process leads to discrete structures at higher binding energy side of the main photoelectron peak (shake-up satellite(s)).

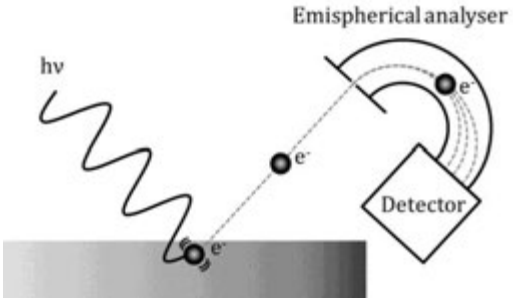

Fig. 5: The photon (hυ) excites the electrons of the sample which are emitted as photoelectrons. The photoelectrons are then separated in energy by means of a hemispherical analyser.

Strong satellite peaks are generally observed in many transition metal and rare earth based compounds. In particular in the XPS spectrum of compounds containing Fe^{3+} ions show strong shake-up satellites (see section 4 paragraphs 3 and 4) and this is an additional feature that can be used to recognise it. Moreover, emitted photoelectrons can leave the sample's surface directly or they can interact with the atoms of the sample before escaping from the surface. The *primary spectrum* is formed by photoelectrons which leave the surface without exchanging energy with the surrounding atoms. The *secondary spectrum* is formed by the photoelectrons which have exchanged energy by means of inelastic scattering processes and it contributes to form a background. The latter ones are labelled as *secondary electrons* and their energy cannot be calculated with equation 14. The scattering processes limit the escape length of the emitted photoelectrons giving rise to one of the more interesting properties of the photoelectron spectroscopy. Photoelectrons with energy >50 eV allow to investigate a thickness of a maximum 50 Å. This feature makes the technique surface sensitive. The short escape length is also the reason for the necessity to work in UHV conditions. The surface sensitivity of the PES technique requires an atomically clean surface. Thus 10^{-10} mbar base pressure is recommended for PES investigations. A schematic representation of the PES experiment is reported in fig. 5.

According to the radiation energy used the photoelectron spectroscopies are classified as X-ray Photoemission Spectroscopy (XPS) and Ultraviolet Photoemission Spectroscopy (UPS).

4.1 X-ray Photoemission Spectroscopy (XPS)

In a XPS experiment the incident photons have energies $100 < h\nu < 1500$ eV; the most common X-ray sources used in a conventional laboratory are the Al Kα (1486.6 eV) and Mg Kα (1253.6 eV). The photon energy is thus enough to promote core electrons into the vacuum continuous level of the investigated samples. As already mentioned, the binding energy of the photoelectrons can be used as fingerprint of the element allowing a chemical analysis of the surface. Each peak is labelled with the corresponding level of the initial state. The photoemission peak associated with an electron ejected from an orbital characterised by $l > 0$ can show a well-defined splitting in two components. The two states derive from the spin-orbit coupling. Accounting for the spin-orbit coupling with the j-j coupling scheme the total angular momentum of each electron is given by $j = l + s$ and the total angular momentum of the whole atom is calculated as $J = \sum j$. Two possible states arise when an electron is ejected from an orbital characterised by $l > 0$. The difference in energy of the two states is due to the parallel or antiparallel alignment of the spin electron and its orbital angular momentum i.e. $j = l \pm 1/2$. This separation for the core shells can be many electron-volts and is another fingerprint of a specific element. The relative intensity of the peaks is given by the ratio of their respective degeneracies $(2j + 1)$. An example of the spin-orbit splitting is reported in fig. 6 for the Au *4f* peak.

The binding energy of the peaks depends also on the electronic density of each atom that is related to the chemical environment, i.e. oxidation state and functional groups present (*chemical shift*). For instance the Fe^{3+}, Fe^{2+} and Fe^{0} *2p* peaks have not the same binding energy: the core electrons of atoms with low electron density (like Fe^{3+}) feel stronger Coulomb interaction respect to a more reduced species (like Fe^{2+}), therefore the energy required for the ionisation process is shifted to higher values. This phenomenon allows for discriminating the oxidation state of each element on the surface. In order to compare the intensity of different XPS peaks the relative atomic photoemission cross-section (σ) must be taken into account. This parameter depends on the atomic initial state and on the photon energy. A complete table of the element photoemission cross-section can be obtained from the web address: http://ulisse.elettra.trieste.it/services/elements/WebElements.html. (Yeh & Lindau 1985; Yeh 1993). The tabulated values have been used in this work for the quantitative interpretation of the XPS spectra. The intensity of each peak can be evaluated by integrating the corresponding area after the subtraction of the inelastic background. This process can be performed by using one of the many available programs which allow the deconvolution of the XPS signal and the background subtraction. The calculated area is then divided by its relative cross section allowing the comparison be-

tween the intensity of the peaks of different elements. In this way it is possible to estimate the surface chemical composition with a typical accuracy of 10 %.

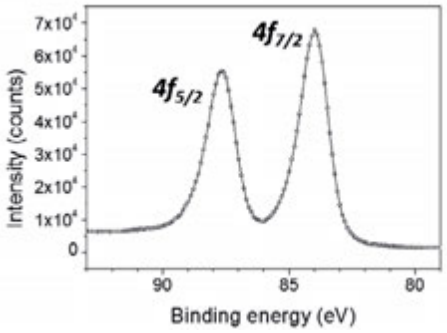

Fig. 6: Spin splitting of the Au *4f* region: the two components $4f_{5/2}$ and $4f_{7/2}$ are separated by 3.67 eV.

The XPS technique is also a useful tool for the estimation of the film thickness. By assuming the system as constituted by a uniform deposit, A, on the substrate surface, B, (fig. 7), and considering the escape length of the photoelectron emitted from the film equal to the escape length of photoelectrons emitted from the substrate, we obtain the following simplified equation:

$$\frac{I'_A}{I'_B} = \frac{N_A\left\{1-exp\left[-d/\lambda_{A,A}cos\theta\right]\right\}}{N_B\left\{exp\left[-d/\lambda_{B,A}cos\theta\right]\right\}} \quad (17)$$

Where $\lambda_{A,A}$ and $\lambda_{B,A}$ are the inelastic mean free paths of the electrons in A (second index letter) emitted by the element A or B (first index letter), and N_A and N_B are the number of atoms constituting the investigated surface portion. The emission angle θ of the electrons is given with respect to the surface normal (polar angle). If the A and B peaks are close in energy is possible to approximate $\lambda_{A,A} \sim \lambda_{B,A} = \lambda$ and write for the layer thickness d:

$$d = \lambda\cos\theta \ln\left(\frac{I'_A N_B}{I'_B N_A} + 1\right) = \lambda\cos\theta \ln\left(\frac{I'_A I_{B\infty}}{I'_B I_{A\infty}} + 1\right) \quad (18)$$

where $I_{A\infty}$ and $I_{B\infty}$ are the intensities of the signals of pure bulk elements A and B. The accuracy in the estimation of d using this equation is affected by the incertitude on N_B/N_A and $I_{B\infty}/I_{A\infty}$. With a good approximation we can assume that $I_{B\infty}$ and $I_{A\infty}$ are equal to the photoionisation cross section of the respective element, while I'_A and I'_B correspond to the intensity of XPS signal. In this case all the parameter of the equation 18 are known allowing the calculation of d thickness. If the

$\lambda_{A,A} \sim \lambda_{B,A} = \lambda$ approximation is not reasonable the equation can be solved numerically introducing the escape length calculated for each element.

In this discussion we have considered only the process involving photoelectrons. However, when the X-ray radiation interacts with the atoms of the surface another process can produce electron emission. This is the case of the Auger process. For the clarity of the discussion we can consider the ionisation of the K shell by means of the photon interaction.

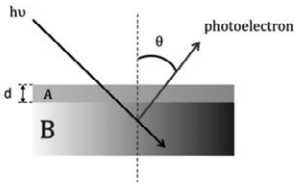

Fig. 7: Schematic representation of a uniform film deposit (A) on top of the substrate (B).

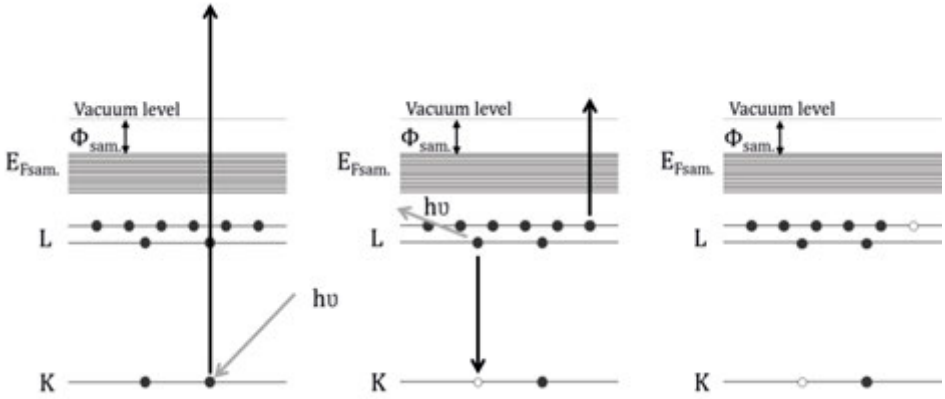

Fig. 8: Schematic representation of the Auger emission process. The photon excites a core electron of the K shell (left) the hole is filled by an electron of the L shell. The energy involved can be emitted as photon or can give up to the Auger electron (centre). The final state is a double ionised atom (right).

The vacancy created in the K shell can be filled by an electron of the L shell with the release of energy in a radiative way, i.e. emitting a photon, or by emitting a second electron: the Auger electron (fig. 8). The Auger transition is indicated with the historical X-ray notation; states with n=1,2,3,4... are labelled as K,L,M,N... respectively, while states with various combination of l=0,1,2,3,4...and j=$\frac{1}{2},\frac{3}{2},\frac{5}{2},\frac{7}{2}$, ... are given conventional suffixes 1,2,3,4... For example the $2p_{3/2}$ spectroscopic level is labelled in the historical X-ray notation as L_2 ($2p_{1/2} \rightarrow L_3$; $3d_{5/2} \rightarrow M_5$; $3d_{3/2} \rightarrow M_4$). This notation will be used in the XAS experiments reported in section 3. The $KL_1L_{2,3}$ Auger emission corresponds to the decay of an electron from the level *2s* (L_1) to the level *1s* (K) with

emission of an electron from the level $2p_{1/2,3/2}$ ($L_{2,3}$). The energy of the emitted Auger electrons is not correlated to the X-ray excitation energy and it depends only on the energy levels of the system. In some cases the emitted Auger electrons of an element present on the surface sample have the same energy of the XPS peak of another element. In such a situation a correct evaluation of the XPS signal is hamper, as in the case presented in sections 4 paragraphs 5 and 6.

4.2 Ultraviolet Photoemission Spectroscopy (UPS)

In the UPS technique the incident photons have energies $10 < h\nu < 50$ which are enough to remove the electrons from the valence band. The most common laboratory source for ultraviolet photoemission spectroscopy is the helium discharge lamp, which can provide photons with energy of 21.2 eV He(I) and 40.8 eV He(II). UPS, allowing the study of the valence band, provides useful information about the electronic structure of the surface and of molecular films. By comparison of the UPS spectrum with the calculated density of state (DOS) of the isolated molecule it is possible to evaluate the intactness of the molecules and their interaction with the substrate. An example of UPS spectrum acquired on the clean Au(111) surface is reported in fig. 9.

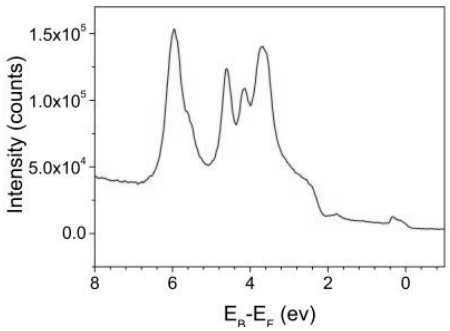

Fig. 9: UPS spectrum of the Au(111) valence band; the zero of the energy scale is set to the Fermi energy of the gold.

5 X-ray Absorption Spectroscopy (XAS)

The synchrotron based X-ray absorption spectroscopy is a fundamental tool for the magnetic and structural investigation of thin films (Wende 2004). In fact, the magnetic characterisation of monolayer and submonolayer molecular films cannot be carried out using the standard magnetometry techniques. These are not able to measure the signal of such small amounts of magnetic materials (Cornia et al. 2011).

The fundamental properties of XAS can be summarized as follow:

- *Element specificity.* The X-ray absorption involves the electronic level of the atoms, thus the energy of the transitions is a fingerprint of the specific element.
- *Sensitivity to electronic state (or valence).* The feature and the energy of the peaks are related to the oxidation states of the investigated atomic species.
- *Sensitivity to the spin.* By using circular polarised X-ray light and measuring the dichroism (X-ray Circular Magnetic Dichroism (XMCD)) it is possible to investigate the magnetism of the absorber.
- *Sensitivity to the anisotropy of the charge distribution around the absorbing atom.* By using linearly polarised light it is possible to measure the X-ray Natural Linear Dichroism (X-ray Natural Linear Dichroism (XNLD)) which is indicative of the orientation of the different molecular orbitals that can be related to a preferential orientation of the molecules.
- *Surface sensitivity.* Using the appropriate detection mode the technique is sensitive only to the top-most atomic/molecular layers of the surface.

X-ray absorption and the related dichroism can be measured only using X-ray synchrotron sources. In third generation synchrotron it is possible to produce polarised X-ray light tuneable in energy with a large flux of photons.

5.1 X-ray synchrotron radiation

The synchrotron radiation is generated by deviation of an accelerated electron beam by means of magnetic fields. This process gives rise to the emission of a wide and continuous electromagnetic spectrum. The electron beam is generated by thermionic emission process by means of an electron gun in UHV environment. The electrons are collimated and accelerated to hundreds MeV energy before being introduced in a booster ring where their energy is further increased to reach the final energy of few GeV. The electrons are then introduced in the storage ring, where theirs linear trajectory is deviated by means of magnetic fields (quadrupole units). In the linear sections of the storage ring additional devices are inserted "disturbing" the pathway of electrons, this process leads to the emission of electromagnetic radiation along the tangent to the electrons trajectory. The produced photons are collected and used for experiments in several beamlines built along the ring.

The main properties of the radiation of each beamline are due to the used system for the photon emission. In particular for the beamline working on XAS-derived techniques the so called “insertion device”, which is made by periodic arrays of magnets placed above and below the electron pathway (fig. 10), is employed. The in-

sertion devices are divided in two classes the *wigglers* and the *undulators*. The main differences are related to the range of photon energies emitted and the collimation of the light. The *wigglers* produce low collimated high energy photon (10-20 KeV) spread on a wide range of energies. The *undulators* generate high collimated energy photon with a narrow spectral emission range. The maximum of the spectral emission can be tuned by changing the distance of the two rows of magnets above and below the electrons path (fig. 10). In both *insertion devices* the emitted photons are linearly polarised. However, by using two or more set of *undulators* it is also possible to obtain the circularly polarised light needed for the XMCD measurements.

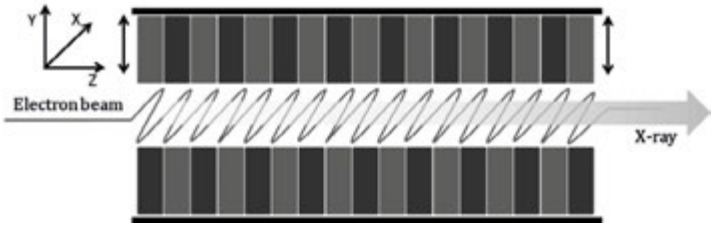

Fig. 10: Schematic representation of an insertion device. The grey and black elements are permanent magnets aligned in two rows, one above and one below the electron beam. In the *undulator* the gap distance between the two rows can be modified to tune the spectral emission.

5.2 X-ray absorption spectroscopy principles

The simplest way to describe X-ray absorption process is the so called one electron approximation (Stohr & Siegmann 2006). In this description the photon transfers its energy to a single core electron which is promoted from the core level to the valence band neglecting all the other electrons in the process. This view is clearly an oversimplification of the physics involved in the process and it does not allow a quantitative interpretation of the spectra. A more correct way to describe the phenomenon is the configuration picture. In this interpretation an atom is excited from its initial to the final excited configuration. Both configurations are described by theirs total angular momentum (J) which can be calculated with the (j-j) coupling scheme, as described in section 2 paragraph 4.1, or by the so called Russell-Saunders (RS) coupling:

$$L = \sum l_i \quad ; \quad S = \sum s_i \quad ; \quad J = L + S$$

where L and S are the total angular orbital momentum and the total spin angular momentum respectively, the l_i and s_i are the angular and spin momentum of the single electrons, respectively. This description allows to take in account the angular

momentum interaction between the excited electron and the other electrons belonging to the same atom.

The cross-section of the X-ray absorption process is calculated considering a time dependent perturbation to the electronic levels induced by the electromagnetic field. The transition probability from the initial state $|i\rangle$ to the final state $|f\rangle$ functions (both containing an electronic and a photon part) can thus be described following the formalism developed by Kramers (Kramers 1926) and by Dirac (Dirac 1929) as:

$$T_{if} = \frac{2\pi}{\hbar}\left|\langle f|H_{int}|i\rangle + \sum_n \frac{\langle f|H_{int}|n\rangle\langle n|H_{int}|i\rangle}{\varepsilon_i - \varepsilon_n}\right|^2 \rho(\varepsilon_f) d(\varepsilon_i - \varepsilon_f) \quad (19)$$

where ε_i, ε_f are the energy of the initial and the final state respectively, $\rho(\varepsilon_f)$ is the density of the final state per unit of energy and $H_{int} = (e/m_e)\,\vec{p}\cdot\vec{A}$ is the Hamiltonian describing the interaction with the electromagnetic field. Where e, m_e and $\vec{p}$ are the charge, the rest mass and the moment of the electron respectively and $\vec{A}$ is the potential vector. Just for clarity of the discussion we report that the electric field can be obtained as $\vec{E} = -\overrightarrow{\delta A}/\delta t$. The cross-section (σ) is thus obtained from the transition probability by normalizing for the total incident flux (ϕ_0):

$$\sigma = \frac{T_{if}}{\phi_0} \quad (20)$$

5.3 X-ray Magnetic Circular Dichroism (XMCD)

The X-ray Circular Dichroism (XMCD) technique allows the characterisation of the magnetic properties of the inspected material. In particular it provides information about the intensity and the direction of the magnetic moment of the probed element. It's important to recall the properties of the XAS experiment which allows element selectivity. The XMCD is thus able to measure magnetic moments of different elements present in the same sample.

In order to explain the basis of the XMCD experiment is convenient to refer to the $2p \rightarrow 3d$ transition of transition metals (fig. 11). In this case the small orbital moment of the d shell is quenched by the crystal field and the shell has only the spin moment. In order to be able to measure the difference in the spin state of the d shell we need a spin dependent XAS process. By using circular polarisation is possible to selectively excite the spin-up or spin-down photoelectron from the core shell. Since the XAS does not allow spin flip processes the photoelectron spin-up (spin-down) can be only excited in spin-up (spin-down) final states. The intensity of the transition thus reflects the density of the empty final states for the spin-up and spin-down respectively. In fact, if the electron is excited from a spin-orbit split level the photon

can transfer part of its angular momentum to the electron trough the spin-orbit coupling. The left circular polarised light transfers opposite angular momentum of the right one. In the transition $2p \rightarrow 3d$ the spin-orbit coupling split the $2p$ state in the $2p_{3/2}$ (L_3edge) and $2p_{1/2}$ (L_2 edge) states with opposite alignment of the two components. The spin polarisation of the photoelectron is the opposite in the two cases. The magnetic information is related to the spin-split valence band which acts as a detector for the photoelectrons and, as already mentioned, the intensity of the absorption is proportional to the density of the empty d final states. If the d valence band possesses an orbital momentum it can also act as orbital momentum detector allowing to separate the spin and orbital contribution to the magnetic moment.

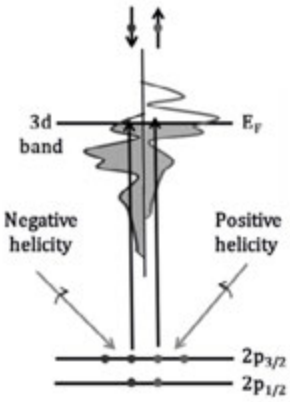

Fig. 11: Schematic representation of the circular polarised light absorption. The different probability of the two transitions gives rise to the XMCD signal at the L_3 edge.

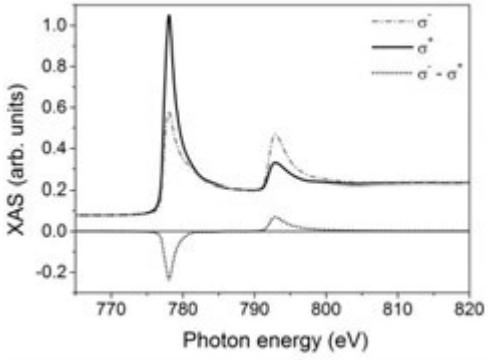

Fig. 12: XAS absorption spectra acquired with left ($\boldsymbol{\sigma^+}$) and right ($\boldsymbol{\sigma^-}$) circular polarisation of a thin film of cobalt evaporated on Cu(100) and the relative XMCD spectrum ($\boldsymbol{\sigma^- - \sigma^+}$).

The XAS spectra of a Co film acquired with the two circular polarisations and the resulting XMCD spectrum are reported in fig. 12. Considering the left circular

polarisation (σ^+ the relative cross-section) with the helicity pointing to the photon propagation direction and considering the reverse for the right polarisation (σ^- the relative cross-section) the XMCD spectrum is defined as:

$$XMCD = \sigma^- - \sigma^+ \quad (21)$$

The size of the dichroism effect scales like $cos\theta$, where θ is the angle between the photon spin and the magnetisation direction. Thus the maximum dichroism is revealed when the helicity of the photon lays in the same direction (parallel or antiparallel) of the quantization axis of the *d* shell, i.e. in the magnetisation direction.

In order to get information concerning the orbital and spin moments the sum rules, reported by Thole et al. (Thole et al. 1992) and Carra et al. (Carra & Altarelli 1993), can be employed. A complete discussion about the details of the calculation is beyond the aim of this work. Here only the general results which allow the calculation for the $2p \rightarrow 3d$ ($L_{2,3}$edges) are presented. For such transitions the angular momentum (m_{orb}) can be calculated as:

$$m_{orb} = -\frac{4\int_{L_2+L_3}(\sigma^- - \sigma^+)d\omega}{3\int_{L_2+L_3}(\sigma^+ + \sigma^-)d\omega} \cdot (n_{3d}) \quad (22)$$

where m_{orb} is in units of μ_B/atom, $(\sigma^- - \sigma^+)$ is the XMCD spectrum, and n_{3d} is the number of the *3d* holes of the specific transition metal atom. Similar formula allows the calculation of the spin momentum (m_{spin}):

$$m_{spin} = \frac{6\int_{L_3}(\sigma^- - \sigma^+)d\omega - 4\int_{L_2+L_3}(\sigma^- - \sigma^+)d\omega}{\int_{L_2+L_3}(\sigma^+ + \sigma^-)d\omega} \cdot (n_{3d}) \cdot \left(1 + \frac{7\langle T_z\rangle}{2\langle S_z\rangle}\right)^{-1} \quad (23)$$

where the $\langle T_z\rangle$ is the expectation value of the magnetic dipole operator and $\langle S_z\rangle$ is equal to half of the m_{spin} in Hartree atomic units. By neglecting the $\langle T_z\rangle/\langle S_z\rangle$ ratio contribution (Chen et al. 1995; Wu & Freeman 1994) it is possible to calculate the two contributions from the direct integration of the XAS and XMCD spectra. The integral $(\sigma^- + \sigma^+)$ can be evaluated after the subtraction of a two step background function (L_3:L_2 ratio 2:1 in agreement with their 2j+1 degeneracy). Referring to fig. 13 the orbital and spin momenta can be thus calculated as (Chen et al. 1995):

$$m_{orb} = \frac{-4q \cdot n_{3d}}{2r} \quad (24)$$

$$m_{spin} = \frac{-(6p-4q) \cdot n_{3d}}{6r} \quad (25)$$

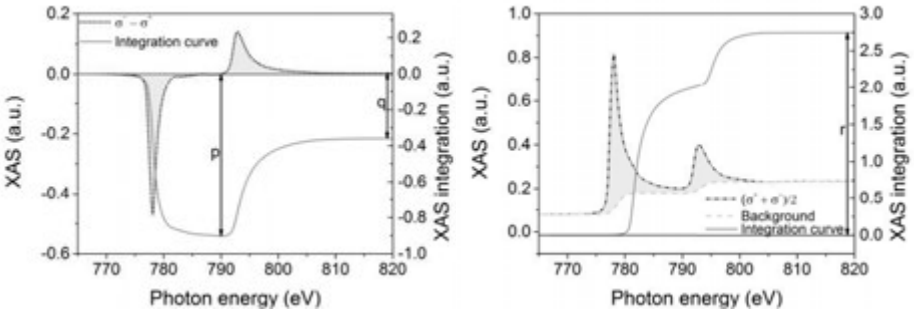

Fig. 13: Integration of the cobalt XMCD spectrum (left) and the integration of the XAS spectrum calculated as $(\sigma^- + \sigma^+)/2$ after the subtraction of the two steps background.

5.4 X-ray Natural Linear Dichroism (XNLD)

The XNLD experiment is defined as the difference between the XAS spectra acquired with vertical and horizontal polarised light. The XNLD technique provides information about the anisotropy of the charge distribution around the absorbing atom. This information can be useful for individuating preferential orientation in SMM hybrid surfaces (Cornia et al. 2011). A simple way to visualize the phenomenon originating the linear dichroism is to invoke the so called "search light effect" introduced by Stöhr *"X-ray absorption is governed by electric dipole transition and the photoelectrons are preferentially excited into the direction of the electric field"* (Stöhr 1995). The dichroism derives from the anisotropy in the valence level of the investigated atom. Considering a transition $2p \rightarrow 3d$ its intensity is related to the sum over all the degenerate *2p* states and all the *3d* states. The core levels leads to a spherical symmetry contribution. The *3d* orbital contribution is strictly related, in mononuclear molecular complexes, to the symmetry of the complex. In cubic symmetry the *3d* degeneracy is broken by the ligand field obtaining the t_{2g} and e_g irreducible representations. The sum of each representation gives rise to a spherical contribution. In this situation no dependence on the photon electrical field orientation has to be expected. However lowering the symmetry of the complex the contribution is no more spherically symmetric and a dependence on the electrical field orientation is found. The intensity of the transition is then at its maximum when the electric field points to the empty states and it will be zero on nodal plane. This allows to extract information about the local symmetry of the absorber.

5.5 X-ray absorption detection

As reported in the previous sections the XAS absorption leads to a core hole final state. This state is not stable and it evolves relaxing in two principal ways: by the

emission of Auger electrons or by emission of fluorescence photons. Both emissions are related to the probability of the XAS absorption and thus they can be measured in function of the photon energy to provide the XAS spectrum. Different detection methods can be employed for the two emissions. In this work the Total Electron Yield (TEY) mode was used.

The Auger emission leads to ionised atoms. If the sample is grounded an electron current flows to the sample to restore the neutrality. This current can be read by means of a picoammeter (fig. 14). Since the process is related to the emission of the Auger electron the TEY mode is surface sensitive. In fact the escape length of the Auger electrons is ~2 nm and no information on processes occurring deeper in the sample are accessible. This detection method allows the study of the superficial properties of the samples.

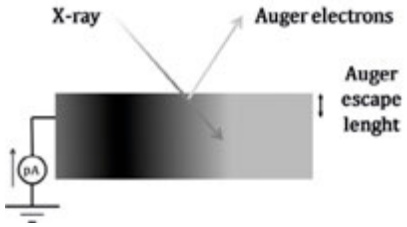

Fig. 14: Schematic representation of the Total Electron Yield (TEY) detection system.

6 DEIMOS beamline

Most of the XAS experiments carried out during this thesis work have been performed on the DEIMOS beamline, which will be shortly described here. DEIMOS beamline experimental setup was designed to perform XAS and its derivate techniques. The beamline's photon energy range is 250-2500 eV. The *insertion device* allows the study with linearly and circular polarised light. A cryo-magnet allows measuring the XAS at temperature as low as 1.5 K with tuneable magnetic field along the photon direction up to 70 kOe.

Two preparation chambers connected to the beamline allows the *in situ* preparation of the sample (fig. 15). In particular the MBE chamber was dedicated to the surface preparation and provides sputtering/annealing and metal evaporation facilities. The other (RAOUL) was employed for the molecular sublimation. The UHV system offers also the possibility to characterise the investigated surfaces by STM, Low Electron Energy Diffraction (LEED), and Auger Electron Spectroscopy (AES).

In Our experiments (see section 3 paragraph 4) a EFM3 Omicron evaporator was assembled in the MBE chamber for the evaporation of the cobalt while our home-made molecules sublimation system was installed in the RAOUL chamber.

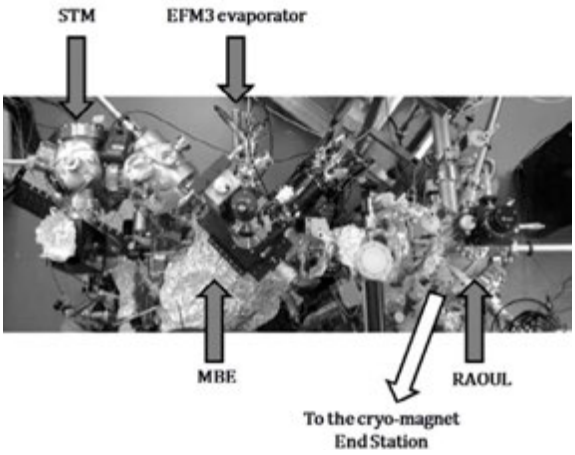

Fig. 15: Top view of the DEIMOS UHV system which allows the *in situ* preparation of the samples.

7 Low Energy Ion Scattering (LEIS)

The Low Energy Ion Scattering (LEIS), also called Ion Scattering Spectroscopy (ISS) is one of the most powerful techniques in the study of the chemical composition of the most superficial layer of surfaces (Brongersma et al. 2007). Due to its ultimate surface sensitivity, it requires UHV condition. In the LEIS experiment the sample surface is bombarded with noble gas ions which are accelerated to energy of 500-10000 eV. The ions collide against the atoms forming the outer layer of the surface. The collision can be describe, in first approximation, as an elastic binary collision of a projectile of mass M_i with energy E_0 with a target of mass M_t at rest; as schematized in fig. 16.

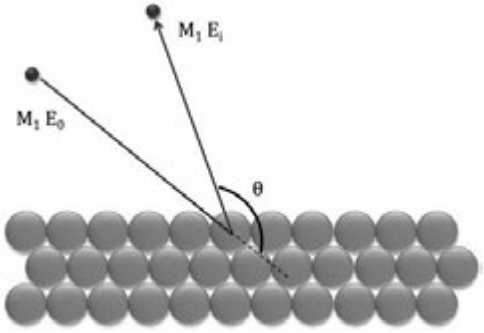

Fig. 16: Schematic representation of the elastic binary collision. The projectile collides against the target and it is back scattered.

In the collision part of the E_0 energy of the projectile is transferred to the target atom. The energy transferred to the target depends on the θ angle and on the mass of the two atoms i.e. M_i and M_t. The projectile is then back scattered with energy E_i and it can be collect by an analyser. An energy scan of the projectiles coming from the target allows to get information on the chemical composition of the outer layer. By knowing the scattering angle (see fig. 16) and the mass of the projectile the following equation can be used to calculate the mass of the target atom (Niehus & Spitzl 1991):

$$E_i/E_0 = \{\pm[(M_t^2 - M_1^2 sin^2\theta)^{1/2} + M_i cos\theta]/(M_1 + M_t)\}^2 \qquad (26)$$

However, if the target possesses a low atomic weight the interaction of the projectiles with the surface can modify the structure of the surface (Brongersma et al. 1998). In order to avoid such phenomenon, low energy of the projectile is commonly used ($E_0 < 1000$ eV).

We have used this technique for the study of the cobalt growth on a Cu(100) single crystal. The two elements have high atomic weights and hence small penetration depth of the He^+ ion is expected.

8 Scanning Probe Microscopies (SPM)

Scanning Probe Microscopies (SPM) are one of the most powerful techniques for studying the surfaces. In fact, by using a tip as local probe, they allow to achieve local surface information with high spatial resolution down to the atomic scale. Scanning Tunnelling Microscopy (STM) and Atomic Force Microscopy (AFM) are two SPM that are based on quantum mechanical tunnelling effect and tip-surface interaction forces, respectively. That made them useful tools for different surface analysis requirement.

8.1 Scanning Tunnelling Microscopy (STM)

A schematic view of a STM is reported in fig. 17 showing the metallic tip, acting as local probe, the conductive sample, the piezo motor system and the feedback circuit. A bias is applied between the tip and the sample surface, the tip is then brought close to the surface until a quantum mechanical tunnelling current (I) flows through a vacuum gap 5-15 Å wide.

In order to record the image the tip is moved across the surface by means of a piezo motor system which allows a fine control of the position (X, Y and Z) respect to the sample surface. The use of a feedback loop circuit on the piezo makes possible

to scan the surface with a constant tunnelling current (constant current mode). The feedback circuit receives the tunnelling current variation from the preamplifier and acts on the Z piezo in order to keep the current constant. The STM image information is related to the ΔZ movements of the tip. In contrast, in height constant mode the feedback circuit is set off during the scan and the image information is the tunnelling current variation. Working in constant current, i.e. with the feedback loop on, allows the imaging of rough surfaces reducing the probability of tip crashing; however the feedback circuitry time delay imposes a low scanning speed. This limitation can be overcome employing the Z constant mode but the presence of the feedback off imposes strictly requirements for atomically flat surface in order to prevent tip crashing. All of the images presented in this work were acquired in constant current mode.

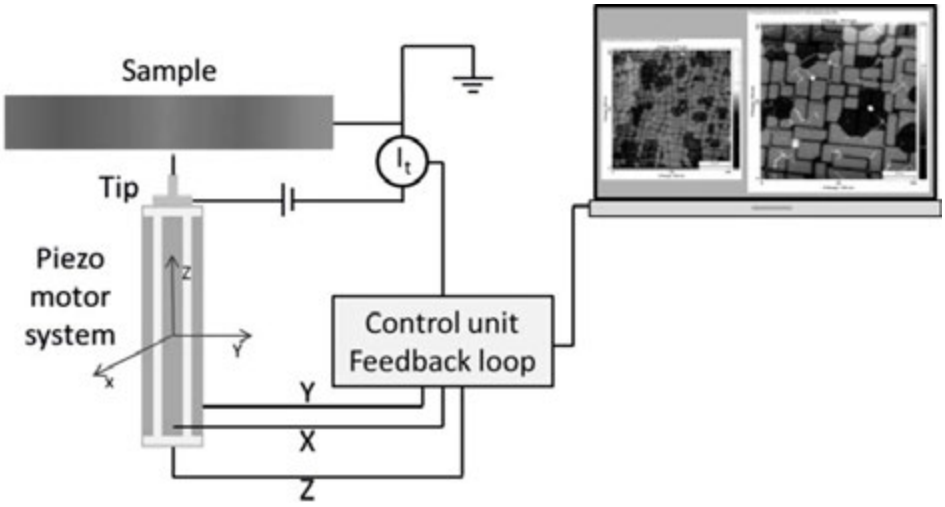

Fig. 17: STM scheme. The sample is grounded and the potential is applied to the tip as it is in the Omicron STM (see section 2 paragraph 9.3). The feedback loop receives the current from the preamplifier and acts on the piezo motor (in constant current mode). The data are recorded by a computer.

8.2 Tunnelling effect

In order to better understand the physics that describes the tunnelling current involved in the STM experiment a brief description of the quantum mechanical tunnelling process is needed. In fig. 18 is reported a scheme of a quantum mechanical particle that goes through a finite potential barrier, with V_0 height and d thickness.

In the classical view one particle with energy $E < V_0$ cannot overcome the barrier. Using the quantum mechanical approach the electron can be described by a wave function $\psi(z)$ and the probability to overcome the barrier is non-zero.

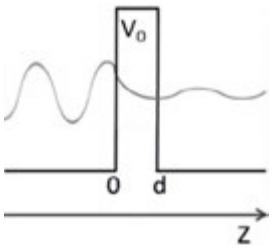

Fig. 18: Scheme of a tunnelling barrier. The electron comes from the left part of the barrier.

It can be calculated resolving the time independent Schrödinger equation below:

$$\left[-\frac{\hbar^2}{2m}\frac{d^2}{dz^2}+V(z)\right]\psi(z)=E\psi(z) \qquad (2.27)$$

where:

$V(z)=0$; outside the barrier
$V(z)=V_0$; inside the barrier

The solutions of the equation are in form of planning waves:

$$\psi(z)=\psi(0)e^{\pm kz} \qquad (28)$$; outside the barrier

Where the vector wave k is:

$$k=\sqrt[2]{\frac{2mE}{\hbar^2}} \qquad (29)$$

and an exponential decay function inside the barrier for an electron going to the positive Z direction:

$$\psi(z)=\psi(0)e^{-kz} \qquad (30)$$

Where the k exponential decay factor is:

$$k=\sqrt[2]{\frac{2m(V_0-E)}{\hbar^2}} \qquad E<V_0 \qquad (31)$$

The probability to find the electron inside the barrier is equal to: $|\psi^2(0)|e^{-2kz}$ and since the thickness d of the barrier is not infinite there is a non-zero probability for the electron to overcome the barrier. Just considering this simplified tunnelling

model is possible to highlight the exponential dependence of the tunnelling probability to the gap distance d as it occurs for the tunnelling current in the STM tip-sample gap.

A more accurate description of the phenomenon was developed starting from the Bardeen formalism (Bardeen 1961), which considers the tunnelling process related to many independent scattering events that lead the electrons to overcome the tip-sample gap. In this view the electrons tunnel from the states of the tip to ones of the sample or *vice versa*. The problem can be described by the time-dependent Schrödinger equation using time-dependent perturbation theory and assuming that the two systems (tip and sample) are weakly interacting. Hence, considering low bias and applying the Fermi's golden rule for the transition probability, the current can be writes as:

$$I = \frac{2\pi e}{\hbar}\sum_{\mu,\nu}\{f(E_{\mathrm{T},\mu})[1 - f(E_{\mathrm{S},\nu}+\mathrm{eV})] - f(E_{\mathrm{S},\nu}+\mathrm{eV})[1 - f(E_{\mathrm{T},\mu})]\} \cdot |M_{\mu,\nu}| \cdot {}^2\delta(E_{\mathrm{T},\mu} - E_{\mathrm{S},\nu}) \qquad (32)$$

Where $f(E)$ is the Fermi-Dirac distribution function and $E_{\mathrm{T},\mu}$ and $E_{\mathrm{S},\nu}$ are the energy eigenvalue of the state ψ_μ of the tip and ψ_ν of the sample respectively. The $\delta(E_{\mathrm{T},\mu} - E_{\mathrm{S},\nu})$ term accounts for the energy conservation of the electron as expected for the elastic tunnelling. The $M_{\mu,\nu}$ is the tunnelling matrix defined as:

$$M_{\mu,\nu} = -\frac{\hbar^2}{2m_e}\int\left[(\psi_\mu)^*\vec{\nabla}\psi_\nu - \psi_\nu\vec{\nabla}(\psi_\mu)^*\right] d\vec{s} \qquad (2.33)$$

In order to calculate the tunnelling matrix the knowledge of the explicit form of the state function of the tip and the sample is needed. However, the description of the atomic structure of the two electrodes is not trivial. In detail, the atomic structure of the tip is unpredictable because there is no reproducible preparation at atomic level for it; moreover the tip structure can undergo changes during the STM experiment.

To overcome these issues Tersoff and Hamann (Tersoff & Hamann 1983; Tersoff & Hamann 1985) assumed a simplified view of the tip schematizing its apex as reported in fig. 19. The exponential decay of the tunnelling current, in respect to the distance, leads to consider that the electron tunnelling process involves mainly the last atom of the tip. Therefore it is possible to assume that the tip apex is spherical. By considering also only the *s*-waves involved in the process and room temperature or below it gives:

$$I \propto V \cdot \rho_{\mathrm{T}}(E_{\mathrm{F}}) \cdot \rho_{\mathrm{S}}(E_{\mathrm{F}}, \vec{r}_0) \cdot e^{2kR} \qquad (34)$$

Where V is the bias, $\rho_T(E_F)$ is the density states of the tip, $\rho_S(E_F, \vec{r}_0)$ is the local density of the state (LDOS) of the sample surface evaluated at the Fermi energy and k is defined as: $k = \sqrt[2]{(2m_e\phi)}/\hbar$; ϕ is the effective barrier height. Under the Tersoff and Hamann assumptions the tip results simply as local probe and the sample contribution to the current is related to its LDOS given by:

$$\rho_S(E_F, \vec{r}_0) = \sum_v |\psi_v(\vec{r_0})|^2 \, \delta(E_v - E_F) \qquad (35)$$

Where the exponentially decay of the wave functions $|\psi_v(\vec{r_0})|^2$ on increasing $|\vec{r_0}|$ explains the current dependence to the tip-sample distance.

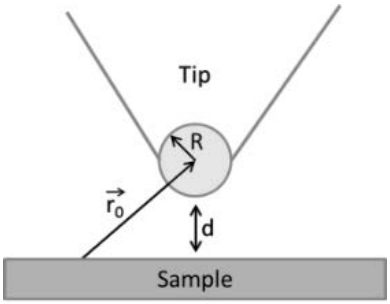

Fig. 19: Tersoff and Hamann simplify tip scheme.

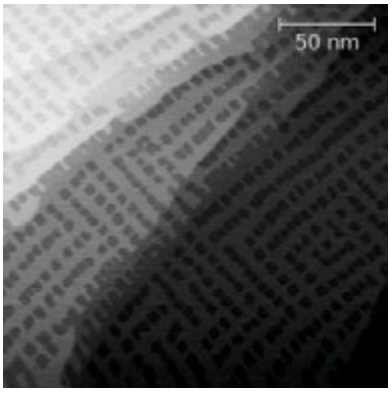

Fig. 20: STM image of small islands of Cu_2N grown on Cu(100) surface (200 pA; 2 V; 200x200 nm^2).

From the last two equations 34 and 35 it results also that working in current constant mode the final image is the constant LDOS surface of the sample. In fact STM experiments access directly the LDOS of the sample and not its morphology. Obviously the LDOS is related to the morphology but in some cases the STM image is not corresponding to it. For example imaging Cu_2N islands on Cu surface, by us-

ing constant current mode and small bias, the islands are showed as depression (fig. 20). A full monolayer of Cu_2N grown on Cu(100) will be used as substrate for the deposition of the Fe_4Ph molecule in section 4 .

8.3 Scanning Tunnelling Spectroscopy (STS)

It has been demonstrated that the STM technique is sensitive to the local density of states. This allows to get information on the LDOS at atomic scale. In order to achieve information on the energy dependence of the LDOS the scanning tunnelling spectroscopy can be employed. In this measure the tip is positioned on top the interesting point and the feedback loop is turned off. A ramp of potential is applied on the tunnelling junction while measuring the tunnelling current. In this way a single point scanning tunnelling spectroscopy is recorded. The data obtained will be the convolution of the LDOS of the tip and the sample. Assuming a flat LDOS for the tip the current is described as:

$$I \propto LDOS_{sample} V \quad (36)$$

Thus the d(I)/d(V) curves provide direct information of the LDOS of the sample. In order to be able to measure the d(I)/d(V) a lock-in detection of an alternate bias is commonly employed. The alternate bias is superimposed to the potential ramp and the lock-in allows to discard the capacitive current signal. In this way it is possible to record the d(I)/d(V) spectra directly. In order to take in account the variation of the transmission coefficient respect to the applied bias a further normalization of the data is generally employed (Selloni et al. 1985). This dependence can be eliminated by using the (d(I)/d(V))/(I/V) as proposed by Stroscio and Feenstra (Stroscio et al. 1986; Feenstra & Mårtensson 1988).

It's important to note that the STS experiment allows a direct measure of the conductance of the investigated point. This is crucial point for the study of inelastic tunnelling process (see section 4 paragraph 7).

9 Multiplatform Ultra-High Vacuum system

In this work mostly of the surface characterisations were carried out exploiting a multiplatform UHV system at the Center for Scanning Probe Characterisation Techniques (CeTeCS) of the Dept. of Chemistry at Florence University (fig. 21). The system offers the possibility to prepare the samples and their investigation *in situ* employing XPS, UPS, LEIS and STM techniques.

9.1 Sublimation chamber

The sublimation chamber was equipped with the system for the molecular sublimation described in section 2 paragraph 2 and with a Sycom quartz crystal microbalance. The base pressure of the chamber is 10^{-10} mbar.

9.2 XPS, UPS and LEIS chamber

The chamber was equipped with a SPECS Microfocus 600 monochromatic source (Al K_α radiation), coupled with a helium discharge lamp and with a hemispherical electron/ion energy analyser (VSW mounting a 16-channel detector). The sample was mounted on a manipulator which permitted the variation of the angle θ between the normal to the sample and the analyser while maintaining the angle between the analyser axis and the x-ray and ultraviolet sources fixed at 54.5°. The XPS source was operated at a power of 100 W (10 kV and 10 mA). To record LEIS spectra we used a focused (approximately 1-2 mm^2) beam of ions generated by a Omicron ISE 100 Gun with an energy range 600 eV to 1500 eV impinging on the surface at an angle of 45° using He^+ as primary ion sources. The scattering angle was 135°, and the kinetic energy of the scattered ions was measured by using the same hemispherical analyser employed for XPS.

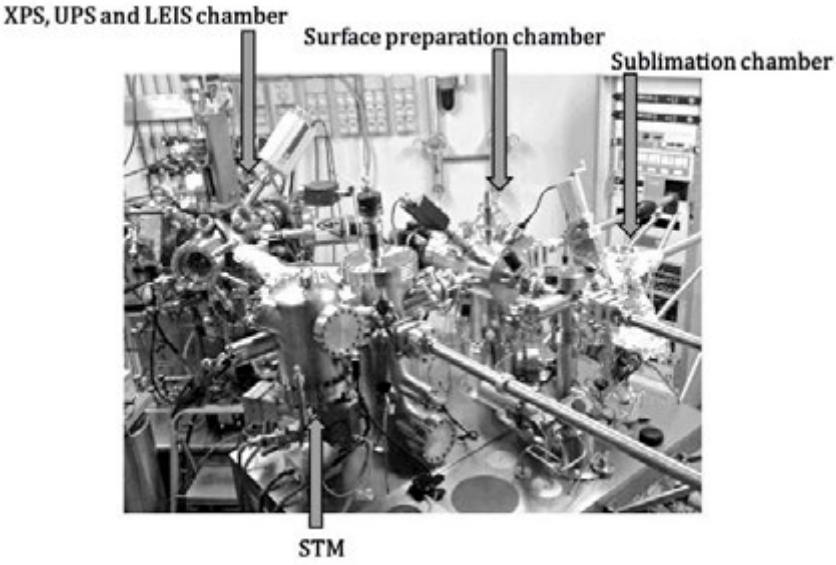

Fig. 21: Picture of the multiplatform UHV system which offers the possibility prepare the sample and investigate it by means of XPS, UPS, LEIS and STM techniques.

9.3 STM Omicron system

In the STM chamber is housed an Omicron Variable temperature STM which can operate in 25-1500 K range. We exploited the low temperature range for the hybrid surface investigation using electrochemically etched tungsten tip. The potential was applied to the tip while the sample is grounded. The base pressure of this chamber is $5 \cdot 10^{-11}$mbar.

Section 3
The terbium bis(phthalocyaninato) complex

1 Introduction

Terbium bis(phthalocyaninato) complex ($TbPc_2$) is one of the most investigated SMM (Ishikawa et al. 2003). Due to its magnetic properties the $TbPc_2$ molecule, and its derivatives, is a promising candidates for spintronic purposes (Bogani & Wernsdorfer 2008; Urdampilleta et al. 2011; Katoh, Isshiki, et al. 2012). The $TbPc_2$ molecule belongs to the metal double decker class in which a Tb^{3+} ion is bound in the centre of two phthalocyanine molecules staggered 45° by each other, as show in fig. 22.

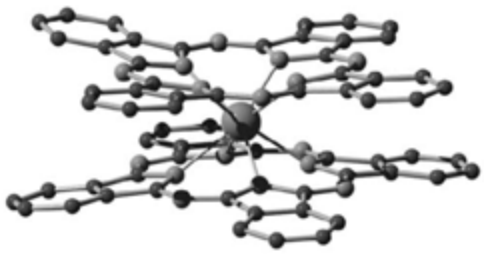

Fig. 22: Terbium bis(phtahalocyaninato) complex ($TbPc_2$) structure.

$TbPc_2$ can be easily synthesised as neutral $[TbPc_2]^0$ and cationic $[TbPc_2]^{-1}$ powder, as described in the next paragraph (Katoh et al. 2009; De Cian et al. 1985). By chemical oxidation of $[TbPc_2]^0$ (Takamatsu et al. 2007) or by electrochemical synthesis (Gonidec et al. 2010; Zhu et al. 2004) is also possible to achieve the $[TbPc_2]^{+1}$ compound which is not stable, behaving as strong oxidative molecule. It is important to note that the oxidation number of the metal ion does not change from the oxidised $[TbPc_2]^{+1}$ to the reduced $[TbPc_2]^{-1}$ molecule because the oxidation/reduction process involves only the electronic structure of the ligands (Zhu et al. 2004).

Luigi Malavolti, *Single molecule magnets sublimated on conducting and magnetic substrates*,
ISBN 978-88-6655-969-6 (print) ISBN 978-88-6655-970-2 (online)

The magnetism of the $TbPc_2$ molecules derives from the large magnetic moment and the huge magnetic anisotropy of the lanthanide ion. The molecule is characterised by strong uniaxial anisotropy with the easy axis of magnetisation along the idealised C_4 rotation axis. The ground state manifold for the $4f^8$ electronic configuration is characterised by J = L+S = 6, which is split by the crystal field at the single Tb^{3+} ion. This results in a separation between the ground doublet, well described by Jz = $\pm$6, and the first excited state on the order of a few hundred Kelvin (Ishikawa et al. 2003; Takamatsu et al. 2007). In the $[TbPc_2]^0$ a second spin system is defined by the presence of an unpaired electron delocalized on the π system of the phthalocyanine ligands (Ishikawa et al. 2004; De Cian et al. 1985). Some differences in the magnetic behaviour of the three oxidation forms of the $TbPc_2$ are reported in literature. In particular the oxidation process leads to an increase of the barrier opposing the reversal of the magnetisation (Takamatsu et al. 2007). By Density Functional Theory (DFT) calculations Ishikawa and Takamatsu (Takamatsu & Ishikawa 2007) have showed that the oxidation process leads to a shrink of the interplanar distance between the two phthalocyanine ligands, suggesting an increase of the crystal field applied to the Tb^{3+}. The hysteresis loops of the $[TbPc_2]^{-1}$ and $[TbPc_2]^{+1}$, investigated by Magnetic Circular Dichroism (MCD) of frozen solutions, show the presence of the so called butterfly hysteresis shape (Gonidec et al. 2010), which is characterised by the presence of moderate tunnelling in zero field. Similar behaviour is detected also in $[TbPc_2]^0$ as reported in paragraph 2.

The high chemical stability of the MPc_2 molecules allows the $[TbPc_2]^0$ to be thermal sublimated in Ultra-high Vacuum (UHV) as well as in High Vacuum (HV) conditions (Zhang et al. 2009; De Cian et al. 1985; Margheriti et al. 2010; Stepanow et al. 2010). This property boosted the studies of the $[TbPc_2]^0$ allowing the preparation of many different hybrid surface made by molecules deposited on solid substrates. Due to the flat shape of the molecules, that facilitates the imaging, detailed STM investigations have been carried out. In thin film of MPc_2 sublimated on different metal surfaces (Zhang et al. 2009; Stepanow et al. 2010; Toader et al. 2011; Fu et al. 2012; Schwöbel et al. 2012) the molecules lay flat with one of the two phthalocyanine ligands facing the surface. In the case of $TbPc_2$ the easy axis is pointing out of the surface plane. By STM imaging the single $TbPc_2$ molecule looks as four-lobed structure when imaged in low bias or in low resolution images whereas in high resolution images eight-lobed structure is commonly observed (Fu et al. 2012).

In Scanning Tunnelling Spectroscopy (STS) experiments the orbital energies can be detected (Katoh et al. 2009; Toader et al. 2011; Fu et al. 2012) while in zero bias region a Kondo peak, due to the presence of the unpaired electron on the ligands, is revealed in $TbPc_2$ molecule sublimated on Au(111) (Katoh et al. 2009; Komeda et al. 2011). However, the presence of the unpaired electron may be altered on absorption

on surface so that in $TbPc_2$ molecules sublimated on Co grown on Ir(111) it is quenched (Schwöbel et al. 2012).

In parallel the magnetic characterisation of such hybrid surfaces has been carried out. For this purpose one of the mostly employed techniques is the X-ray Circular Dichroism (XMCD), thanks to the element selectivity and the high sensitivity, which allows the characterisation of sub-monolayer films (Funk et al. 2005; Cornia et al. 2011). On metal surfaces the XMCD derived hysteresis loops acquired in sub-monolayer/monolayer samples show no opening (Stepanow et al. 2010; Margheriti et al. 2010; Lodi Rizzini et al. 2011; Lodi Rizzini et al. 2012), while on thicker film the hysteresis opening is recovered (Margheriti et al. 2010). This anomalous behaviour has been investigated but, by thus far, no clear explanation is reported. In order to rationalize it a key role of molecule-surface and molecule-molecule interactions has been proposed. The presence of molecule-surface interactions has been recently reported to play a key role in the prominent antiferromagnetic (AF) coupling observed in sub-monolayer film of $TbPc_2$ sublimated on nickel (Lodi Rizzini et al. 2011), and in the observation of an exchange bias on thin film sublimated on manganese (Lodi Rizzini et al. 2012). Moreover, the molecule-molecule interactions are responsible of the different magnetic behaviour of the isostructural paramagnetic YPc_2 molecule in solvated and non-solvated crystallographic phase (Paillaud et al. 1991).

The preferential orientation of the $TbPc_2$ molecules in thin and thick films has been investigated by X-ray Linear Natural Dichroism (XNLD). In thin films the molecules are lying flat, in agreement with the STM characterization, on the contrary in thick films a preferential orientation in "standing-up" geometry has been revealed (Margheriti et al. 2010). This is not surprising; it is well known that for simple phthalocyanine during the films grown a molecular reorientation process occurs (Biswas et al. 2009). In fact synchrotron based investigations using near-edge X-ray absorption fine structure spectroscopy and surface sensitive X-ray Photoemission Spectroscopy (XPS) experiments revealed that copper phthalocyanine (CoPc) molecules start to lose their lying orientation on Au(111) substrates after 3ML and a standing orientation is fully retrieved after ca. 10 ML (Biswas et al. 2007). This structural change obviously alters the molecule-molecule interactions and a non-negligible effect on the behaviour of the $TbPc_2$ can be anticipated.

In order to shed some light on this phenomenon we have studied the magnetic properties of the $TbPc_2$ molecule starting from the characterisation of the pristine microcrystalline powder, throughout the sublimation process to the final film samples. We have also investigated the magnetic behaviour of thin films sublimated on two of the most employed magnetic substrate in spintronic devices. This characterisation was performed in order to prepare the ground for the employment of the $TbPc_2$ as organic layer in spin valve device (see paragraph 4).

2 Erratic magnetic hysteresis

2.1 $TbPc_2$ synthesis

The neutral $MPc_2 \cdot CH_2Cl_2$(M = Tb^{3+} and Y^{3+}) compounds were synthesised according to the procedure reported in literature (Katoh et al. 2009; De Cian et al. 1985). The template reaction was carried out by mixing 1,2-dicyanobenzene and $M(OAc)_3 \cdot 4H_2O$ in 1-hexanol in presence of catalytic amount of 1,8-diazabicyclo[5,4,0]undec-7-ene (DBU) as represented in fig. 23.

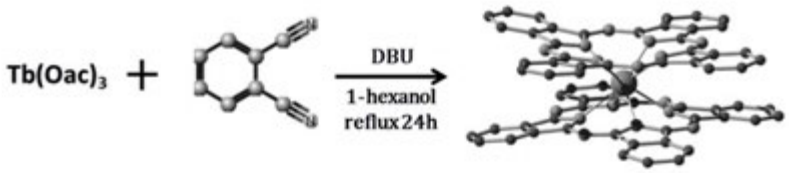

Fig. 23: Terbium bis(phtahalocyaninato) complex ($TbPc_2$) synthesis reaction scheme.

It was used 8:1 molar ratio of 1,2-dicyanobenzene : $M(OAc)_3 \cdot 4H_2O$ in order to prevent the formation of M_2Pc_3 molecules. The mixture was refluxed for at least 1 day. Once at room temperature it was filtered and the precipitate was washed with acetic anhydride, cold acetone, and n-pentane in sequence. The precipitate was extracted with several portion of $CHCl_3$. The neutral $[TbPc_2]^0$ and the anionic one $[TbPc_2]^{-1}$ reside in the solution while most of the free phthalocyanines reside in the solid phase. The solution was then concentrated and purified by chromatography. The column was prepared using silica as stationary phase and 98:2 CH_2Cl_2/MeOH solution was employed as eluent. The first green fraction collected contains the $[TbPc_2]^0$ whereas the second blue fraction is the $[TbPc_2]^{-1}$. The green solution was then concentrated. By addition of n-Hexane a dark microcrystalline powder of $[TbPc_2]^0 \cdot CH_2Cl_2$ was precipitated. After filtration the powder was left to dry in air before being used.

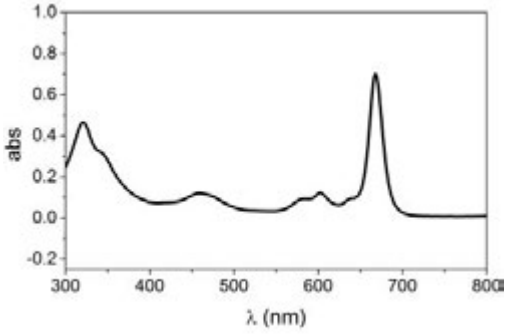

Fig 24: UV/vis spectrum of a solution of $[TbPc_2]^0$ in $CHCl_3$.

The powder of the neutral complex was solubilized in $CHCl_3$ in order to recorder the UV/visible absorption spectrum (fig. 24) to confirm the quality of the neutral compound (Gonidec et al. 2010). To have more insight on the UV/vis spectrum peaks attribution see paragraph 2.6.

2.2 Microcrystalline $[TbPc_2]^0 \cdot CH_2Cl_2$ hysteresis

The magnetic properties of a microcrystalline powder sample of $[TbPc_2]^0 \cdot CH_2Cl_2$, hereafter simply $TbPc_2 \cdot CH_2Cl_2$, were investigating by using a Vibrating Sample Magnetometer (VSM) (see section 2 paragraphs 1.1 and 1.2).

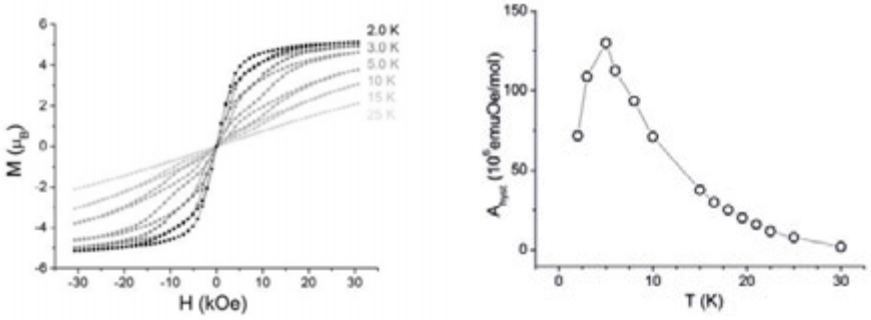

Fig 25: Temperature dependence of the hysteresis loops recorded on $[TbPc_2]^0 \cdot CH_2Cl_2$ a pure microcrystalline powder sample (left) the data are reported per mole of $TbPc_2$ and the field sweeping rate is 50 Oe s^{-1}; Temperature dependence of the area inside the hysteresis loops (right). The line is only a guide to the eye. Reproduced from Ref. (Malavolti et al. 2013) with the permission from The Royal Society of Chemistry.

On the left of fig. 25 left it is reported the temperature dependence of the hysteretic loops recorded using a field-sweeping rate of 50 Oe s^{-1}. At 25 K the curve shows a paramagnetic behaviour with linear field dependence of the magnetisation. Just decreasing the temperature to 15 K a small hysteretic behaviour is detected and between 10 K and 2 K the so called butterfly shape hysteresis is well visible.

It is interesting to note that the temperature dependence of the area inside the hysteretic loops is not monotone (fig. 25 right). Starting from 2 K the area increases until reaching the maximum value at 5 K and then it shrinks asymptotically increasing the temperature. The hysteresis loops presented in fig. 25 left are taken as reference for further comparison.

2.3 Sublimation process: $TbPc_2$ hysteresis transformation

As stated in paragraph 1 $TbPc_2$ SMM has attracted a growing interest due to its thermal stability that allows the sublimation of intact molecules in HV condition

(Zhang et al. 2009; De Cian et al. 1985; Margheriti et al. 2010; Stepanow et al. 2010). We studied how the thermal treatment affects the hysteresis behaviour of this SMM. Using the sublimation system reported in section 2 paragraph 2 the pristine powder of $TbPc_2 \cdot CH_2Cl_2$ was degased at 580K for several hours in HV condition (pressure < $5x10^{-7}$mbar). It was then warmed up to the sublimation temperature of about 670 K for few minutes and finally allowed to cool to room temperature. The X-ray Diffraction (XRD) analysis of the heated powder is reported in fig. 26 together with the spectrum of the pristine powder. As expected the pristine powder spectrum matches the simulated one for a crystalline powder, while, on the other hand, the heated sample looks like an amorphous phase. The lack of crystalline structure could be related to the loss of the crystallization solvent (CH_2Cl_2) during the heating procedure.

The heated powder was characterised by VSM technique (fig. 27 left) repeating the measurements carried out on the pristine sample. Unexpectedly the temperature dependent hysteresis loops show no hysteresis opening throughout the whole temperature range.

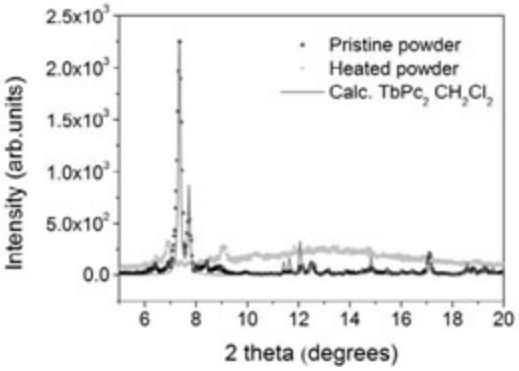

Fig 26: XRD spectra of pristine (black circles), $TbPc_2 \cdot CH_2Cl_2$ calculated (solid grey line), and heated sample (grey circles). The pristine powder spectrum matches the calculated one while the heated powder spectrum is amorphous like.

In order to check the intactness of the molecules in the sample a thick film of $TbPc_2$ was sublimated on Kapton using the heated powder. The temperature dependence of the hysteretic loops is reported in fig. 27 right. The curves show the recovery of the hysteretic behaviour. The opening is detected at temperatures as high as 10 K, slightly lower than in the pristine microcrystalline powder, and a monotone dependence of the insight area on temperature throughout the investigated range is observed. Despite these differences the presence of the hysteresis opening suggests that the heated powder comprises intact molecules.

The different behaviours shown by the three samples of $TbPc_2$ must be related to different dynamic relaxation processes operating in the three different phases. In or-

der to explain these anomalies and further confirm the presence of intact molecules in the heated powder the ac susceptibility was investigated. The measurements were carried out from 0.5 Hz up to 10 kHz in 5-100 K temperature range on both powder samples, pristine and heated, respectively. No further measurements were carried out on the $TbPc_2$ film because it showed too small magnetic signal for a complete *ac* susceptibility investigation. Both powders show an out of phase component of the susceptibility in zero field which is the fingerprint of the SMM behaviour (fig. 28).

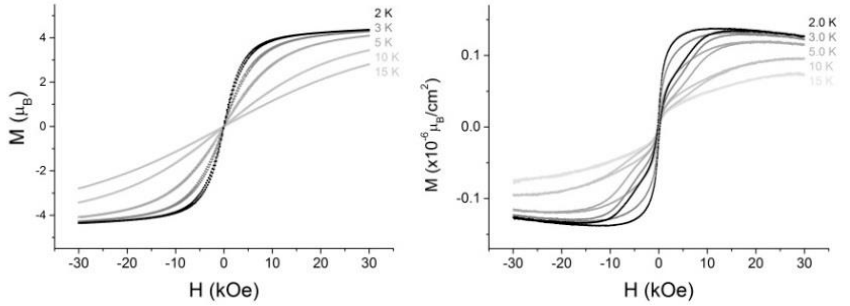

Fig. 27: Temperature dependence of the hysteresis loops recorded on the heated powder of $TbPc_2$ (left) taken out from the crucible before the sublimation of the molecules and on a film of $TbPc_2$ evaporated on Kapton (right). The data are reported per mole of $TbPc_2$ in (left) and per square centimetre of the film in (right). The field sweeping rate is 50 Oe s^{-1}. Reproduced from Ref. (Malavolti et al. 2013) with the permission from The Royal Society of Chemistry.

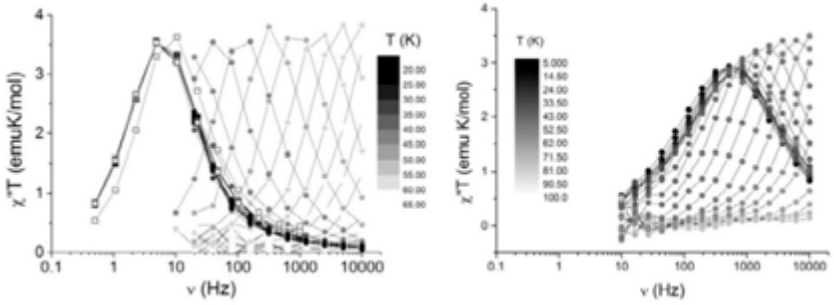

Fig 28: Frequency dependence of the product of temperature with the out-of-phase component of the magnetic susceptibility of $TbPc_2 \cdot CH_2Cl_2$ (left) and of the heated powder (right); measured in zero static field. Reproduced from Ref. (Malavolti et al. 2013) with the permission from The Royal Society of Chemistry.

Decreasing the temperature the maximum shifts to lower frequency and below 40 K no dependence is detected in agreement to the onset of the tunnelling regime between the two quasi-degenerate $m_J = \pm 6$ ground states (Branzoli et al. 2010). The

χ''curves were fitted by using the extended Debye model (Gatteschi et al. 2006; H.B.G. Casimir & du Pré 1938):

$$\chi'' = (\chi_T - \chi_S)\frac{(\omega\tau)^{1-\alpha}\cos(\pi\alpha/2)}{1+2(\omega\tau)^{1-\alpha}\sin\left(\pi\frac{\alpha}{2}\right)+(\omega\tau)^{2-2\alpha}} \quad (37)$$

where ω is the angular frequency, τ is the relaxation time, χ_T and χ_S are the isothermal and adiabatic limits respectively while the α parameter is related to the width of the τ distribution. The temperature dependence the τ distribution is depicted in fig. 29.

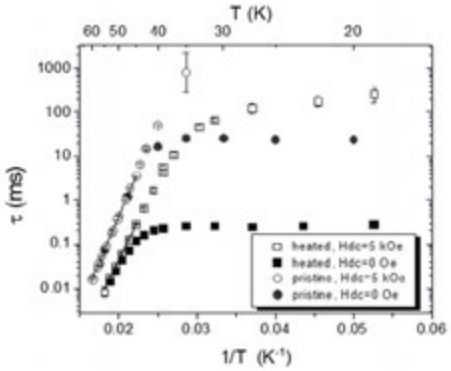

Fig 29: Temperature dependence of the relaxation time extracted from ac susceptibility data on the pristine (circles) and heated (squares) $TbPc_2$ samples. The empty symbols correspond to the measurement in a static magnetic field of 5 kOe. The black lines correspond to the best fit curves using the Arrhenius law on the high temperature data under a static magnetic field. Reproduced from Ref. (Malavolti et al. 2013) with the permission from The Royal Society of Chemistry.

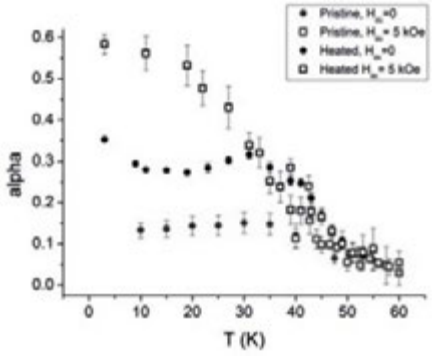

Fig 30: Temperature dependence of the parameter describing the width of the distribution of relaxation time extracted from the simulation of the out-of-phase component of the *ac* susceptibility according to the extended Debye model. Reproduced from Ref. (Malavolti et al. 2013) with the permission from The Royal Society of Chemistry.

Below 40 K the relaxation mechanism of both powders in zero field is dominated by tunnelling but the process in the heated powder is 10^2 faster (table 1). In fig. 30 are reported the α values vs T. It is interesting to note that in the tunnelling regime the α value is almost doubled, ca. 0.3 vs 0.15, in the heated sample, in agreement with its amorphous state.

By applying a static field of 5 kOe, which corresponds to the maximum hysteresis opening of the pristine sample, the tunnelling process is partially suppresses and a more precise analysis of the temperature dependence of the relaxation time can be performed. Above 40 K τ is found to follow the Arrhenius law, in agreement with previous experiments. However, while it levels off below 30 K in the heated powder, with a gradual increase of α, it continues to diverge, at least within the time window accessible in our experiment, for the pristine powder. This different behaviour justifies the disappearance of the hysteresis of the heated sample as due to a more pronounced tunnelling in field of the thermally treated sample. From table 1 we can notice that the activation barrier is slightly smaller for the heated sample. It should be however considered that the effects of the more pronounced tunnelling can influence the estimation of the barrier.

	τ_0(s)[a]	Δ(K)[a]	Γqt(s-1)[b]
Pristine	1.85(5)×10-12	965(20)	42
Heated	1.5(1)×10-12	856(20)	3660

a) Extracted from data taken at Hdc=5 kOe

b) Measured in zero static field.

Table 1: Parameters of the magnetisation dynamics extracted from *ac* susceptibility data for pristine and heated samples of $TbPc_2 \cdot CH_2Cl_2$.

These data highlight different relaxation dynamics operating in the two bulk samples, which differ in their structure i.e. microcrystalline and amorphous. The evaporated film shows a behaviour more similar to that of the pristine material. This observation suggests a more regular packing of the molecules in the film, a feature that is common to metal-phthalocyaninato (MPc)-based films, although the same crystal structure of the pristine compound cannot be achieved due to the loss of CH_2Cl_2 during the heating process.

In order to have some insight two different studies were carried out. A thick film of $TbPc_2$ evaporated on quartz was characterised by Magnetic Circular Dichroism (MCD) (see paragraph 2.6). Just for clarity of the discussion we anticipate that on all evaporated samples at least a preferential orientation of the molecules respect to the substrate surface is detected. This supports the presence of a certain degree of order inside the film that correlates to the magnetic properties. This is not surprising, in

fact Katoh et al. extensively investigated double and multi-decker lanthanide complexes and evidenced a significant dependence of the magnetisation dynamics on the crystal packing, suggesting a key role of Ln–Ln dipolar interactions (Katoh, Horii, et al. 2012). A similar trend has also been observed for other single ion slow relaxing species (Lopez et al. 2009; Rinehart & Long 2012), like Er^{3+} polyoxometalate (Luis et al. 2010) and the Dy^{3+} complex with the DOTA ligand (Car et al. 2011).

2.4 $TbPc_2$ in magnetic dilution environment

In order to have some insight on the role played by intermolecular interactions a dilution study was performed. It is well know that the magnetisation dynamics is sensitive to dilution in diamagnetic hosts (Abragam & Bleaney 1986). The tunnelling efficiency strictly depends to the relative energies of the levels on the opposite side of the anisotropy barrier. The local dipolar fields generated by other $TbPc_2$ molecules can modify the gap energy of the levels involved in the tunnelling process. This dipolar interaction mechanism is particularly efficient in case of the fields aligned to the easy axis of the molecule, which can tune the gap energy by bringing the levels in or out of resonance; thus modifying the magnetisation dynamics (Gatteschi et al. 2006). On the other hand exchange interactions, which can be mediated by the unpaired electron residing on the phathalocyanine rings, must be taken in account. The dilution in diamagnetic hosts leads to an insulation of the $TbPc_2$ molecules hindering the dipolar interaction as well as the exchange ones.

Two types of dilution were performed by dispersing the pristine powder of $TbPc_2{\cdot}CH_2Cl_2$ in a Poly(methyl methacrylate) (PMMA) polymeric matrix and by preparing Tb-doped YPc_2 sample. The PMMA matrix was preferred respect to a frozen solution for practical purposes. In fact, during the formation of the dispersed sample, either by polymerization or by cooling down the diluted solution, the formation of micro-crystallites can occur. The polymeric matrix allows inspection by optical microscope and X-ray micro-analysis in order to check their formation, while for a frozen solution the same characterisation is more complicated.

By employing these techniques the threshold concentration for the micro-crystallites formation was estimated above 0.2 wt %, within the resolution limit of 700 nm of the X-ray micro-analysis. The hysteresis loops recorded for two samples, namely 1 wt % and 0.2 wt %, are depicted in fig 31. The concentrated sample presents the micro-crystallites formation while no crystallites were revealed for the diluted one. The reported data are not corrected by the diamagnetic contribution of the polymeric matrix, which is more pronounced in the diluted sample. Nevertheless significant differences are evidenced. The concentrated sample shows a hysteresis opening already at 15 K and the presence of significant butterfly hysteresis at lower temperature. It is also interesting to note the no linearly dependence of the area in-

side the hysteresis on the temperature for the concentrated sample. This behaviour is similar to that observed for the pristine microcrystalline powder. On the contrary the proper diluted sample (0.2 wt %) shows no hysteresis opening above 5 K and a less pronounced tunnelling relaxation in zero field. This findings is in agreement to that observed by MCD experiments on a frozen solution of $TbPc_2$ in CH_2Cl_2 (Gonidec et al. 2010), and suggests that an efficient magnetic insulation of these SMMs induces a reduction of the tunnelling probability.

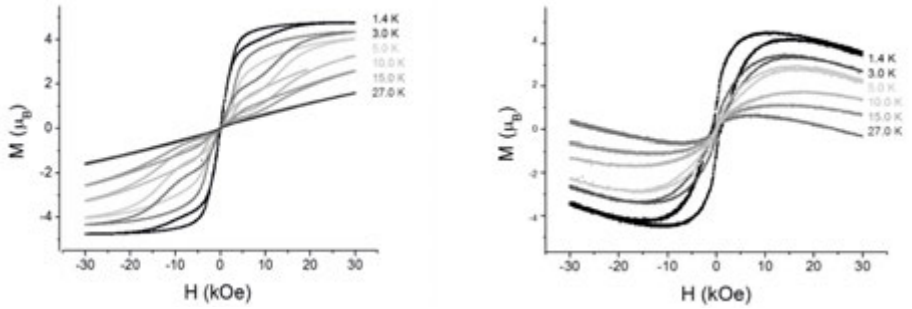

Fig. 31: Temperature dependence of the hysteresis loops recorded on $TbPc_2{\cdot}CH_2Cl_2$ dispersed in PMMA at 1% in weight concentration (left) and 0.1% (right). In the 1 % sample aggregates are formed. The data are reported per mole of $TbPc_2$ and the field sweeping rate is 50 Oe s^{-1}. Reproduced from Ref. (Malavolti et al. 2013) with the permission from The Royal Society of Chemistry.

In the second experiment a solid solution of $TbPc_2$ in $YPc_2{\cdot}CH_2Cl_2$ was prepared. In order to achieve 10:90 $TbPc_2$:YPc_2 ratio the synthesis reported in paragraph 2.1 was employed. $YPc_2{\cdot}CH_2Cl_2$ crystals are isomorphous to the $TbPc_2$ analogue and they show a paramagnetic behaviour due to the unpaired electron on the phathalocyanine rings. In the right part of the fig. 32 the temperature dependence of the hysteresis loops of the $Tb_xY_{1-x}Pc_2{\cdot}CH_2Cl_2$ is reported to be compared to the reference data of the pristine $TbPc_2{\cdot}CH_2Cl_2$ sample (fig. 25 left). The diluted data are not corrected for the paramagnetic behaviour of the YPc_2 molecules and they are plotted for mole of $TbPc_2$; therefore the magnetisation value results higher because the paramagnetic contribution of ca. 9 moles of the YPc_2 radicals is added for each $TbPc_2$ mole. However, as far as hysteretic behaviour is concerned, no significant differences are observed.

This remarkable finding suggests that dipolar interactions, due to neighbouring Tb^{3+} ions, do not significantly influence the magnetisation dynamics of $TbPc_2$ in the investigated temperature range. This is in contrast to some differences observed by Ishikawa et al. (Ishikawa et al. 2005) in the mK temperature region and to what reported for the octabutoxy-phthalocyaninato derivative (Katoh, Horii, et al. 2012).

Although the dipolar interactions, significantly reduced in the doped system, are not significantly affecting the relaxation dynamics, nothing can be said about the intermolecular exchange interactions. These are in fact mediated by the π stacking of Pc ligands and are therefore expected to be partially active also in the $Tb_xY_{1-x}Pc_2 \cdot CH_2Cl_2$ sample.

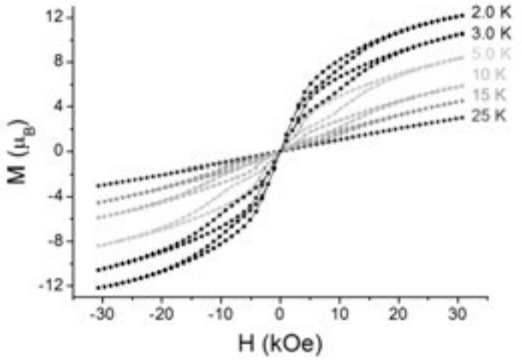

Fig. 32: Temperature dependence of the hysteresis loops recorded on $Tb_xY_{1-x}Pc_2 \cdot CH_2Cl_2$. The data are reported per mole of $TbPc_2$ and the field sweeping rate is 50 Oe s^{-1}. Reproduced from Ref. (Malavolti et al. 2013) with the permission from The Royal Society of Chemistry.

2.5 Evaluation of the exchange interaction

In order to investigate the role of the exchange interactions in the dynamic relaxation process of $TbPc_2$ SMMs in different packing environments the YPc_2 derivative was chosen as reference. It has been already mentioned that this is a paramagnet molecule isostructural to $TbPc_2$. It is thus reasonable to assume that the exchange intermolecular interactions in the YPc_2 and $TbPc_2$ are comparable, with the latter experiencing also significant dipolar interactions due to the large moment of Tb^{3+}.

It is known that the $YPc_2 \cdot CH_2Cl_2$ crystals at intermediate temperatures show a weak ferromagnetic interaction between molecules aligned along the crystal columns, while below 1.35 K the onset of three-dimensional antiferromagnetic (AF) order is observed (Paillaud et al. 1991). On the contrary, YPc_2 crystallizing in the $P2_12_12_1$ space group, which correspond to the crystalline phase without the CH_2CH_2 solvent, exhibits AF interaction in the whole range of temperature as reported by Paillaud et al. (Paillaud et al. 1991) and recently confirmed by solid state NMR characterisation (Branzoli et al. 2011).

We decided therefore to investigate how the sublimation process influences the exchange interactions between YPc_2 radicals. The χT products of the pristine $YPc_2 \cdot CH_2Cl_2$ microcrystalline powder, which shows the expected ferromagnetic behaviour in the investigated temperature range, is reported in fig. 33 (triangles). The

χT product for the heated powder and for a film prepared by sublimation of YPc_2 on Teflon tape are also reported in fig. 33, circles and squares respectively. The χT product of heated powder decreases by decreasing the temperature. Thus, it shows the expected antiferromagnetic behaviour for YPc_2 powder without CH_2Cl_2 molecules of crystallization (Paillaud et al. 1991). Since the YPc_2 susceptibility is ca. 40 times smaller than that of $TbPc_2$ the detection of sublimated films is quite challenging. In order to achieve a suitable micrometric film thickness a long sublimation process was carried out on micrometric film of Teflon tape. This minimises the diamagnetic contribution of the substrate. Although less pronounced than in the heated powder case, the χT product dependence on the temperature of the film shows intermolecular antiferromagnetic interactions. The data were fitted by using the Curie-Wiess law:

$$\chi = \frac{C}{T-\theta} \qquad (38)$$

The Weiss constants θ extrapolated are 0.22(1) K, -4.1(1) K, and -2.5(1) K for the pristine powder, heated powder, and evaporated film, respectively.

Assuming that the intermolecular exchange interactions between the paramagnetic ligands are comparable in isostructural $TbPc_2$, our observation suggests that no clear correlations exist between the strength and nature of these interactions and the disappearance of hysteresis in the heated $TbPc_2$ sample.

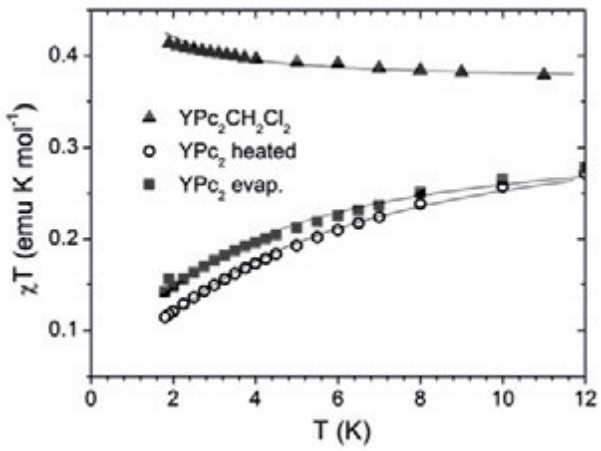

Fig. 33: Temperature dependence of the relaxation time extracted from ac susceptibility data on the pristine (triangles) and heated (circles) $TbPc_2$ samples. The empty symbols correspond to measurement in a static magnetic field of 5 kOe. The lines correspond to the best fit curves obtained using the Curie–Weiss law. Reproduced from Ref. (Malavolti et al. 2013) with the permission from The Royal Society of Chemistry.

It is now evident that a more accurate characterisation of the sublimated molecular films of $TbPc_2$ is mandatory in order to understand its peculiar magnetic behaviour, i.e. the observation of a hysteretic behaviour not observed in the heated powders used to evaporate the film. We will present later more detailed investigations based on large scale facilities such as the Swiss muon source, which can provide insight on the magnetic properties of the evaporated films. We discuss here *in house* Magnetic Circular Dichroism (MCD) investigations. Although MCD cannot offer the same potentiality of the formerly mentioned large scale facilities techniques, it is able to provide interesting information concerning the preferential molecular orientation respect to the substrate surface.

2.6 Magnetic Circular Dichroism of $TbPc_2$ sublimated on quartz

We performed angle-resolved Magnetic Circular Dichroic (MCD) spectroscopy at room temperature under 13 kOe of applied field on a film of thickness (ca. 200 nm, thus equivalent to that of previously investigated samples) evaporated on a diamagnetic quartz substrate hold at room temperature (Campo 2012). The spectra were acquired for three different values of the ϕ angle formed by the magnetic field and propagation vector of the light with the normal to the surface, namely ϕ= 0°, 22°, 45°. The data, reported in fig 34, are compared to those obtained for a CH_2Cl_2 solution of the complex, taken as an isotropic reference.

We focused our attention on the Q-band region of $LnPc_2$ molecules around 670 nm, related to the family of $\pi^*\rightarrow\pi$ transitions centred on the Pc^- ligands. Such transitions are known to be polarised on the Pc plane, thus giving precious information on the orientation of the molecule (Bräuer et al. 2009). A strong angular dependence is observed in the evaporated sample, the shape of the MCD evolving from dispersive- to absorptive-like. If we compare the three spectra of the evaporated sample with that of the solution, we notice that the line shape evolution likely originates from the relative weight of different spectral components which can all be found in the isotropic MCD spectrum. This suggests a more complex structure of the electric dipole orientations in the Q-band of $TbPc_2$ with respect to the simple Pc ligand. While this topic needs further dedicated studies, it is clear that molecular orientation is responsible for this angle-dependent behaviour.

In order to gain further insight on the anisotropy of the evaporated film we studied the field dependence of the MCD signal measured at λ= 605 nm and T = 1.8 K. The observation of the magnetic behaviour through π optical transitions of the ligand is due to a partial hybridization of these orbitals with those of the metal (Dunford et al. 2000). As shown in fig. 35, the typical butterfly hysteresis is found at ϕ= 45°; for ϕ= 0°, however, the hysteresis loop closes significantly, suggesting that $TbPc_2$ molecules organize themselves in the evaporated film with their tetragonal

symmetry axis lying in the plane of the substrate. A preferential orientation of $TbPc_2$ on oxide surfaces in the standing configuration, characterises simpler Pc molecules and confirms previous experiments on $TbPc_2$ based on synchrotron radiation (Margheriti et al. 2010). Observation of a hysteresis seems therefore to be associated with the order in the crystal packing also not directly related to dipolar or exchange interactions.

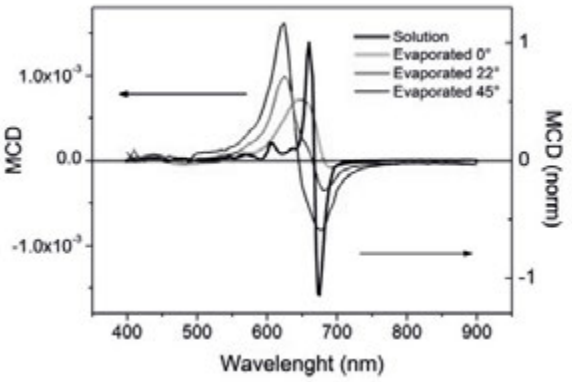

Fig. 34: Room temperature MCD spectra (under 13 kOe applied field) of $TbPc_2$ as a CH_2Cl_2 solution and as 200 nm evaporated film at different angles of incidence of the light with respect to the surface normal. Reproduced from Ref. (Malavolti et al. 2013) with the permission from The Royal Society of Chemistry.

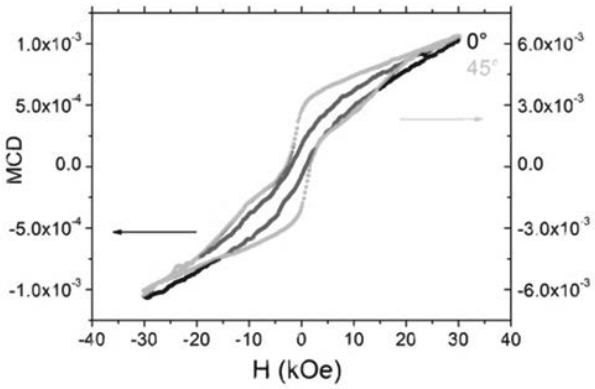

Fig. 35: Low temperature (1.8 K) MCD hysteresis loops of a 200 nm $TbPc_2$ thin film evaporated on quartz. The loops were recorded at λ= 605 nm and with light incidence of 0° (black) and 45° (grey) with respect to the surface normal. The sweeping rate is 150 Oe s^{-1}. Reproduced from Ref. (Malavolti et al. 2013) with the permission from The Royal Society of Chemistry.

3 Characterisation of thick films through low-energy implanted muons

In the previous paragraphs a magnetic characterisation of the pristine and heated powders has been reported. In order to complete the magnetic characterisation of the sublimated films and shed some light on the different behaviour of thin and thick films Low-Energy implanted Muon Spin Relaxation (LE-μSR) experiments were carried out. The investigation was performed thanks to the collaboration with Dr. Zaher Salman of the Paul Scherrer Institute (PSI), whose group carried also out the data analysis.

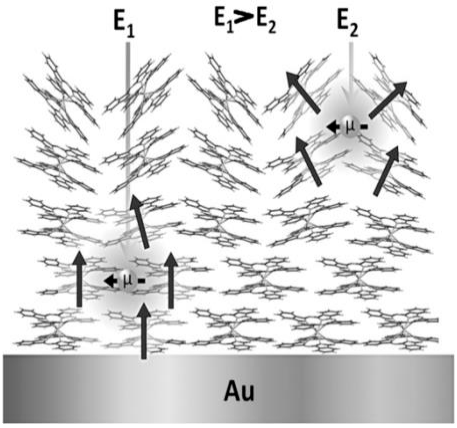

Fig. 36: Schematic of a typical LE-μSR experiment. Fully spin-polarised muons are implanted with energy E into a thin film of $TbPc_2$ and sense the dipolar magnetic fields of neighbouring SMMs. The muon mean implantation depth is proportional to their energy E.

The unique properties of this technique allow a depth characterisation of the dynamics of the magnetic moments inside the films. Before starting our discussion a brief introduction to the basic concepts of the technique is presented here. Muons can be employed as local probe to detect dipolar fields. In fact, the positive muons are leptons with charge +e, spin $1/2$, rest mass mμ= 207me and a gyromagnetic ratio $\gamma/(2\pi)$ of= 135.5 MHz/T. A 100% polarised beam of muons can be generated and focalised on the investigated sample. The penetration depth of the muons depends on their energy, i.e. the more energy the more are penetrating (fig. 36).

The muons are affected by the local fields inside the sample, which induces a change in the initial polarisation i.e. the muons magnetic moments precess around the local static field. However, they are not long living particles (mean lifetime is 2.2 μs) and after a time of the order of few μs they decay:

$$\mu^+ \rightarrow e^+ + \upsilon_e + \bar{\upsilon}_\mu \qquad (39)$$

this decay includes the emission of an electron neutrinos υ_e, a muon antineutrinos $\bar{\upsilon}_\mu$ and a positron e^+.

Positrons are preferentially emitted along the muons' spin polarisation at the moment of the decay (fig. 37). In fact, the probability of the positrons emission in a direction forming a θ angle with the muon polarisation can be calculate as:

$$W^+(\theta, \varepsilon) = 1 + A^+(\varepsilon)\cos\theta \qquad (40)$$

where ε is the energy of the positron and A^+ is the asymmetry. Thus, counting the spatial distribution of the emitted positrons allows to follow the time evolution of the muons polarisation. From this data is thus possible to get information on the local field experienced by the muons.

In these experiments, fully spin-polarised muons are implanted into the sample and used as a local probe to detect dipolar fields from the surrounding molecules. They provide the direct observation of the spin dynamics of individual SMMs.

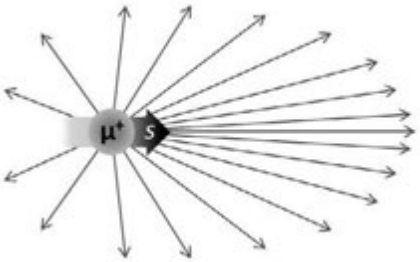

Fig. 37: Preferential emission of the positron along the polarisation axis of the muon.

In this study three samples were investigated: (1) a microcrystalline powder sample of $TbPc_2 \cdot CH_2Cl_2$, (2) a thick (ca. 1 μm) and (3) a thinner film sample (ca. 100 nm). The films were evaporated onto 200 nm polycrystalline gold films grown on freshly cleaved Muscovite mica substrates. The thickness of the film was estimated by Atomic Force Microscopy (AFM) with the standard scratch method and cross-checked by magnetometry measurements. The sublimation rate was estimate using the following procedure. A $TbPc_2$ film was sublimated on quartz for at list one hour. The sample was then undergone to scratch and AFM investigations. The scratch procedure was carried out by using a thin needle in order to selectively remove in the scratched area (ca 40μm per several mm) the $TbPc_2$ deposit from the quartz substrate. The AFM was then used to trace the step profile and get the thickness information. Thus the thickness allows the calculation of the deposition rate. It's important to note that for film deposited on Au(111) grown on mica this procedure cannot be employed because the substrate is not hard enough and it can be damaged

by the scratch procedure. During the samples preparation it was impossible, for geometric reason, to prepare in parallel films on Au(111) and on a quartz substrate because the size of sample required for μSR is very large (3 cm of diameter disks). This made impossible a direct scratch measure of the sample thickness. However, the deposition rate during the film growth was estimated by measuring the sublimation rate before and after the sample preparation. The thickness data were then cross-checked after the muon experiment by magnetometry measurements. To do that each $TbPc_2$ film was re-solubilised in CH_2Cl_2. The solution was dried onto a stretched Teflon tape to obtain the $TbPc_2$ solid which was investigated by standard magnetometry. The saturation magnetisation of the sample M_{sample} was then measured. Knowing the molar magnetisation M it was possible to get the total mass of the sample as:

$$Mass = \frac{M_{sample}}{M} \cdot M_w \qquad (41)$$

where M_w is the molecular weight. Thus knowing the surface area of each sample and the density of the $TbPc_2$ film it was possible to calculate the thickness. This thickness estimation was found in good agreement with the one obtained from AFM experiment (96 nm vs 107 nm for thinner film).

The muon spin relaxation curves obtained for the microcrystalline powder and the thick film sample in zero field, where in ordinate the measured asymmetry is reported, are represented in fig. 38. The measurements in both samples show a remarkable qualitative similarity in the whole temperature range. In high temperatures, i.e. above 100 K the curves show an exponential-like relaxation from the initial value to zero. At 4.2 K the asymmetry exhibits a dip at early times (inset of fig. 38), followed by a recovery and then relaxation at longer times. The slowly relaxing tail indicates that the internal magnetic field experienced by the implanted muons in $TbPc_2$ contains two contributions: a static component and a dynamic component. The static and dynamics terms are relative to the $\upsilon/(\gamma\delta)$ ratio, where the υ is the fluctuation rate of the dynamic magnetic field, $\gamma/(2\pi)$= 135.5 MHz/T is the muon's gyromagnetic ratio, and δ is the width of static magnetic field distribution sensed by the muons. The static case is approached when the ratio is $\ll 1$, while the fast fluctuation limit is approached when the ratio is $\gg 1$. When muons experience a distribution of static magnetic fields with an additional dynamic component, the muon spin relaxation curve can be described by the phenomenological static Kubo-Toyabe function, multiplied by a suitable dynamic relaxation (Fudamoto et al. 2002; Salman et al. 2010). The form of the Kubo-Toyabe function depends on the distribution of the static field sensed by the implanted muons, e.g., Gaussian or Lorentian.

$$A(t) = \frac{A_0}{3}\left[1 + 2(1-\gamma\delta)e^{-\gamma\delta t}\right]e^{-\sqrt{\lambda t}} \qquad (42)$$

where A_0 is the initial asymmetry and λ is the relaxation rate, which contains information regarding the dynamics of the local field. The square root relaxation reflects the averaging of the relaxation behaviour of muons stopping in many non-equivalent sites (Uemura et al. 1985; Lascialfari et al. 1998; Salman et al. 2002; Blundell et al. 2003; Branzoli et al. 2009; Branzoli et al. 2010). By fitting the data with the above mentioned equation the parameters λ and δ were obtained and their temperature dependence is shown fig. 39.

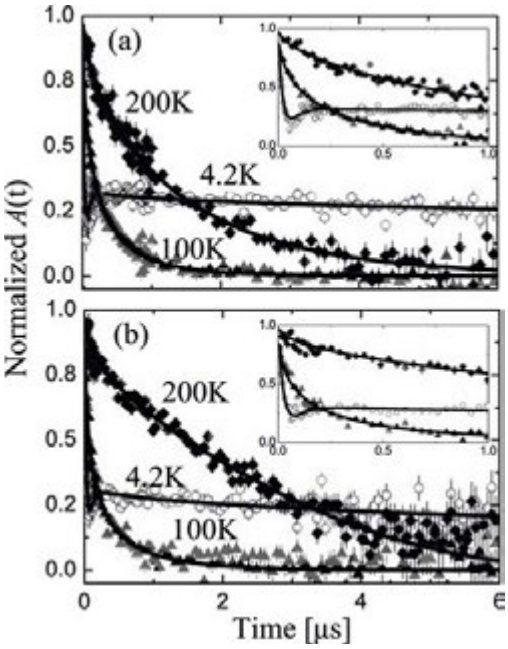

Fig. 38: Typical muon spin relaxation curves in the (a) bulk and (b) thick film samples measured in zero applied field and at various temperatures. The insets show the early time relaxation, where the dip in the relaxation can be clearly seen at low temperatures. The lines are fits to equation 42. Reprinted with the permission from (Hofmann et al. 2012). Copyright (2012) American Chemical Society.

It is important to note that the results obtained for the microcrystalline powder are consistent with previous muon spin relaxation measurements (Branzoli et al. 2010). The qualitative similarity between bulk and films behaviour is an indication that SMM nature of the $TbPc_2$ in the film is retained. The static and the dynamic behaviour in all the three samples are in fact characterised by three different temperature regimes. At high temperature λ is small and δ is ca. zero. As the temperature is decreased λ increases sharply while δ remains zero. At ca. 100 K, λ peaks and δ be-

comes non zero. Finally, below ca. 50 K both the parameters saturate and become temperature independent. However, quantitative differences are observed at low temperature between the microcrystalline powder and the films; for example, the saturation value of δ is ca. 42 mT in the powder and ca. 24 mT in the film samples. It is important to point out that δ is equal in both film samples throughout the whole temperature range and is even independent of the muons' implantation energy. At high temperature, λ, which is directly related to the spin dynamics, is also equal in both films and is E independent. However, at low temperature, and only in the thin (nominally 100 nm) film, it strongly depends on E.

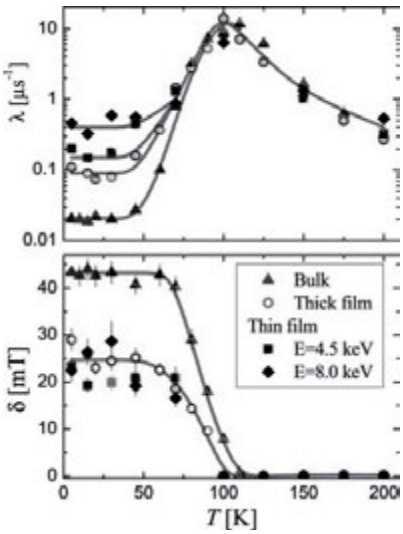

Fig. 39: λ (top) and δ (bottom) as a function of temperature in bulk, thick and thin film samples obtained from fits of the relaxation curves to equation 42. The lines are a guide to the eye. Reprinted with the permission from (Hofmann et al. 2012). Copyright (2012) American Chemical Society.

We consider first the static magnetic field experienced by the muons. At high temperatures, δ is ca. zero reflecting the absence of static fields as a consequence of fast thermal fluctuation between the ground ($J_z = \pm 6$) and the first excited ($J_z = \pm 5$) spin states. The saturation of δ at low temperature indicates that muons experience a temperature-independent distribution of static fields. In fact, at this temperature we expect all the molecules to reside in the ground state, since the energy gap to the next excited state is more than 650 K. Information regarding the dynamics of the local field can be extrapolated from λ. The exponential increase as the temperature is decreased in the high temperature regime demonstrates the slowing of spin dynamics. This is due to the reduced probability of spin-phonon-mediated transitions between different spin states (Lascialfari et al. 1998; Villain et al. 1994; Salman 2002). The

small difference in the λ value between the microcrystalline powder and the films in this temperature regime implies that the energy gap between the ground and the first excited state does not change significantly. This is a direct evidence that there is almost no change in the crystal field of the Tb^{3+} ions between microcrystalline powder and films. In contrast to this behaviour, the saturation of λ at low temperature is a consequence of persistent spin dynamics at temperatures far below the energy gap. This is attributed to quantum tunnelling between the two quasi-degenerate $J_z = \pm 6$ ground states (Branzoli et al. 2009; Branzoli et al. 2010), which is particularly efficient in zero applied magnetic field, corresponding to the condition of our experiment. Interestingly, in fig. 39 one can observe a clear difference in the saturation value of λ depending on the sample: bulk, thick or 100 nm film. Moreover, in the 100 nm film it also depends on the muons' implantation energy/depth.

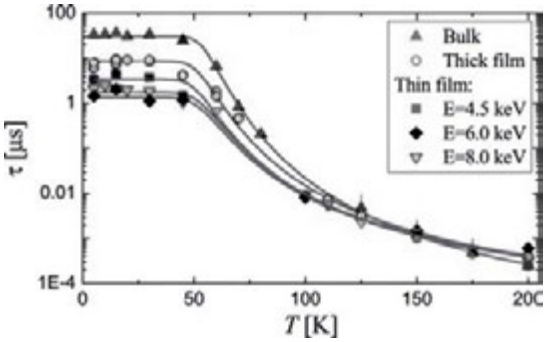

Fig. 40: Correlation time as a function of temperature measured in bulk and $TbPc_2$ films. The lines are fits to equation 44. Reprinted with the permission from (Hofmann et al. 2012). Copyright (2012) American Chemical Society.

In what follows we extract the correlation time of the molecular spin dynamics as a function of temperature. At low temperatures where $\gamma\delta > \lambda, A(t)$ is almost identical to the dynamic Lorentzian Kubo-Toyabe function, and hence $\lambda = (2/3\tau)$ (Uemura et al. 1985; Hayano et al. 1979), where τ is the correlation time of the local magnetic field experienced by the muon, which in our case is that generated by the $TbPc_2$ SMMs. However, at high temperatures, where δ is ca. 0, the relaxation rate can be written as $\lambda = 2\tau(\gamma\delta_0)^2$ (Uemura et al. 1985; Hayano et al. 1979), where δ_0 is the size of the fluctuating field at the measured temperature. Note that the SMMs are in their ground J = 6 manifold throughout the measured temperature range. Therefore, δ_0 can be evaluated from the low-temperature saturation value, $\delta_0 = \delta(T \rightarrow 0)$, which reflects the size of the dipolar field from the magnetic moment of a single $TbPc_2$ molecule. Thus, we can readily extract τ as a function of temperature in the high and low-temperature ranges, as shown in fig. 40.

The probability (or inverse correlation time) of phonon-induced transitions between the $J_z = \pm 6$ and $J_z = \pm 5$ states is (Lascialfari et al. 1998; Villain et al. 1994; Salman 2002):

$$\frac{1}{\tau_{sp}} = C\Delta^3 \exp\left(\frac{\Delta}{T}\right) \qquad (43)$$

where C is a temperature-independent parameter that represents the spin-phonon coupling strength and Δ is the energy gap between the spin states. This accounts for the observed high-temperature dependence of τ, but given the exponential dependence and the large value of Δ, no spin dynamics is expected at low temperatures. However, in the low-temperature regime of our muon spin relaxation data we find that τ is finite and temperature- independent. In order to model these results, we add a phenomenological constant contribution at low temperatures, τ_q, which reflects the contribution of quantum tunnelling to the correlation time. Thus, the full probability for transitions between different sublevels of the J = 6 manifold is (Salman 2002):

$$\frac{1}{\tau} = \frac{1}{\tau_{sp}} + \frac{1}{\tau_q} \qquad (44)$$

A fit of the results to this model provides the values for Δ, C, and τ_q given in table 2. We find that Δ is similar in all samples and exhibits no implantation energy dependence, as expected from the similar high-temperature behaviour in τ. This confirms that the crystal field experienced by the Tb ions does not depend on sample or depth in the films. The values of C vary significantly between the different samples. This is to be expected between bulk and films, given the loss of solvent molecules of CH_2Cl_2 (Paillaud et al. 1991) and the probable formation of a different molecular order in the films. These effects modify the phonon spectrum dramatically and, therefore, affect the value of C. However, the difference between the thick and 100 nm film is surprising, but may also be due to the effect of film thickness on the phonon spectrum when it is decreased from the micrometer to the nanoscale.

Parameters	Bulk	Thick film (~1μm)	Thin film (~100nm)
C [10^{-14}/μs·K^3]	6.2±2.5	1.1±0.2	0.51±0.22
Δ [K]	877±30	790±10	640±30
τ_q	31.2±1.6	6.6±0.2	See fig. 41

Table 2: Summary of parameters from fits of τ as a function of T to equation 44.

Most importantly, we note that only in the thin film we find a clear E/depth dependence of τ_q, as shown in fig. 41. To establish a clear relation between the muons'

implantation energy and the mean/root mean squared (rms) stopping depth in the $TbPc_2$ film (fig. 41), Trim. SP simulations (Eckstein 1991) were used to model experimental measurements. First, the fraction of the asymmetry was determined from muons stopping in the gold substrate as a function of E. For this purpose, $A(t)$ was measured in a magnetic field, B, applied transverse to the initial spin of the muons. At 5 K muons stopping in the $TbPc_2$ film depolarise very rapidly due to the large internal fields, while muons stopping in nonmagnetic gold experience predominantly the applied transverse field and, therefore, precess at the Larmor frequency, γB.

The normalized fraction of precessing signal as a function of E is plotted in fig. 42. Next, the muon stopping depth profile in a $TbPc_2$ film of density ρ ca. 1.5 ± 0.1 g·cm^{-3} was simulated. We further assume that our muon beam (radius ~1cm) impinges on a film with thickness cross-section profile as illustrated in the inset of fig. 42, which is suggested by AFM measurements. Best fit to the experimental data is obtained using a film with a nominal thickness of ~100 nm, which falls gradually to ~50 nm at the edges of the beam spot. Note that this method of implantation depth estimate has many potential systematic uncertainties due to the non-uniform thickness profile and density of the film.

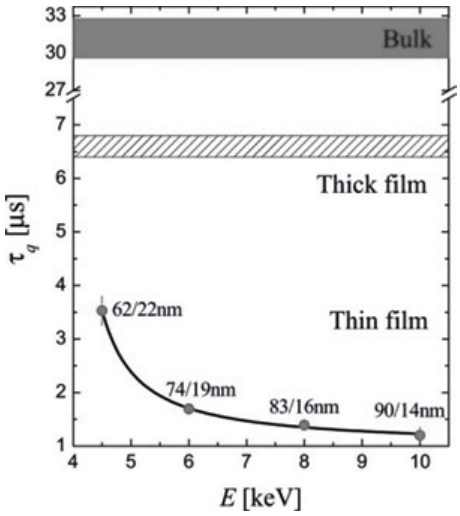

Fig. 41: τ_q as a function of E (and corresponding mean/rms implantation depth) obtained from fits of τ as a function of temperature to equation 44. The solid-shaded and hatched areas represent the values (and uncertainty) in the bulk and the thick film samples, respectively. Reprinted with the permission from (Hofmann et al. 2012). Copyright (2012) American Chemical Society.

However, this treatment gives a rough idea of the depth dependence of τ_q as reported in fig. 41. Here, the values of τ_q are basically a weighted average of the corre-

lation time of the $TbPc_2$ molecules over the full stopping depth distribution of the implanted muons, which provides qualitative information regarding its depth dependence. Interestingly we notice that the depth dependence extends to a scale of several tens of nm away from the gold surface.

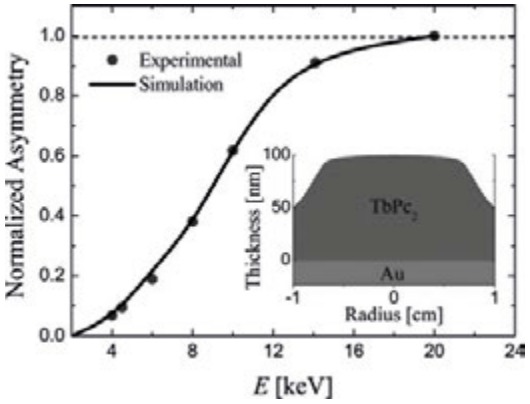

Fig. 42: Normalized fraction of muons stopping in the Au substrate as a function of E. The solid line is the estimated value from Trim.SP simulations using a $TbPc_2$ film with a nominal thickness of~100nmand a cross-section profile as illustrated in the inset. Reprinted with the permission from (Hofmann et al. 2012). Copyright (2012) American Chemical Society.

As mentioned in the paragraph 1 the starting point of these studies were the XMCD and XNLD measured on a $TbPc_2$ thick film and on the monolayer by Margheriti et al. (Margheriti et al. 2010). The different magnetic behaviour of the two samples was attributed to a competition between molecule-substrate and molecule-molecule interactions. It's now interesting to compare the muon spin relaxation data to previous measurements. The XMCD and XNLD techniques are sensitive only to the top few monolayers and they do not provide details of the depth dependence of the $TbPc_2$ magnetic and structural properties. Muon spin relaxation measurements complement the magnetic characterisation by revealing a significant depth dependence of the molecular spin dynamics as far as several tens of nm from the surface. In particular, τ_q is small for high E, i.e., near the gold surface and becomes larger as we probe molecules further away from the substrate, gradually approaching the value measured in the thick film where all muons stop far from the substrate (few 100's nm away). The data are in agreement with the XMCD detected hysteresis loops which show no hysteresis opening in monolayer samples (Stepanow et al. 2010; Margheriti et al. 2010; Lodi Rizzini et al. 2011) and the recovery of the hysteresis opening in the thick film (Margheriti et al. 2010). This finding, in conjunction with the different orientation of the molecules highlighted by XNLD in thick and monolayer films, suggests that molecule-molecule interactions play a key role in the magnetisation dynamics of the $TbPc_2$ films. In fact the depth dependence of τ_q may be related to a

gradual variation of the molecular packing from the lie down geometry in proximity of the metal substrate to the standing up characterising the top layers of the thick film. It is important to note that this interpretation is in agreement with what shown in the previous paragraph about pristine and heated powder.

4 Toward $TbPc_2$ spintronic devices

4.1 Introduction

$TbPc_2$, as well as all SMMs, have been a workbench for the study of quantum effects in magnetism (Gatteschi et al. 2006); more recently these systems have attracted a growing interest as active elements in organic spintronic devices (OSPDs) (Dediu et al. 2009). These generally consist of a semiconductor organic film located between two ferromagnetic electrodes, one acting as spin injector and the other as spin analyser (Dediu et al. 2009) (fig. 43).

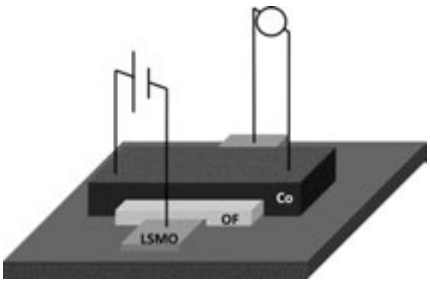

Fig. 43: Schematic representation of a vertical spin valve device. The organic film (OF) is stratified between the two ferromagnetic electrodes of cobalt (spin injector) and Lanthanum Strontium Manganite Oxide (LSMO)(spin analyser).

Recent studies, employing tris(8-hydroxyquinolinato) aluminium (Alq_3) organic film, have shown how OSPDs can be designed to behave as spin valves or "memristor" (Prezioso et al. 2013) where the non-volatile resistence of the device can be tuned and depends on the hystoric current and bias voltage applied. Recent electric transport studies involving SMMs are based on single molecules transistor (Heersche et al. 2006; Jo et al. 2006) where the molecule is placed between two non-magnetic electrodes. On the other hand Urdampilleta et al. have recently obtained a supramolecular spin valve (Urdampilleta et al. 2011) employing $TbPc_2$ molecules deposited on a carbon nanotube. At best of our knowledge, SMMs have not yet been employed as organic film in macroscopic spin valve devices.

In OSPDs the molecules-electrode interface plays a key role to define the final device properties (Sanvito 2011). Therefore, the knowledge of the magnetic

behaviour of the interface is mandatory in order to move toward OSPDs incorporating $TbPc_2$ or other SMMs as organic film.

Two of the most employed electrode materials in OSPD are the Lanthanum Strontium Manganite Oxide (LSMO) used as spin injection and the metallic cobalt as spin analyser (Dediu et al. 2009). The study of the molecules-electrode interfaces, i.e. $TbPc_2$/LSMO and $TbPc_2$/Co, has been here splitted and two hybrid surfaces, obtained by sublimation of the $TbPc_2$ on the ferromagnetic electrode surfaces, have been studied separately. This investigation has been carried out by employing the element selectivity and surface sensitivity of X-ray Absorption Spectroscopy (XAS) and related techniques, like X-ray Magnetic Circular Dichroism (XMCD) (see section 2 paragraph 5), which allows to distinguish the magnetic signal of the $TbPc_2$ film from the bigger one coming from the substrate. XMCD has been already successfully employed on $TbPc_2$ and for other SMMs deposited on different surfaces (Stepanow et al. 2010; Lodi Rizzini et al. 2011; Lodi Rizzini et al. 2012; Margheriti et al. 2010; Mannini et al. 2008; Sönke Voss et al. 2008; Mannini et al. 2009; Mannini et al. 2010).

4.2 $TbPc_2$/LSMO/STO hybrid surface

The characterisation of such hybrid surface has been preliminary reported by Margheriti (Margheriti 2010). Herein it is reported only a brief summary just for the clarity of the discussion. LSMO is a perovskite manganite of formula $La_{1-X}Sr_XMnO_3$ which, for determined X values (for example 0.3), shows an excellent magnetic polarisation at room temperature (Dediu et al. 2002). Its stability under different conditions allows the preparation of *ex situ* samples. The LSMO substrates employed in our study were made by channel spark ablation from a stoichiometric polycrystalline target in partial oxygen atmosphere ($P=4x10^{-2}$ mbar) (Graziosi et al. 2013) and grown on strontium titanate (STO) subtrate.

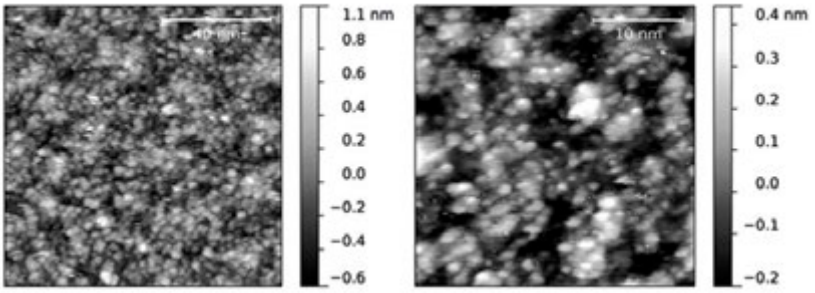

Fig. 44: STM images of 12 nm LSMO on STO, the surface was annealed 30 minutes at 250°C in UHV before being investigated. 100x100 nm^2 (left) and 30x30 nm^2 (right) both acquired with 50 mV bias and 50 pA of current.

The STM investigation carried out on a LSMO after that the surface was annealed at 250°C for 30min in UHV is reported in fig. 44. The images reveal a granular surface with average height of ca. 1 nm (RMS roughness 0.29 nm). Most outgrowths show lateral dimensions comparable with those of the $TbPc_2$ molecules (ca. 1.5 nm). Thus, the surface corrugation does not allow the STM characterisation of sub-monolayer $TbPc_2$ films.

The X-ray absorption spectroscopy characterisation was performed at the SIM-X11MA beamline at the Swiss Light Source (SLS) synchrotron facility by *in situ* deposition of a thin molecular layer. The LSMO substrate, consisting in a 12 nm LSMO film grown on strontium titanium oxide (STO), was cleaned by sonication in isopropanol before being used. The molecular sublimation was carried out using the device described in section 2 paragraph 2. A thin film of $TbPc_2$ was sublimated *in situ* in UHV condition on 12 nm thick film of LSMO substrate. The XAS investigation of the hybrid surface was performed at the Mn $L_{2,3}$ and Tb $M_{4,5}$ edges. The spectra were acquired in total electron yield mode using both linearly and circularly polarisation light. The magnetic field was applied along the photon propagation vector (fig. 45 left) and at variable angle, θ, with the normal to the surface (fig. 45 right).

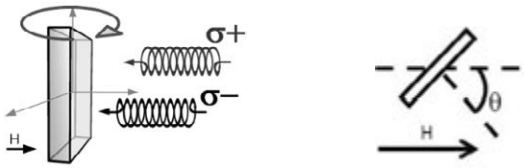

Fig. 45: Schematic representation of the geometry used in XMCD experiment. The field is applied along the photon direction (left); θ is the angle between the magnetic field direction and the normal to the surface (right).

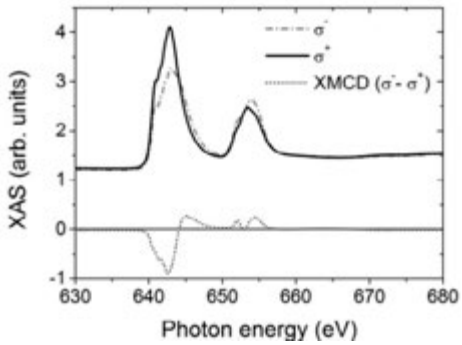

Fig. 46: XAS spectra acquired at the Mn $L_{2,3}$ edges in right circular polarisation σ^- (dash and dot) and left polarisation σ^+ (solid) and the XMCD spectrum σ^- - σ^+ (dot) of the $TbPc_2$/LSMO/STO hybrid surface. Reproduced from Ref. (Malavolti et al. 2013) with the permission from The Royal Society of Chemistry.

In fig. 46 are reported the XAS spectra acquired at 2 K and in presence of a 3 T field for both circular polarisations, i.e. σ^+ and σ^- corresponding to right and left polarisation, respectively, as well as the XMCD signal defined as $\sigma^- - \sigma^+$. The curves show the characteristic features expected for LSMO films reported by other authors (Li et al. 2011), confirming the quality of our surface, especially in respect of its magnetic polarisation.

The field dependence of the XMCD signal was recorded at the Mn $L_{2,3}$ at two angles, θ, between the magnetic field and the surface. Fig. 47 shows a more rapid saturation of the magnetic signal for θ = 45° in agreement with the expected angular dependence for the in-plane magnetic anisotropy of LSMO films.

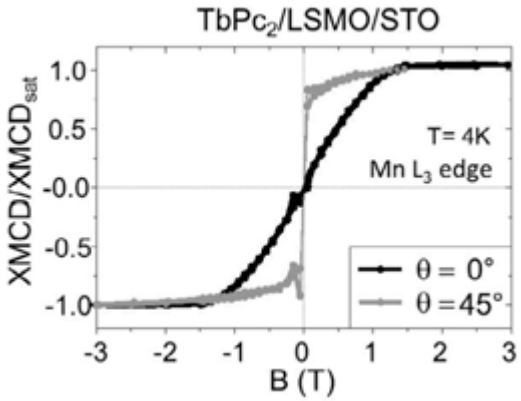

Fig. 47: Field and angular dependence of the XMCD signal acquired at the Mn L_3 edge. . Reproduced from Ref. (Malavolti et al. 2013) with the permission from The Royal Society of Chemistry.

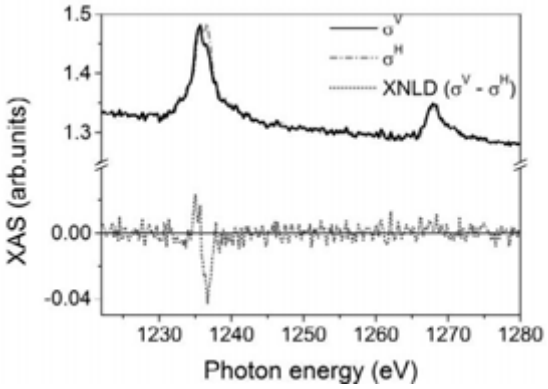

Fig. 48: XAS spectra acquired at the Tb $M_{4,5}$ edges in horizontal linearly polarisation σ^H (dash and dot) and vertical polarisation σ^V (solid) and the XNLD spectrum $\sigma^V - \sigma^H$ (dot) of the $TbPc_2$/LSMO/STO hybrid surface. . Reproduced from Ref. (Malavolti et al. 2013) with the permission from The Royal Society of Chemistry.

The sample was then characterised at the Tb $M_{4,5}$ edges in order to get structural and magnetic information on the molecular film. Since the roughness of the LSMO does not allow an STM investigation to get information about the molecular orientation on the surface, linearly polarisation light was employed (see section 2 paragraph 5.4). The XAS spectra using vertically (σ^V) and horizontally (σ^H) polarised light were recorded at θ = 45° thus allowing to extract the X-ray Natural Linear Dichroism (XNLD) spectrum, defined as $\sigma^V - \sigma^H$, which is reported in fig. 48. The presence of dichroism at the M_5 edge suggests a non random orientation of the electric field generated by the ligands around the Tb^{3+} ion and thus a partial preferred orientation of the molecules on the surface can be suggested. By comparison with previous calculated data reported in literature (Margheriti et al. 2010) the shape of the XNLD spectrum can be interpreted considering a favoured standing-up geometry of the $TbPc_2$ molecules respect to the surface plane. This finding is in line with the observed growing mode of simple metal-phatahlocyanines on oxides (Biswas et al. 2009). Nevertheless the roughness itself could play a non-negligible role.

The magnetic characterisation was carried out employing the circular polarised light. The XAS and XMCD spectra are reported in fig. 49. The XMCD spectrum shows a strong dichroism at the M_5 edge whereas a smaller one at the M_4 edge as expected for the $TbPc_2$ molecules (Margheriti et al. 2010).

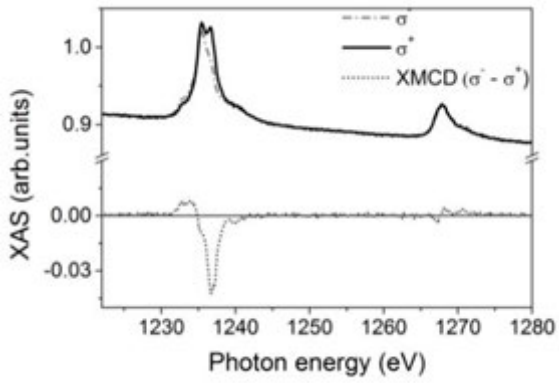

Fig. 49: XAS spectra acquired at the Tb $M_{4,5}$ edges in right circular polarisation σ^- (dash and dot) and left polarisation σ^+ (solid) and the XMCD spectrum $\sigma^- - \sigma^+$ (dot) of the $TbPc_2$/LSMO/STO hybrid surface. . Reproduced from Ref. (Malavolti et al. 2013) with the permission from The Royal Society of Chemistry.

The hysteresis loops recoded at Tb $M_{4,5}$ edges are reported in fig. 50. Albeit the hysteresis curves show the butterfly shape, typical of bulk $TbPc_2$ molecules, the opening is significantly smaller. A slight angular dependence confirms what evidenced by the XNLD spectrum, i.e. a slightly preferential orientation of the mole-

cules with their easy magnetisation axis in the plane of the surface. It's interesting to note that no sizable antiferromagnetic coupling of the molecules with the LSMO was detected and no correlation of the molecular hysteresis loops with those of the substrate was observed. The roughness of the substrate and the standing preferential orientation of $TbPc_2$ molecules are not favourable conditions to promote a significant molecule-substrate magnetic interaction and the use of magnetic metallic surface appears more promising and has been the object of this thesis, as described in the next session.

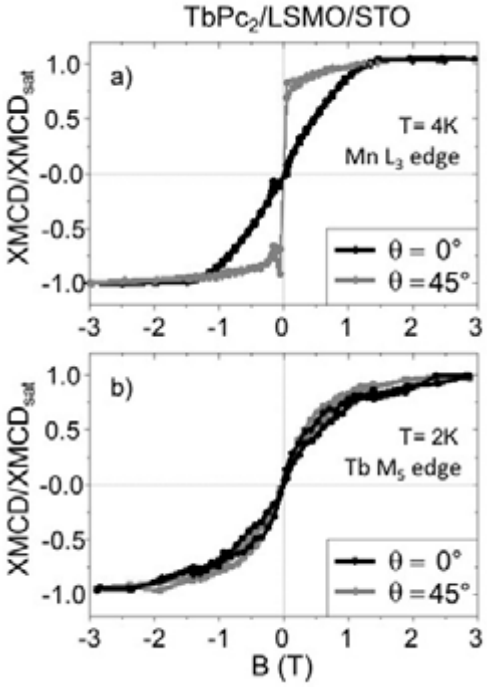

Fig. 50: Field and angular dependence of: the XMCD signal acquired at the Mn L_3 edge (top), and of the XMCD signal acquired at the Tb M_5 edge for the $TbPc_2$/LSMO/STO hybrid surface. Reproduced from Ref. (Malavolti et al. 2013) with the permission from The Royal Society of Chemistry.

4.3 $TbPc_2$/Co/Cu(100) hybrid surface

The study of the hybrid surface made by phthalocyanine molecules sublimated on magnetic metals is attracting an increasing interest. Although in some cases the magnetic moment of MPc molecules is quenched by the interaction with a metallic surface (Mugarza et al. 2012; Stepanow et al. 2011), the interaction of flat metal complexes with ferromagnetic substrate has been widely studied showing interesting proprieties. By investigating the hybrid surface made by iron porphyrin molecule

sublimate on Co and Ni surfaces Wende et al. (Wende et al. 2007) detected the presence of a ferromagnetic exchange coupling. Similar studies are reported also for MPc hybrid surfaces which demonstrated that the coupling can be strong enough to polarise the molecular magnetic moment at room temperature (Scheybal et al. 2005; Miguel et al. 2011; Wende et al. 2007). These findings have boosted the characterisation of hybrid surface made by $TbPc_2$ SMM on such magnetic substrates.

A recent study has shown the presence of a strong antiferromagnetic (AF) interaction between the $TbPc_2$ molecules and a nickel substrate film grown on Cu(001) (Lodi Rizzini et al. 2011). Given the relevance of metallic cobalt substrate in the realization of organic spintronic devices (Dediu et al. 2009) the extension of the investigation to this metallic surface appeared necessary. Only after we performed our experiments a brief report on the characterisation of the $TbPc_2$/Co/Cu(100) system became available in literature (Klar et al. 2013), showing a weak AF coupling between $TbPc_2$ and cobalt. We will show in the following that different results have been obtained by us.

In contrast to the case of LSMO the cobalt substrate need to be prepared *in situ* at the synchrotron facility and its realization poses some criticalities. Therefore in house preliminary cobalt evaporation tests to obtain an epitaxial growth of Co on a Cu(100) single crystal were carried out in our UHV multi-instrument system presented in section 2 paragraph 9.

In order to evaluate the optimal conditions for the cobalt epitaxial growth several techniques were employed. The thickness of the films was estimated by cross-checking STM and XPS data. The XPS regions of Co *2p* and Cu *2p* peaks and their relative fits of a 42 min evaporated Co film are reported in fig. 51a,b.

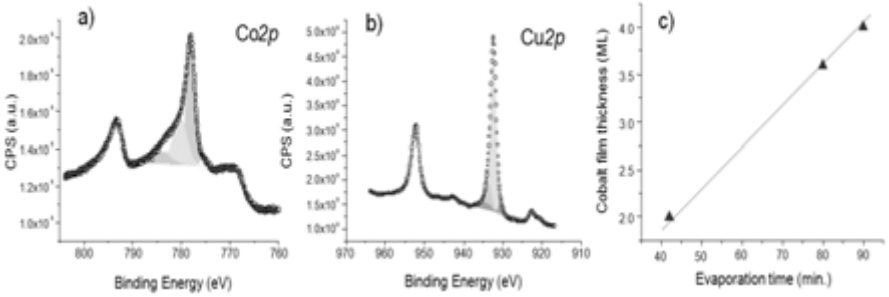

Fig. 51: XPS spectra and relative fit of the Co2p region (a) Cu2p region (b) and the calibration point of the evaporation process (c). Reproduced from Ref. (Malavolti et al. 2013) with the permission from The Royal Society of Chemistry.

The spectra were acquired using the monochromatic Al K_α source, 1486.6 eV. Following the considerations reported in section 2 paragraph 4.1 the cobalt layer thickness d was calculated as:

$$d = \lambda cos\theta \ln\left(\frac{I'_A \sigma_B}{I'_B \sigma_A} + 1\right) \quad (45)$$

where λ is the escape length of the photoelectrons, I'_A , I'_B are the areas and σ_A, σ_B are the cross-section of the Cu $2p_{3/2}$ and Co $2p_{3/2}$ peaks, respectively. The calculated thickness of the 42 min evaporated cobalt film was 2.1 ML. Same investigations were repeated increasing the evaporation time obtaining the calibration curves reported in fig. 51c. The data could be fitted by a linear relation, as expected for constant Co evaporation flux.

Before the XPS investigation the 2.1 ML cobalt film sample was also characterised by STM. In fig. 52 are reported the STM images for two different nominal thicknesses, 2.1 and 4 ML of Co, as estimated from the previous calibration. Both samples show a *quasi* layer-by-layer growth (Allmers & Donath 2011) with the formation of small cobalt islands. They present rounded edges preferentially oriented along the Cu [±110] directions; moreover the cobalt films do not exactly reproduce the underling Cu atomic step edges looking meandering (Ramsperger et al. 1996). All these features confirm the good quality of the cobalt films.

It is well known that in thin films an intermixing of the two metals can take place even at room temperature due to an atomic exchange process [26,28]. This phenomenon could be responsible of the formation of a layer of copper on top of the cobalt film.

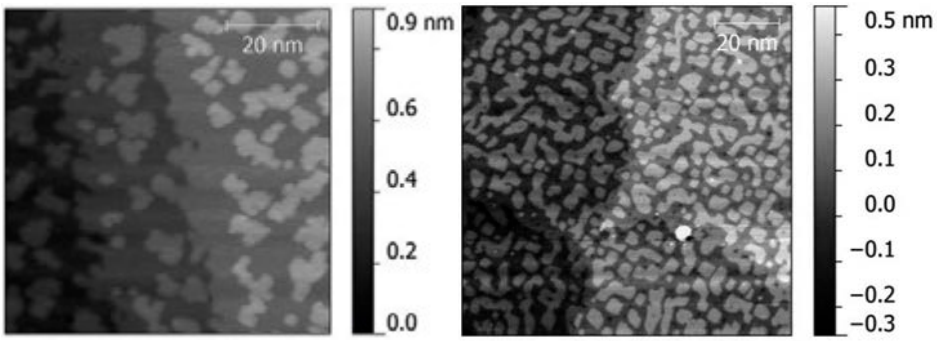

Fig. 52: STM image of 2.1ML (400 pA; -0.4 V ; 75x75 nm^2) (a) and 4ML of Co on Cu(100) (900 pA; 1.4 V; 100x100 nm^2) (b). They show the typical cobalt rounded edge islands preferentially oriented along the Cu [±110] directions.

In order to take in account this phenomenon the LEIS techniques, sensitive to the top-most layer chemical composition, was employed (see section 2 paragraph 7). The LEIS spectra, presented in fig. 53, were acquired using a He^+ beam accelerated to 1000 eV on samples with increasing thickness of the Co film. The data are relative to

the same samples of the XPS characterisation. The Cu peak is found at about 790 eV whereas the Co at ca. 770 eV, in agreement with atomic mass selectivity of the technique (see equation 26). As expected increasing the thickness deposition the intensity of the Cu peak decreases while the Co peak increases. The 4 ML sample shows almost uniquely the Co peak suggesting that for thicker samples the top-most layer is mainly made by Co.

The *in house* study was completed by STM investigation of the final hybrid surface. In order to have a clear image of the molecules sublimated on the cobalt surface a sub-monolayer coverage $TbPc_2$ film is mandatory. For this purpose we calibrated the $TbPc_2$ sublimation by STM investigation of molecular films sublimated on the Cu(100) single crystal. The image acquired on a sub-monolayer $TbPc_2$ film sublimated on Co/Cu(100) i.e. $TbPc_2$/Co/Cu(100) hybrid surface, is reported in fig. 54. It is important to point out that the molecules show the characteristic four lobed shape expected for lying down intact $TbPc_2$ complexes.

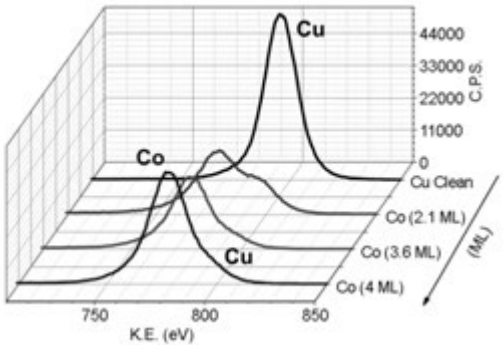

Fig. 53: LEIS spectra of clean Cu (100) surface and after subsequent Co deposition. Reproduced from Ref. (Malavolti et al. 2013) with the permission from The Royal Society of Chemistry.

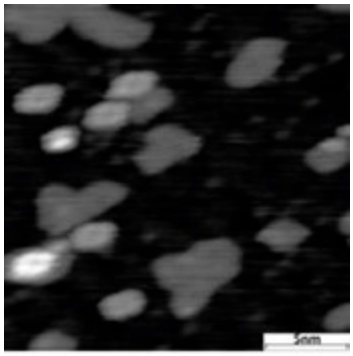

Fig. 54: STM image of $TbPc_2$/Co/Cu(100) (200 pA; 1.5 V; 22x22 nm^2). Reproduced from Ref. (Malavolti et al. 2013) with the permission from The Royal Society of Chemistry.

The magnetic characterisation of the hybrid surface was made by XAS and its derivate techniques. XMCD-based investigation requires specific UHV facilities allowing the *in-situ* preparation of the hybrid surface. The samples were growth in the preparation chamber of the DEIMOS beamline at the SOLEIL synchrotron (see section 2 paragraph 6). The cobalt evaporations were carried out using the same parameters of the *in house* experiments. Before preparing the final hybrid surface a characterisation of evaporated cobalt films was performed by using STM and XAS techniques. The nominal thicknesses presented hereafter were estimated from the Co $L_{2,3}$ edges jump ratio. The quality of the surfaces was checked by *in situ* STM analysis. The image acquired for a nominal 2.5 ML cobalt film is reported in fig. 55. The image shows the expected features described in the previous paragraph. Indeed the cobalt islands are aligned along two preferential directions and the edge steps look meandering (similar to what reported in fig. 52), as expected for the cobalt epitaxial growth on copper (Allmers & Donath 2011; Ramsperger et al. 1996).

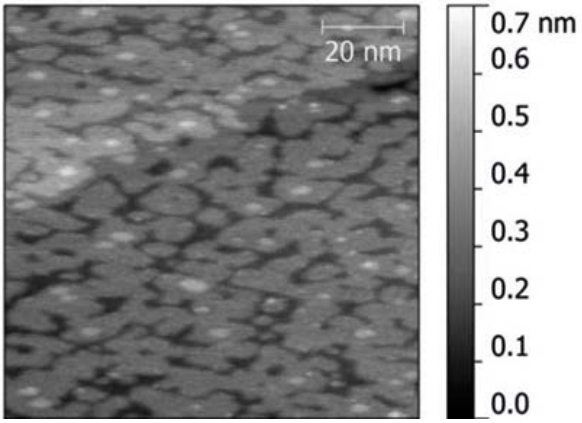

Fig. 55: *In situ* STM image of a 2.5 ML of Cobalt evaporated on Cu(100) (100 pA ; 1.0 V; 95x95 nm^2).

It is well known that the magnetic anisotropy of Co films depends strongly on the thickness. We decided to investigate a thickness of 5 ML which corresponds to a strong in plane magnetisation. The XAS spectra and the relative XMCD of a 5.5 ML cobalt film are reported in fig. 56. It is important to note that the shape and energy of the cobalt $L_{2,3}$ rule out the presence of oxidised cobalt (Chen et al. 1995; Srivastava et al. 1998). This is of the utmost importance in order to study the magnetic behaviour of the hybrid surface. In order to evaluate the magnetic behaviour of the cobalt film the XMCD sum rules can be applied (Chen et al. 1995; Srivastava et al. 1998).

Through their application it is possible to estimate both orbital (m_{orb}) and spin (m_{spin}) moments using the integral calculation described by Chen et al. (Chen et al. 1995) (see section 2 paragraph 5.3). From this analysis we estimated m_{orb} = 0.23 μ_B, m_{spin} = 1.81 μ_B and the resulting ratio m_{orb}/m_{spin}= 0.127. These data are in agreement with what reported in literature (Srivastava et al. 1998) and will be useful for further considerations.

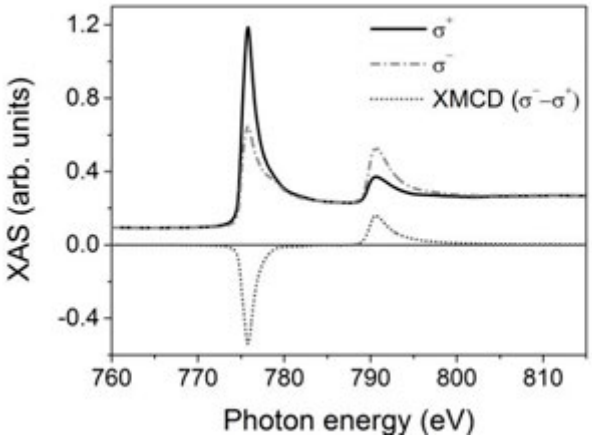

Fig. 56: XAS spectra acquired at the Co $L_{2,3}$ edges (5.5 ML) in right circular polarisation σ^- (dash and dot) and left polarisation σ^+ (solid) and the XMCD spectrum σ^- - σ^+ (dot) of the Co/Cu(100) surface. Reproduced from Ref. (Malavolti et al. 2013) with the permission from The Royal Society of Chemistry.

In order to prepare the hybrid surface the sublimation of thin $TbPc_2$ film was carried out on a freshly prepared 5 ML cobalt film. We employed the elemental selectivity of the XAS based techniques to characterise the cobalt film magnetic behaviour of the $TbPc_2$/Co/Cu(100) hybrid surface. The XAS spectra acquired at the Co $L_{2,3}$ edges using both circular polarisations and the relative XMCD spectrum are reported in fig. 57. The sum rules were applied allowing the calculation of the m_{orb} = 0.22 μ_B, m_{spin} = 1.75 μ_B and the resulting ratio m_{orb}/m_{spin}= 0.125. These data are in agreement with those presented for the bare 5.5 ML cobalt film. Thus no significant modification of the magnetic behaviour of the cobalt film is showed due to the presence of the molecular film.

The field dependence of the maximum of the XMCD signal at the Co L_3 edge acquired for θ =0° and θ=60° are reported in fig. 58. The curves show the pronounced angular dependence expected for a cobalt thin film with in plane magnetic anisotropy. The out of plane magnetic signal saturates at ~3.7 T This anisotropy field is in agreement to the expected one for 5 ML cobalt film thickness (Kowalewski

et al. 1993) confirming the high quality and good control we have achieved in the preparation of the Co substrate.

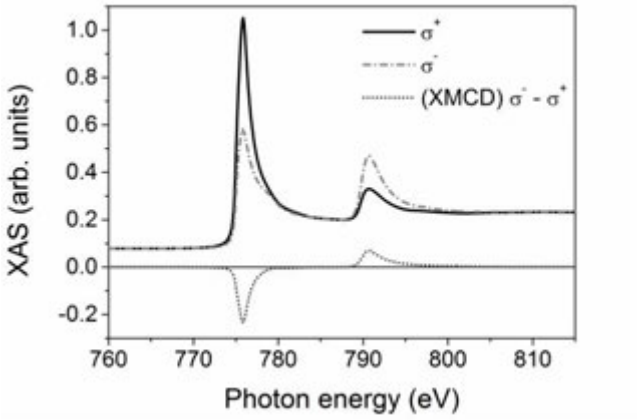

Fig. 57: XAS spectra acquired at the Co $L_{2,3}$ edges (5 ML) in right circular polarisation σ^- (dash and dot) and left polarisation σ^+ (solid) and the XMCD spectrum σ^- - σ^+ (dot) of the $TbPc_2$/Co/Cu(100) hybrid surface. Reproduced from Ref. (Malavolti et al. 2013) with the permission from The Royal Society of Chemistry.

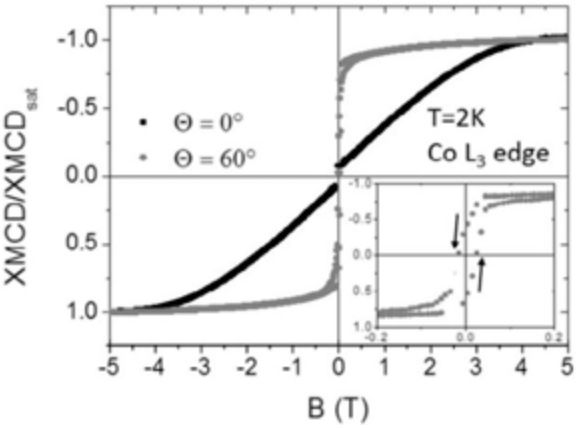

Fig. 58: Field and angular dependence of the XMCD signal acquired at the Co L_3 edge. In the inset is reported the enlargement of the θ=60° curve which show the hysteretic behaviour of the cobalt film. Reproduced from Ref. (Malavolti et al. 2013) with the permission from The Royal Society of Chemistry.

Moving to the Tb $M_{4,5}$ edges, the XAS recorded spectra (fig. 59) acquired with linear polarised light show the presence of a sub-monolayer $TbPc_2$ film. A semi-quantitative estimation of the thickness can be done by comparing the Tb M_5 edge

signal with the oscillation of the background that is due to the EXAFS signal of the copper substrate. Comparing our results with literature data (Lodi Rizzini et al. 2011; Klar et al. 2013) it is possible to assert that the $TbPc_2$ coverage is in the sub-monolayer range.

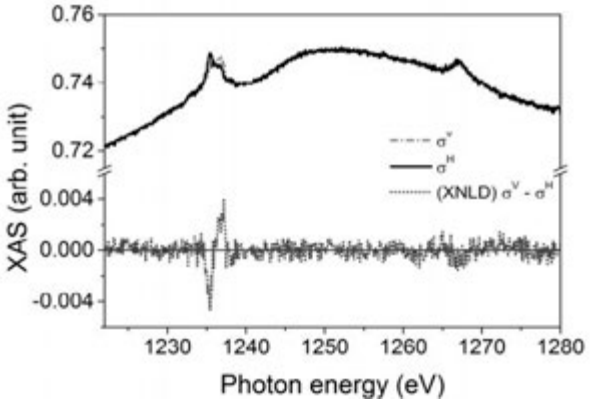

Fig. 59: XAS spectra acquired at the Tb $M_{4,5}$ edges in horizontal linearly polarisation σ^H (solid) and vertical polarisation σ^V (dash and dot) and the XNLD spectrum σ^V - σ^H (dot) of the $TbPc_2$/Co/Cu(100) hybrid surface. Reproduced from Ref. (Malavolti et al. 2013) with the permission from The Royal Society of Chemistry.

The XNLD reveals a dichroic signal at the M_5 edge, whose shape is similar to that previously observed for the film grown on LSMO, but with opposite sign. This can be ascribed to the lying down orientation of $TbPc_2$ molecules, expected for metallic surfaces and indeed observed in our STM investigation (fig. 54).

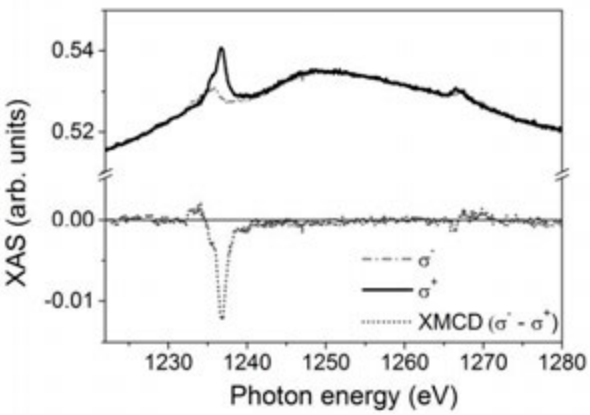

Fig. 60: XAS spectra acquired at the Tb $M_{4,5}$ edges in right circular polarisation σ^- (dash and dot) and left polarisation σ^+ (solid) and the XMCD spectrum σ^- - σ^+ (dot) of the $TbPc_2$/Co/Cu(100) hybrid surface. Reproduced from Ref. (Malavolti et al. 2013) with the permission from The Royal Society of Chemistry.

The XMCD spectrum, reported in fig. 60, shows similar features to those observed also for bulk samples and films on other substrates, including the LSMO (see section 3 paragraph 4.2). The field and angular dependence of the dichroic signal at the M_5 edge are reported in fig. 61. In agreement with previous observation, the magnetic signal saturates at smaller fields when the field is applied out of plane, $\theta=0°$, as this corresponds to the easy axis of lying down molecules. In both loops, recorded at different angles, no detectable opening of the hysteresis is revealed. The $TbPc_2$ seems to behave as a simple paramagnetic molecule at a temperature as low as 2K, in agreement with previous findings on thin films of $TbPc_2$ evaporated on non-magnetic substrates, such as gold (Margheriti et al. 2010) and copper (Stepanow et al. 2010).

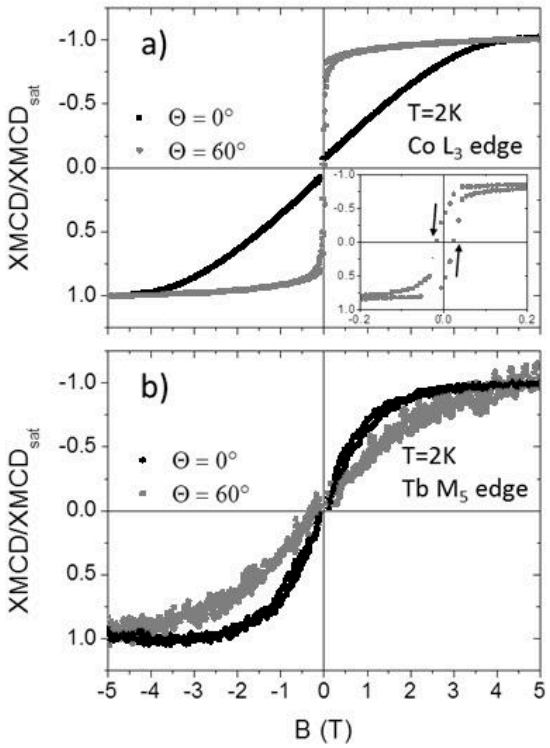

Fig. 61: Field and angular dependence of: the XMCD signal acquired at the Co L_3 edge (top), and of the XMCD signal acquired at the Tb M_5 edge for the $TbPc_2$/LSMO/STO hybrid surface. Reproduced from Ref. (Malavolti et al. 2013) with the permission from The Royal Society of Chemistry.

More interesting is the absence of any detectable antiferromagnetic interaction between the molecular sub-monolayer film and the cobalt substrate. In fact the

magnetic signal does not show any anomaly in the field dependence, typical of the overcoming of an antiferromagnetic interaction. It must also be noted that no correlation is observed between the magnetism of the two materials, which present different magnetic anisotropy, and no anomalies in $TbPc_2$ behaviour are observed at the saturation fields of the Co substrate. Our results are in contrast to what recently reported by other authors (Klar et al. 2013) in a short communication for the same hybrid surface. The origin of this discrepancy remains unclear, given also the limited information available in the reported communication. In detailed analysis we performed on both Co substrate and molecular film we can exclude the incidence of the most common issues that may have a negative impact on the measure: like the formation of an oxide layer, the termination with nonmagnetic Cu film, or the evaporation of a thick molecular film, preventing a direct contact between the magnetic molecules and the magnetic substrate.

Section 4
The Fe_4 SMM class

1 Introduction

The slow magnetic relaxation properties of the family of Fe_4 molecules, conjugated with their chemical stability, made them one of the most interesting SMMs. Despite the low blocking temperature (hysteresis opening only below 1 K) Fe_4 molecules have been used as model systems to shed some light on the complex and fascinating behaviour of SMMs (Gatteschi et al. 2006). Fe_4 SMMs have the propeller like shape shown in fig. 62. In the archetypal Fe_4 system the three peripheral iron(III) ions are coordinated by two diketonate ligands, i.e. dipivaloylmethanate (dpm^-), while six μ-methoxide (OMe^-) anions bridge them to the central iron(III) ion to give the final formula $[Fe_4(OMe)_6(dpm)_6]$ (Barra et al. 1999). The molecule is characterised by the presence of a C_2 symmetry axis passing through Fe1 and Fe2, thus the peripheral ions are arranged at the vertices of an isosceles triangle (Barra et al. 1999). The antiferromagnetic coupling of the central ion (s=5/2) to the peripheral ones (s=3x5/2) causes the total spin of the ground state to be S=5. The ground state can be considered selectively populated for temperature below 5 K.

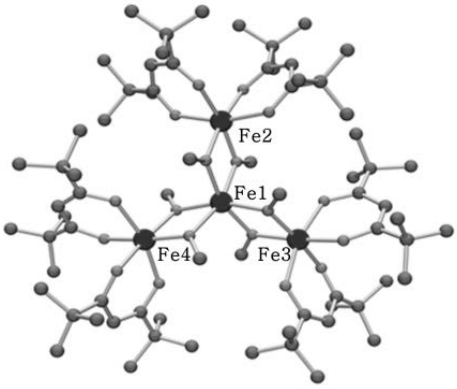

Fig. 62: Molecular structure of the archetypal Fe_4 system, the $[Fe_4(OMe)_6(dpm)_6]$.

Luigi Malavolti, *Single molecule magnets sublimated on conducting and magnetic substrates*,
ISBN 978-88-6655-969-6 (print) ISBN 978-88-6655-970-2 (online)

The degeneracy of the S=5 ground state is removed by the zero-field splitting Hamiltonian term:

$$H_{zfd} = D\left[\hat{S}_z^2 - \tfrac{1}{3}S(S+1)\right] \qquad (46)$$

where D, the axial anisotropy factor, is equal to -0.2 cm^{-1} for the $[Fe_4(OMe)_6(dpm)_6]$ and $\hat{S}_z$ is the projection of the total spin operator along the easy axis. Therefore the energy level as function of m_s, eigenvalues of $\hat{S}_z$ is a parabola (fig. 63).

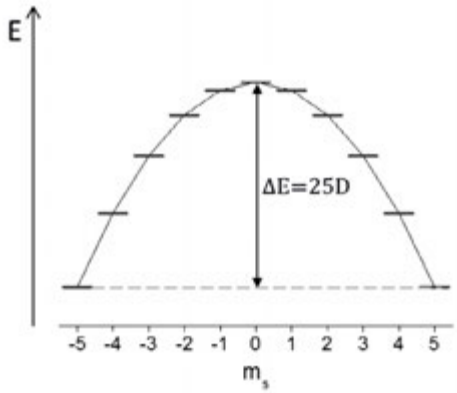

Fig. 63: Energy level diagram of the S=5 state as function of the m_s states in zero field; $\Delta E = DS^2$ is the energy of the anisotropy barrier.

The magnetic properties of the molecule, i.e. the D parameter, can be easily tuned by replacing the six μ-metoxide bridges with two tripodal ligands, leading to the general formula $Fe_4(L)_2(dpm)_6$ (Andrea Cornia et al. 2004; A Cornia et al. 2004). The introduction of the tripodal ligands L=R-C$(CH_2OH)_3$ where R=Me, R=CH_2Br, R=Ph modifies the helical pitch of the $Fe(O_2Fe)_3$ unit toward three-fold symmetry. This also increases the axial anisotropy resulting in D values equal to -0.445 cm^{-1}, -0.432 cm^{-1}, -0.42 cm^{-1}, respectively (Accorsi et al. 2006). The same trend is found also for the anisotropy barrier.

As in the case of the terbium(III) bis(phthalocyaninato) complex, the potential for the use of Fe_4 in spintronic devices, being one of the most stable and versatile SMM, boosted the development of its assembling strategies on surfaces (Bogani & Wernsdorfer 2008). The addition of sulphur-containing moieties on the R group of the tripodal ligands allowed the preparation of chemically grafted monolayers on gold surfaces. XMCD based experiments evidenced that the typical butterfly-shaped magnetic hysteresis of these SMMs was still observable in monolayers assembled on gold (Mannini et al. 2009; Mannini et al. 2010; Rodriguez-Douton et al. 2011). On

the other hand the deposition from solution is still far from allowing a detailed characterisation of the film and a fine control of the molecular organization on surfaces. Indeed, the UHV thermal deposition, employed in this thesis for $TbPc_2$ SMMs, is highly desirable not only for the cleanness of the process but also for the possibility to control the coverage allowing also the investigation of individual molecules.

In order to exploit the UHV techniques physical deposition method based on the sublimation process is desirable. UHV sublimation allows a larger versatility in the selection of surfaces that can be used as well as a larger control of the deposition characteristics.

A considerable effort has been made to obtain SMMs that retain their properties after the thermal sublimation onto a surface. Among the several Fe_4, the complex bearing the tripodal ligand L=Ph-$C(CH_2OH)_3$ (hereafter Fe_4Ph, see fig. 64), has been proved to sublimate in UHV and to maintain its SMM character when deposited to form films a few hundreds nm thick. Although the SMM behaviour is preserved, both susceptibility and EPR measurements have shown the presence of some impurities (less than 5%) which can be associated with the very volatile $Fe(dpm)_3$ compound (Margheriti et al. 2009).

Starting from these findings one of the goals of this thesis has been the investigation of Fe_4Ph at the single molecule level. STM and STS local probe techniques have been employed to characterise hybrid surfaces, i.e. Fe_4Ph molecules sublimated on different surfaces. For this purpose XPS and UPS techniques were also employed to get important information about the chemical composition and electronic properties of the molecular film. By means of a spectroscopic and STM characterisation we studied different kinds of hybrid surfaces (Fe_4Ph on Au(111), Cu(100) and Cu_2N) succeeding in finding the suitable conditions to isolate the molecules on the surface and perform STS measurements.

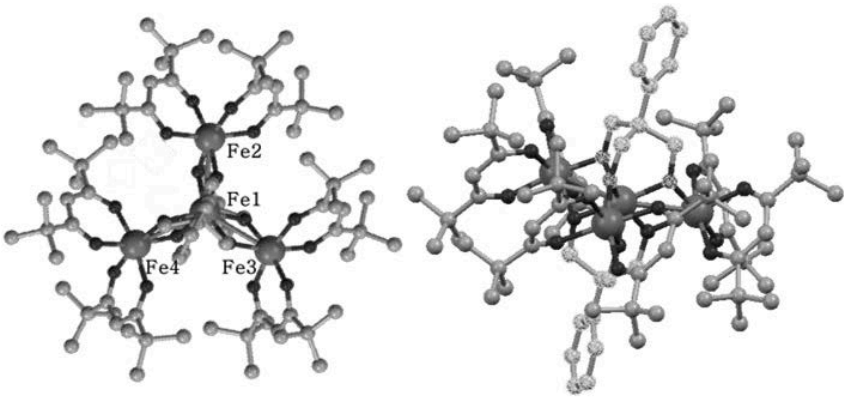

Fig. 64: Fe_4Ph structure; top view (left); side view (right).

2 Thick film characterisation

As a first step we looked for the optimal conditions for the UHV thermal deposition of Fe_4Ph. The molecule was synthetized by the group of prof. A. Cornia at the University of Modena and Reggio Emilia (UNIMORE) following the procedure already reported by our joined teams (Accorsi et al. 2006). Fe_4Ph crystals were mechanically ground before being inserted into the sublimation crucible. In order to define the parameters of the sublimation process a Quartz Crystal Microbalance (QCM) was employed. For the microbalance calibration the crystal density of the Fe_4Ph, $\rho = 1.192\ g{\cdot}cm^{-3}$ (Accorsi et al. 2006), was used to evaluate the nominal thickness (see equation 13). The thickness values as a function of the time, while the crucible temperature is slowly increased, is reported in fig. 65. The sublimation rate becomes different from zero above 200 °C, as evidenced by the corresponding increase of the film thickness. These data are partially in contrast with previous experiments (Margheriti et al. 2009; Margheriti 2010) where the sublimation rate is reported to start at higher temperature; however the different experimental setup, in particular the thermocouple positioning, can account for this discrepancy.

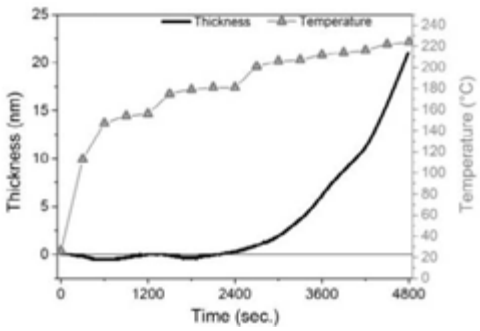

Fig. 65: Quartz microbalance thickness data (black) and the corresponding temperature (gray) as a function of the elapsed time.

On the basis of QCM data, degassing of the powder has been carried out immediately below the sublimation temperature, i.e. 200°C maintaining this temperature for 48 hours before using it for the sample preparation. Then, every deposition was made by using a crucible temperature of 215°C, which allowed to have a very low nominal deposition rate (0.5 Å/min). All Fe_4Ph films were prepared by keeping the substrate at room temperature. The sublimation process was then validated on the basis of the spectroscopic features (XPS and UPS) of a thick film (ca 4 nm) grown on the Au(111) surface.

The XPS spectra were acquired using a monochromatic Al K_α source (1486.6eV). The XPS spectra in the regions of interest (Fe *2p*, O *1s*, C *1s* and Au *4f*) and relative

curve fitting are reported in fig. 66. The binding energy scale was calibrated by setting the Au $4f_{7/2}$ peak to 84.04 eV. The Fe *2p* region shows a typical structured signal due to the presence of satellite peaks. This region of the spectrum was fitted by using three components for each spin orbit peak, as reported in literature (Yamashita & Hayes 2008; Rigamonti et al. 2013). It is important to note that the binding energy of the first component of the Fe $2p_{3/2}$ peak is at 711.1 eV, in agreement with the expected value for Fe^{3+} ions. Two components were used for the O *1s* region, in order to account for the shake-up peak. In the C *1s* region two contributions can be distinguished: a main component due to aliphatic and aromatic carbon atoms (285.0 eV) and a shoulder due to the carbonyl and alcoholic carbon atoms (286.5 eV). The relative intensity of the two contributions matched the expected value of 3.8.

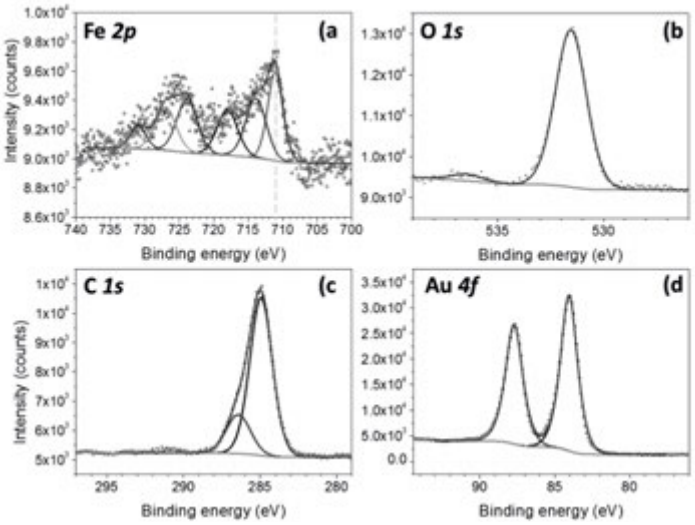

Fig. 66: XPS data for the Fe_4Ph thick film (ca. 4 nm): Fe *2p* (a), O *1s* (b), C *1S* (c), and Au *4f* region (d) and their relative fits. The spectra were acquired using a monochromatic Al K_α source (1486.6eV).

In order to estimate abundance of each element percent the following formula were employed:

$$Fe\% = \frac{A_{Fe}/\sigma_{Fe}}{A_{Fe}/\sigma_{Fe}+A_C/\sigma_C+A_O/\sigma_O} \qquad (47)$$

$$C\% = \frac{A_C/\sigma_C}{A_{Fe}/\sigma_{Fe}+A_C/\sigma_C+A_O/\sigma_O} \qquad (48)$$

$$O\% = \frac{A_O/\sigma_O}{A_{Fe}/\sigma_{Fe}+A_C/\sigma_C+A_O/\sigma_O} \qquad (49)$$

Where ΔE, A_O and A_C are the areas of Fe, O and C respectively and σ_{Fe}, σ_O, σ_C their relative cross-section at 1486.6 eV. The good agreement of the experimental data with the theoretical ones, suggests the presence of intact molecules on the surface (table 3).

	Experimental	Expected
Fe%	3.6	3.7
O%	16.8	16.7
C%	79.6	79.6

Table 3: Comparison between the expected elemental composition for Fe_4Ph and that obtained by XPS analysis for a thick film of Fe_4Ph (ca 4nm) grown on the Au(111) surface.

The spectroscopic characterisation of the film was completed by performing UPS experiments. By means of the He(II) source (40.8 eV), see section 2 paragraph 4.2, it was possible to probe the occupied molecular states up to 20 eV below the Fermi level and thus to obtain a spectroscopic fingerprint of the molecule (fig. 67). The binding energy value ~2.6 eV of the highest molecular orbital (peaks 1,2) indicates the insulating character of the molecule which is an important aspect to take into account when correlating UPS with STM and STS measurements. The experimental spectrum (upper curve) is in very good agreement with the theoretical DOS (lover curve) calculated for the isolated molecule (see fig. 67).

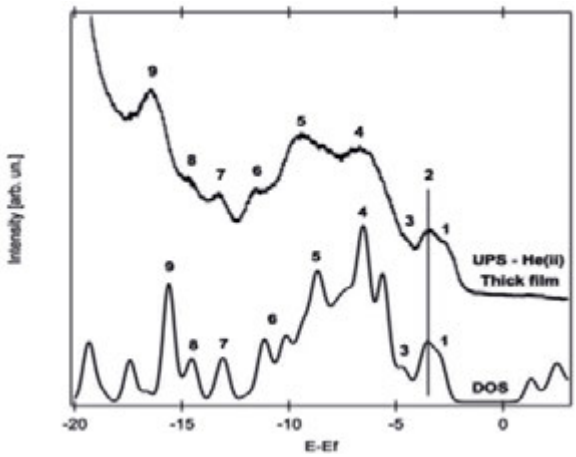

Fig. 67: Comparison between the theoretical DOS calculated for the isolated Fe_4Ph molecule and the UPS spectrum taken for a 4 nm Fe_4Ph film deposited on Au(111).

All calculations were performed by S. Ninova with the CP2K program package (Mundy et al. n.d.) within the DFT framework and we provide here an

overview of the calculations. Grimme's D3 parameterization approach was used in order to introduce the dispersion correction term (Grimme et al. 2010). The revPBE (Zhang & Yang 1998) functional was chosen for the geometry optimization. The Norm-conserving Goedecker-Teter-Hutter (GTH) pseudopotentials were used together with GTH double-ζ polarized molecularly optimized basis sets for all atomic species (Goedecker et al. 1996). An energy cut-off of 400 Ry was applied to the plane-wave basis sets. The Fe_4Ph cluster was considered in its ground state (S=5), where the central ion is antiferromagnetically coupled with the peripheral ones. The size of the simulation cell was (25 x 25 x 25) Å. The structure of the Fe_4Ph was taken from X-ray experimental data and it was geometrically optimized. For the density of states, the optimized structure was set to wavefunction optimization, using the hybrid functional PBE0 (Ernzerhof & Scuseria 1999) and a 0.35 Gaussian convolution has been introduced in order to better compare with the experimental dataset. The theoretical spectrum has been shifted of about 2.8 eV in order to align the experimental and theoretical HOMO, the highest occupied molecular orbital.

Both XPS and UPS investigations suggest the presence of intact molecules in the thermally deposited thick film. We then focused our attention on the preparation and characterisation of monolayer and sub-monolayer films, deposited on the Au(111) surface.

3 Preparation and XPS characterisation of Fe_4Ph deposited on Au(111) at low-coverage

In order to obtain the suitable coverage to study the molecule in isolated conditions (sub-monolayer deposition) we calibrated the evaporation times by referring to the XPS Fe *2p* signal of chemical grafted monolayer of Fe_4C_9 on gold (Mannini et al. 2010). The Fe_4C_9 belongs to the family of $Fe_4L_2dpm_6$ in which the tripodal ligands bear a sulphur moiety able to graft the molecule on the gold substrate. In this case C_9 stands for 11-(acetylthio)-2,2-bis(hydroxymethyl)undecan-1-ol. The gold substrate (100 nm Au/Mica) was left incubating for 24 hr in a solution of 2 mM Fe_4C_9 in CH_2Cl_2. After that the surface was washed several times with CH_2Cl_2 to remove the physisorbed material.

The Fe*2p* and Au*4f* regions of the Fe_4C_9 sample are reported in fig. 68. As in the case of the thick film the binding energy of the Fe $2p_{3/2}$ peak is in agreement with the presence of Fe^{3+}. The $(A_{Au}/\sigma_{Au})/(A_{Fe}/\sigma_{Fe})$ i.e. the ratio between the Au *4f* area (A_{Au}), corrected by its cross-section (σ_{Au}), and the area of the Fe *2p* (A_{Fe}), again corrected by its relative cross-section (σ_{Fe}), was chosen as a reference for the monolayer coverage.

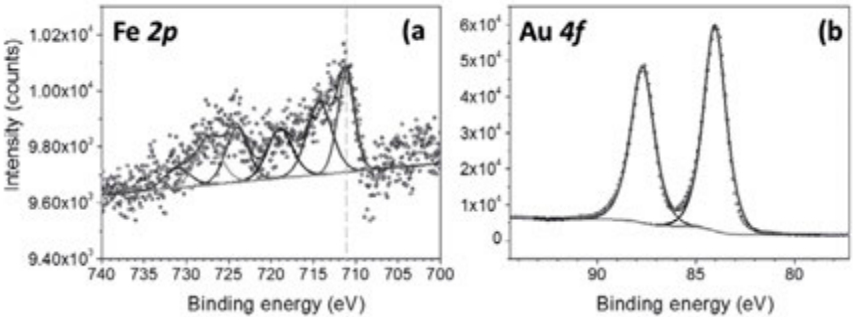

Fig. 68: XPS data for the chemical grafted Fe_4C_9 film: Fe *2p* (a), and Au *4f* region (b) and their relative fits. The spectra were acquired using a monochromatic Al K_α source (1486.6eV).

The exposure time of a clean Au(111) single crystal to the molecular flux was calibrated to achieve the same ratio as in the chemical grafted monolayer. A 0.85 nm film of sublimated Fe_4Ph, estimated from QCM data, matched the $(A_{Au}/\sigma_{Au})/(A_{Fe}/\sigma_{Fe})$ ratio of the Fe_4C_9 sample indicating the formation of almost monolayer coverage (table 4). The elemental percentage of this sample is in agreement, within the experimental error, with the expected values (table 4).

	$(A_{Au}/\sigma_{Au})/(A_{Fe}/\sigma_{Fe})$	Fe %	O %	C %
Chemical grafted (1ML)	34.6	–	–	–
Sublimated 0.85 nm (~1ML)	39.6	3.6	18.4	78.0
Sublimated 0.25 nm (<1ML)	141.1	3.1	18.1	78.8
Fe_4Ph expected values	–	3.7	16.7	79.6

Table 4: XPS data relative to the samples presented in this section.

It is important to note that the area quantification in monolayer/sub-monolayer samples is made difficult by the small S/N ratio which affects the Fe *2p* signal. Moreover, the O *1s* region background is perturbed by the onset of the Au *4p 3/2* peak (fig. 69b). In this case the choice for the background subtraction is very critical. Indeed by using different kind of baseline, we can obtain an overestimate of about 10% (Tougaard background) or an underestimate of 15% (Linear background). Here we reported the elemental percentage obtained with the Tougaard background.

The UPS technique is unfortunately not useful for very low coverage because the valence band of the Au substrate is still very intense and does not allow to disentangle the features of the molecule.

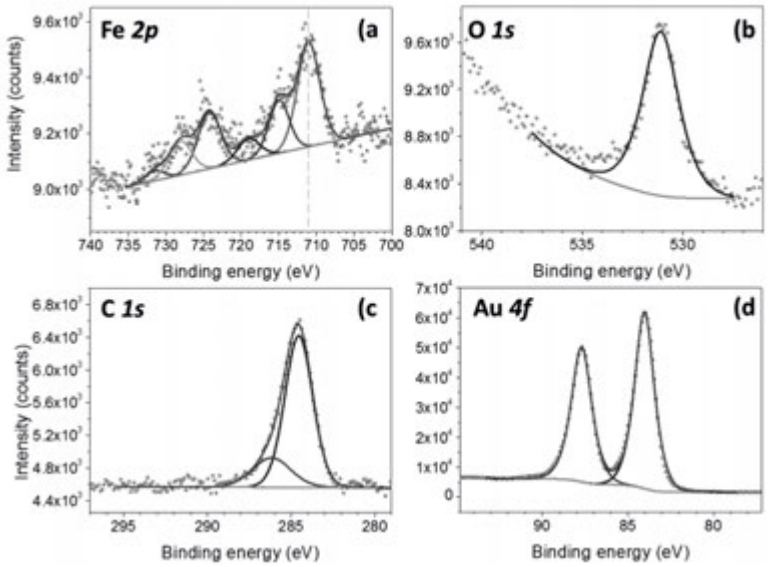

Fig. 69: XPS data for 0.85 nm (~1ML) film of Fe_4Ph: Fe *2p* (a), O *1s* (b), C *1S* (c), and Au *4f* region (d) and their relative fits. The spectra were acquired using a monochromatic Al K_α source (1486.6eV).

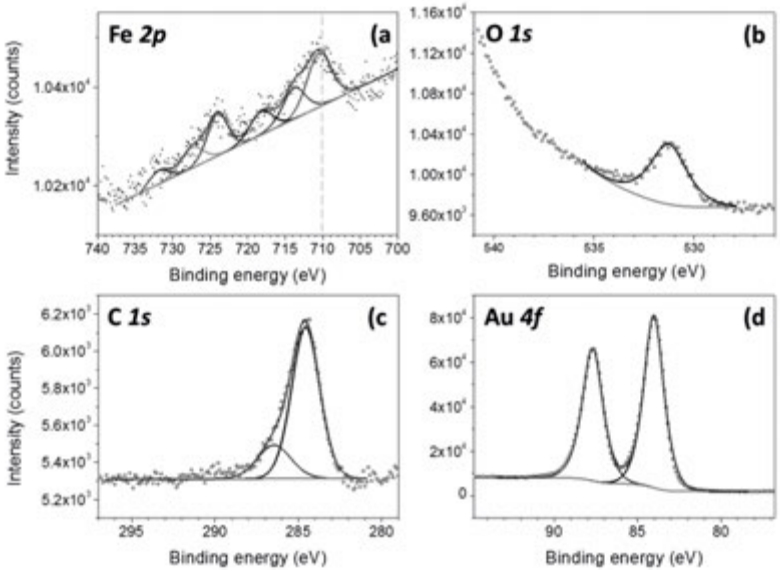

Fig. 70: XPS data of 0.25 nm sub-monolayer film: Fe *2p* (a), O *1s* (b), C *1S* (c), and Au *4f* region (d) and their relative fits. The spectra were acquired using a monochromatic Al K_α source (1486.6eV).

In order to achieve sub-monolayer coverage, which is the desired coverage for the STM investigation, a new sample was prepared with a nominal thickness of 0.25 nm. The XPS characterisation revealed a $(A_{Au}/\sigma_{Au})/(A_{Fe}/\sigma_{Fe})$ ratio significantly higher than in the previous samples, confirming the low coverage (table 4). The XPS spectra show a slightly shift of the Fe $2p_{3/2}$ binding energy, probably due to the screening effect of the substrate (fig. 70). The elemental percentage (table 4) is in agreement with the data of the 0.85 nm (~1 ML) film and, within the experimental error, with the expected values.

The characterisations performed above have permitted the tuning of the evaporation process as planned in order to reach a very low coverage of Fe_4Ph molecules. This low coverage allows to use STM for the local characterisation of the Fe_4Ph molecules on surface. Moreover, with the support of this STM investigation of low coverage deposition it has been possible to clarify the origin of the alteration in the elemental analysis carried out by the XPS.

4 STM characterisation of Fe_4Ph sub-monolayer on Au(111)

As mentioned in section 3 STM investigation of SMMs on surfaces have been mostly focused on the $TbPc_2$ molecule, which is an ideal candidate thanks to its flat shape. In fact other SMMs, such as Mn_{12} and Fe_4 classes of SMMs, are more three-dimensional in shape and less conductive, making STM investigation of these films more difficult.

For the STM investigation we used a Fe_4Ph film of about 0.25 nm estimated thickness (sub-monolayer range) sublimated on a Au(111) single crystal. After the evaporation, the sample was immediately cooled down to 35 K. The sample cooling is needed in order to prevent the molecular diffusion on the surface that would probably favour the formation of densely packed domains making difficult to get a good imaging of the molecules. It is important to stress that all the images presented here were acquired using low tunnelling current, i.e. 3 pA. Higher current values, indeed, seem to be very dangerous for the molecules which can be damaged by the tip.

A large scale STM image of 0.25 nm Fe_4Ph/Au(111) is reported in fig. 71a. The image shows clearly the presence of two different kinds of molecular domains (labelled as A and B). A close inspection of B-type domains reveals the presence of spherical objects (fig. 71b). On the other hand the objects forming the A-type domains seem to be very flat with a characteristic bi-lobed shape (fig. 71c). By looking at the profile traced in fig. 71b and reported in fig. 71d we can appreciate the different height of the two domains: 0.25±0.04 nm and 0.7±0.1 nm for A and B, respec-

tively. It is important to note that the height of both domains is referred to the bare gold, i.e. the A and B objects are in direct contact with the surface.

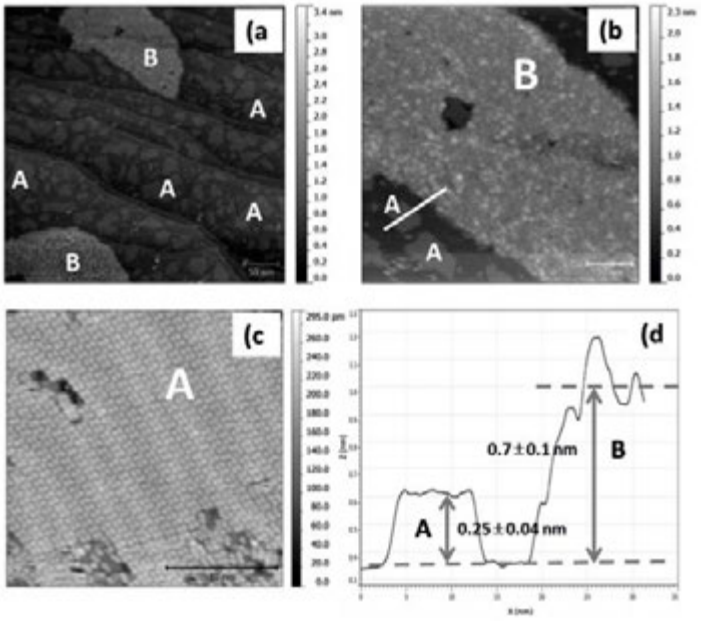

Fig. 71: STM investigation of 0.25 nm sub-monolayer film. Large scale image of the surface (3pA; 2.5V; 400x400nm^2) (a); enlargement of the B structure (3pA; 2.5V; 120x120nm^2) (b); high resolution image of the A structure (3pA; 2.5V;25x25nm^2) (c); and the profile of the b image (d).

Although the height estimated from STM experiments cannot be directly compared with the real height of the investigated objects, the A-type domains seem too small to be formed by intact Fe_4Ph molecules. This interpretation is also supported by the bi-lobed and flat shape of the single units within the ordered domains (Fig. 71c). On the other hand the spherical shape of B-type objects and the greater height of their islands lead to the conclusion that Fe_4Ph molecules can be associated with these domains. However, the lack of high resolution images does not allow having a better insight. In fact the formation of big, apparently disordered, islands prevents us from getting good resolution in the B-domains. The formation of such big islands can be related to a high mobility of the molecules on the Au(111) surface, which induces aggregation processes.

As far as A-type domains are concerned, they are suspected to be fragments of disintegrated Fe_4Ph molecules. The contamination with fragments is particularly evident at very low coverage while it becomes practically undetectable for higher ones. Due to the very fragile nature of the polynuclear SMMs (Sönke Voss et al. 2008;

Mannini et al. 2008), it is possible to hypothesize different origins for the decomposition process. It could be generated during the sublimation process or simply be due to a surface-mediated fragmentation of the cluster.

Before trying to improve the morphological quality of the images of the B-domains, a test was performed in order to have some insight on the decomposition process.

4.1 Back exposure sublimation test

In order to shed more light on the process involved in the formation of A domains, a simple test was performed by using the sublimation geometry shown in fig. 72. The clean Au(111) crystal was kept in the preparation chamber for 80 minutes with the crucible at the sublimation temperature (215 °C) but without exposing the sample to the direct flux of the molecules. The surface was then investigated by STM. In large scale images (fig. 73a) the surface appears covered by a densely packed layer through which the corrugation of the herring bone reconstruction of the Au(111) surface can be still detected.

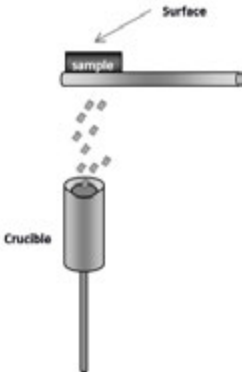

Fig. 72: Back exposure geometry. The sample is not directly exposed to the molecular flux coming from the crucible.

A close inspection by STM of the surface (see the enlargement in fig. 73b) reveals a textured layer of small objects similar to that observed in the A-type domains of the 0.25 nm Fe_4Ph sample (see fig. 71c). No trace of the B-type (Fe_4Ph) islands is revealed. This observation suggests the presence of very volatile species that can be stuck on the surface even if the sample is not directly exposed to the flux coming from the crucible. The probability that Fe_4Ph molecule, as big as they are, can bounce on the chamber walls then be able to reach the sample surface is expected to be lower than for smaller, more volatile fragments.

A partial decomposition of the Fe_4 molecules during the sublimation process seems more likely than a surface induced fragmentation. By looking at the shape of

the A objects we can speculate that they are formed by dpm-containing species. Images with objects with similar shape have been indeed reported in the study of the dissociation of a chromium tris-diketonato complex on Cu(100) surface (Grillo et al. 2002).

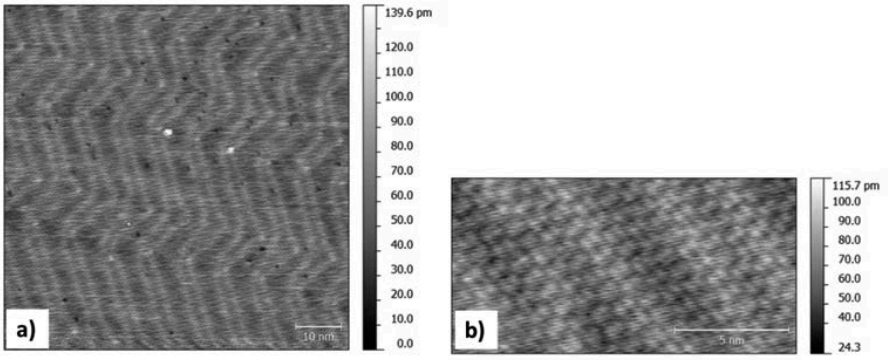

Fig. 73: Large scale STM image of the 80 min back exposed sample (3 pA; 2 V; 110x110 nm^2) (a), in the enlargement (3 pA; 2 V; 15x7.5 nm^2) (b) the textured layer formed by A-type molecule.

5 STM investigation on Cu(100) surface

Assuming that only domains of type B are compatible with intact Fe_4Ph molecules, it is quite evident that the molecules tend to aggregate into islands, hampering the collection of high resolution images. It would be therefore advisable to reduce the mobility of the molecules. This could be achieved simply sublimating the molecules on cooled surfaces. Unfortunately our UHV system does not allow such a procedure. An alternative way is the deposition on more reactive surfaces like Cu(100). This surface is more reactive than the Au(111) one and could allow the onset of stronger molecule-surface interactions, thus reducing molecules mobility.

Again a sub-monolayer sample with similar coverage as the previous one, 0.25 nm, was prepared. The sample was cooled down to 35 K before being investigated. The STM image reported in fig. 74a clearly shows islands formed by well-defined spherical objects and, underneath, a wetting layer arranged in dendritic structures. As in the case of Au(111), the height of the islands measures 0.72±0.02 nm while the dendritic structures are height 0.19±0.01 nm (see profile of fig. 74b). The two structures were labelled as A' (0.19 nm height) and B' (0.72 nm height) in analogy to the A and B islands on Au(111) surface. It is important to point out that the B' height is referred to the A' under layer (fig 74b) while in the Au(111) surface is referred to the bare gold. Among the A' layer spherical objects (labelled as C') are present with a

lateral dimension of 1.9±0.2 nm. A correct height estimation of the C' objects is difficult since it is not possible to discern if they lie in direct contact with the copper surface or above the A' islands. The good resolution obtained for islands of B' domains allows the estimation of the lateral dimensions of the spherical objects, i.e. 1.8±0.4 nm, which is in agreement with the expected dimension of intact Fe_4Ph molecules (ca. 1.7 nm). These data suggest that the molecules forming the B' regions could be intact Fe_4Ph molecule.

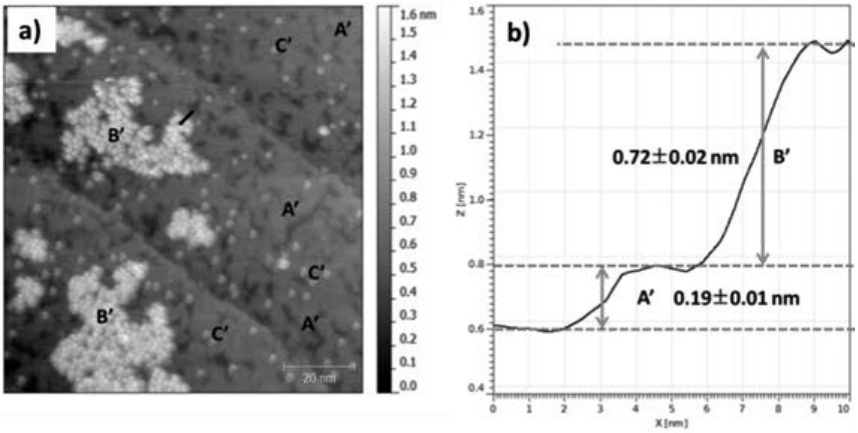

Fig. 74: STM investigation of 5 min sublimated sub-monolayer film on Cu(100) substrate (3p A; 2.5 V; 100x100 nm^2) (a); and a profile of the image (b).

By comparing large scale images (400x400 nm^2) obtained for 0.25 nm of Fe_4Ph on Cu(100) and Au(111), it is possible to note the B/A (B'/A') coverage ratio (molecules/contaminants) is higher for the Au(111) surface with respect to the Cu(100). The homogenous aspect of A'-type domains suggests that B' islands are probably grown on top of the A' structures which can act as decoupling layer from the bare Cu(100) surface. These findings can be interpreted in two ways: a surface effect in the Fe_4Ph molecule stability or in terms of sticking coefficients of the preformed fragments. In both cases a higher proportion of A-type domains is to be expected for Cu(100) and no unambiguous hint on surface effect can be extrapolated from this experiment. Unfortunately XPS technique cannot provide more insight. In fact, using the Al K_α source the Fe *2p* regions reside at the same energy of the $L_2M_{23}M_{23}$ Cu Auger peak, which overwhelms the iron components.

The presence of molecule-surface interactions are certainly related to the nature of the substrate and the investigation of the sublimation of Fe_4Ph on a less reactive substrate could allow a more complete view of the phenomenon.

6 STM investigation on Cu_2N/Cu(100) surface

The Cu_2N surface is an inert surface which has been used as electronic decoupling layer in Inelastic Electron Tunnelling Spectroscopy (IETS) studies on single atoms (Hirjibehedin et al. 2006; Otte et al. 2008; Loth, von Bergmann, et al. 2010; Loth, Etzkorn, et al. 2010). In fact the presence of the Cu_2N layer allows the decoupling of magnetic impurities i.e. transition element atoms such as Fe, Mn and Co, from the valence band of the Cu(100). Although the magnetic core of the Fe_4Ph molecule is expected to be decoupled from the surface by the ligands, the Cu_2N surface represents a good standard for further investigations. The Cu_2N surface can be obtained by sputtering the Cu(100) surface with N_2 (using 1 keV energy and 0.25 $\mu A \cdot cm^{-2}$) and annealing at 300 °C for 10 min. Depending on the sputtering time different coverage of Cu_2N can be achieved. However the growth of the Cu_2N overlayer is self-limited to 1 ML and no multilayer of copper nitride can be obtained.

The STM image in fig. 75a shows a 30% coverage of Cu_2N islands on Cu(100) surface. The surface is covered by square small islands with lateral dimension of ca. 7.5 nm. This structure is due to the incommensurate nature of the Cu_2N lattice (fig. 75b) respect to the lattice of the underlying Cu(100). The dimensions of the islands are thus a compromise between the strain and the edge energy (Choi et al. 2008; Leibsle et al. 1994; Komori et al. 2002). By increasing the sputtering time a full layer of Cu_2N can be obtained. The STM image of clean Cu_2N layer is reported in fig. 75c.

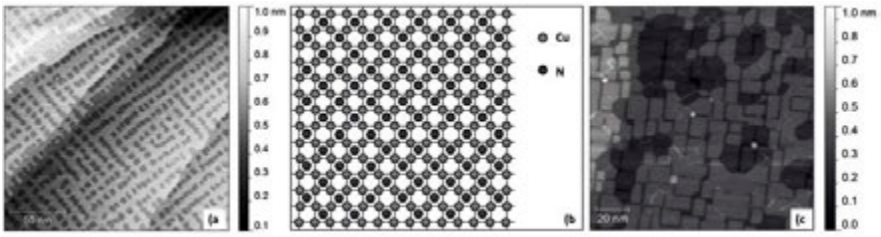

Fig. 75: STM image of 30 % Cu_2N coverage islands on Cu(100)(200p A; 2 V; 200x200 nm^2)(a); Atomic structure of C(2x2) Cu_2N surface(b);STM image of clean Cu_2N (200 pA; 2 V; 140x140 nm^2)(c).

We studied a similar 0.25 nm sub-monolayer coverage of Fe_4Ph also on the Cu_2N surface. The large scale images of the hybrid surface (fig. 76a) revealed the presence of islands with ca. 0.8±0.1 nm (B") similar to what found on Au(111) and Cu(100) surfaces. The lateral dimension of the B" spherical objects are 1.6±0.2 nm comparable to what we measured on Cu(100) and to the real dimension of the Fe_4Ph molecule (ca. 1.7 nm). By focusing on the areas between the B" structures the presence of small objects with height of 0.28±0.02 nm (A") was found (fig. 76b,c). It's in-

teresting to note that on the Cu_2N surface the small molecules are not able to aggregate in large domains, as observed on the other surfaces, and they present a tetra-lobed shape. The tetra-lobed shaped objects remind in some way the bi-lobed objects observed on the Au(111) surface. While in the latter case they self-assemble to form large ordered domains, in the case of Cu_2N they seem to be coupled in pairs to form the tetra-lobed elements. The hole observed in the middle of the image suggests that two bi-lobed objects are coordinating something, i.e. an iron ion or a defect of the surface. As in the case of the Cu(100) substrate the XPS technique does not provide further insight (see section 4 paragraph 6).

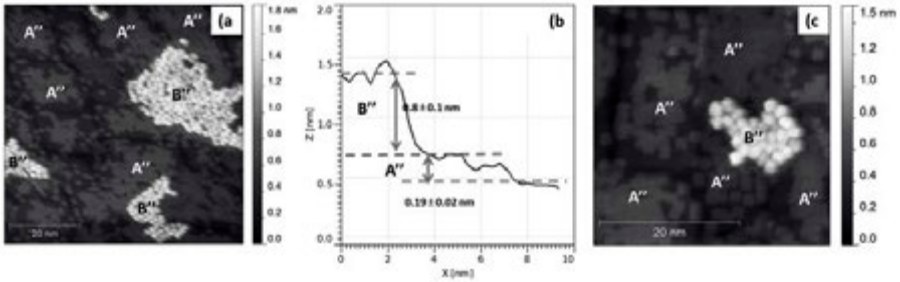

Fig. 76: (a) STM image of 0.25 nm of Fe_4Ph on Cu_2N (3 pA; 2.5 V; 70x70 nm^2) (b); the profile corresponding to the pink line traced in a); (c) and the enlargement where is visible the tetra-lobed shape of the A structure (3 pA; 2.5 V; 35x35 nm^2).

The data presented here suggest the presence of intact Fe_4Ph on surface combined also with a relevant fraction of a contaminant. In order to prove the intactness of the Fe_4Ph molecules Scanning Tunnelling Spectroscopy (STS) was employed (see section 2. Paragraph 8.3). The measurements were performed on a different UHV-STM system which was designed to achieve the high performance required for IETS charachterisation.

7 STS and IETS measurements

The STS measurements were carried out at the Max Planck Research Group - Dynamics of Nanoelectronic Systems in Hamburg. Thanks to the collaboration with Dr. S. Loth and his group I had the opportunity to work for three weeks in their laboratory. We obtained first encouraging results and more detailed experiments are being carried out. Being able to perform low temperature STS measurements on a complex and fragile molecule like Fe_4 is an important achievement in itself. In this section the first spin excitation spectra consistent with intact Fe_4 molecules and their preliminary analysis will be presented. The UHV-STM in Hamburg is specifically designed to perform Inelastic Electron Tunnelling Spectroscopy (IETS) for the study

of the electronic and magnetic properties of single atoms, nanostructures and molecules. The STM, equipped with a pumped ^{3}He cooling system, can perform measurements down to 0.4 K allowing the study of the Fe_4Ph molecule below its blocking temperature. It is also equipped with a vectorial superconductive magnet, which allows the application of a magnetic field up to 90 kOe along the STM junction direction and up to 20 kOe in an arbitrary direction.

The d(I)/d(V) spectra were acquired using a lock-in detection of an applied bias modulation. In this STM the tip is grounded and the potential is applied to the sample, it is therefore opposite to the Omicron STM instrument (section 2 paragraph 9.3). For the sample preparation we adapted our experimental sublimation setup (see section 2 paragraph 2) to their UHV system. In order to avoid the formation of molecular domains and to freeze the single molecules on the surface the sublimation process was carried out with the sample kept at 4 K. We employed the Cu_2N surfaces as substrate because it does not allow the formation of large islands and the B" objects lay in direct contact with the bare surface. The analysis of the STM images reveals that both the A'' and B'' molecules are present on the surface. We focused our investigation only on the B" molecules which, as demonstrated in the previous paragraphs, can be considered Fe_4Ph candidates.

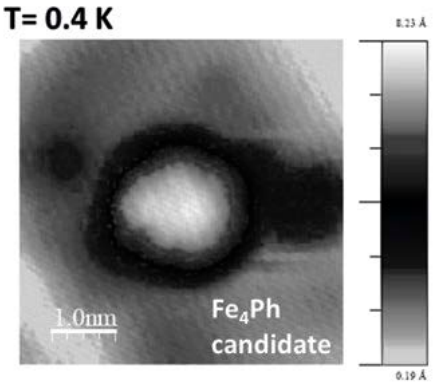

Fig. 77: STM image of single B" molecule sublimated on Cu_2N surface. The image was acquired at 0.4 K (3 pA; 2.0 V; 5x5 nm^2).

The STM image of isolated B" molecules, acquired with both STM tip and sample at 0.5 K, is reported in fig. 77. Their apparent height and lateral dimensions are in agreement with those revealed in the previous experiment. On such candidates several attempts were carried out to look for the HOMO/LUMO features in the differential conductance curves acquired on top of the molecules. These measurements were partially hampered by the molecular fragility i.e. molecular fragmentation during the bias sweep (few V), and no clear data were recorded to be compared with the experimental and theoretic density of states.

Our study was then focused on a small sweep range (few mV) centred in zero bias, which was disrupting for the molecules. In this energy range inelastic tunnelling processes related to spin excitation transitions can be detected. The tunnelling process can in fact occur following two pathways: by elastic and by inelastic tunnelling. In the former case the electron does not interact with the environment while in the inelastic process the electron exchanges energy during the tunnelling process through the molecule.

The inelastic tunnelling process can be employed to achieve information on the energy levels of the inspected system. In fact, it has been first used in planar junction to study vibrational excitations in molecules (Hansma & Kirtley 1978; Jaklevic & Lambe 1966; Weinberg 1978). Then the STM technique has enabled the study of spin excitation in single magnetic metal atoms, nanostructures (Heinrich et al. 2004; Hirjibehedin et al. 2006; Hirjibehedin et al. 2007; Loth et al. 2012), and SMMs (Kahle et al. 2012).

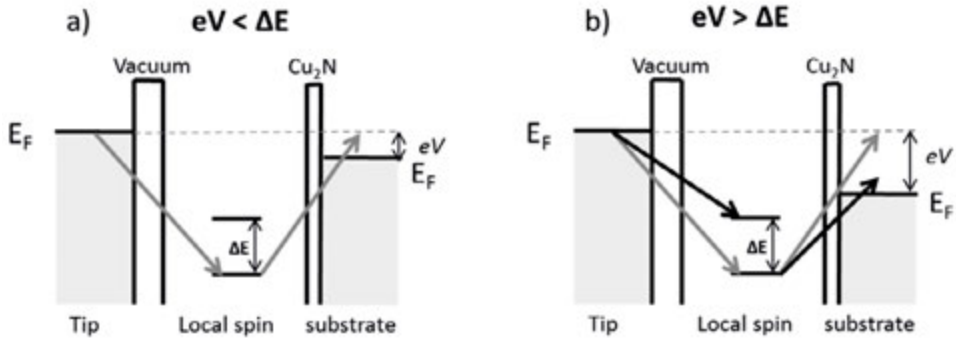

Fig. 78: Scheme of the tunnelling processes; When the electron energy, i.e. the applied bias *eV*, is less than the energy required for the molecular transition only the elastic process is present (grey arrows)(a); on the contrary when the electrons energy is enough to excite the spin system the inelastic tunnelling can occur (black arrows) opening a new tunnelling channel and increasing the differential conductance.

To briefly explain the main concepts of the spin excitation process let us consider a spin system inside the tunnelling gap i.e. between the tip and the surface (fig. 78). The grey arrows in fig. 78 represent the elastic tunnelling. This tunnelling channel is always available, regardless of applied bias, provided there are filled states in one electrode and empty state in the opposite electrode at the same energy. However, when electrons possess enough energy they can interact with the local spin promoting a transition within the sublevels of the spin and still reach empty states (fig. 78b). This process constitutes the inelastic tunnelling phenomenon and it can be considered as an additional conduction channel. Thus, when the applied bias match-

es the required energy for the spin transition to be excited the inelastic channel becomes available. This leads to an increase of the conductance of the system which is now formed by both the elastic and inelastic conduction channels. The spin excitation process is thus detected as a step in the differential conductance. It is important to note that the threshold voltages at which the steps are observed corresponds to the energy of the excitations.

In fig. 79a is reported the differential conductance d(I)/d(V) curves acquire on the bare Cu_2N substrate and on B" molecule in zero magnetic field. As expected the curve on Cu_2N is flat while the one recorded on the molecule is characterised by two steps close to the zero bias value, which look like a negative peak (fig. 79a). These features can be attributed the presence of spin excitation process. At 0.5 K the ground state of the double well $|S, m_s\rangle$=$|5, \pm5\rangle$ is selectively populated and the inelastic process excite the spin levels of the molecule to the $|5, \pm4\rangle$ states (fig. 79b). The features in the differential curve of the B" molecule is indicative of inelastic tunnelling process onset above a bias of absolute value ca. 0.5 mV. This is in agreement with the expected calculated energy involved in $|5, \pm5\rangle$ to $|5, \pm4\rangle$ transition of Fe_4Ph, i.e. 0.47 meV.

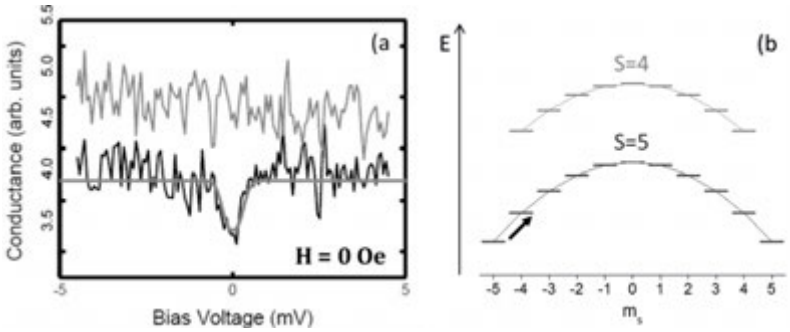

Fig. 79: IETS measurement on top of B" molecule (lower black) and the same measurement on bare Cu_2N surface (upper grey) acquired using lock-in detection at 768 Hz and 100 μV amplitude modulation and calculated spectra (lower grey)(a). Fe_4Ph levels scheme (b), at 0.4 K the system resides in the ground state $|\mathbf{5}, \pm\mathbf{5}\rangle$and the inelastic tunnelling can excite the molecule to the $|\mathbf{5}, \pm\mathbf{4}\rangle$ states; the black arrow indicates the possible excitation which obeys to the spin selection rules $\Delta S=0, \pm1$ and $\Delta m_s=0, \pm1$. Graph in panel (a) courtesy of Dr. J. Burgess, Hamburg.

These measurements clearly demonstrate the capability of the technique to provide fine details on the electronic structure of the deposited species at the single-molecule level. However, the fragile nature of the Fe_4 molecules makes the IETS experiment rather challenging. The presence of this spin excitation in fact was not con-

sistently detected on every candidate and a larger set of data must be acquired to confirm these preliminary results.

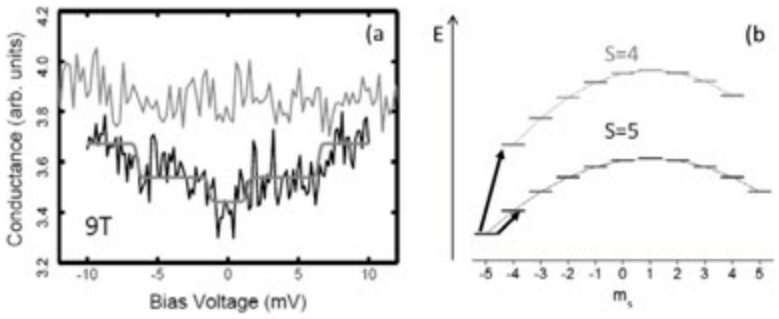

Fig. 80: IETS measure on top of B" molecule (lower black) and the same measure on bare Cu_2N surface (upper grey) acquired using lock-in detection at 768 Hz and 100 μV amplitude modulation and calculated spectra (lower grey)(a). Simplified Fe_4Ph levels scheme (b) considering the field applied along the molecular easy axis. The black arrows indicate the possible excitation which obeys to the spin selection rules $\Delta S=0, \pm 1$ and $\Delta m_s=0, \pm 1$. Graph in panel (a) courtesy of Dr. J. Burgess, Hamburg.

The experiment was repeated applying 90 kOe magnetic field normal to the sample surface. The magnetic field can be taken in account in the Hamiltonian description introducing the Zeeman term which removes the degeneracy of the $|5, \pm 5\rangle$ states. The spectra acquired are reported in fig. 80a. The measure was performed using a larger bias range compared to the zero field measurement. This allowed the observation of four steps: two at ca. 1 mV and two at ca. 7 mV absolute bias values.

The higher energy steps could be associated to a process involving a transition from the $S=5$ ground state to the first excited total spin state, characterised by $S=4$, as depicted in fig. 80b. This feature was also present in zero magnetic field measurements. It is however important to notice that this spectral feature at higher bias showed a variability significantly larger than the one observed at low bias. Although the different orientation of the Fe_4 molecules on the substrate could be at the origin of the differences observed under applied magnetic field, the residual inconsistencies suggest that other factors, like the chemical instability of the molecules in the experimental conditions, must be taken into account. Further investigations are therefore needed for a reliable assignment of these spectral features.

The lower grey spectra in fig. 79 and fig. 80 show the expected spin excitation spectra for intact Fe_4 molecules for comparison. The conductance spectra were simulated using the Fe_4 spin anisotropy parameters from ref. (Mannini et al. 2009) under the assumption that tunnelling interaction happens with the Fe atoms individually. The calculations were performed by Dr. S. Loth using scattering theory in

1st Born approximation. The transition intensities were computed using an interaction Hamiltonian:

$$H = \vec{\sigma} \cdot \vec{S} + u \qquad (50)$$

where $\vec{\sigma}$ is the electron spin, $\vec{S}$ is the spin of the Fe atoms and u is a spin independent scattering term (Loth, Lutz, et al. 2010). This operator acts on the product states of the tunneling electron and molecule spin. In this way the selection rules are imposed by energy and angular momentum conservation; spin-dependent conduction channels can be accounted for.

Although only a preliminary characterisation of the spin excitation of Fe_4Ph molecules through IESTS has been possible during my stay in Hamburg, the results are rather encouraging, confirming that objects consistent with intact and isolated Fe_4 molecules can be detected and addressed at the Cu_2N surface. Moreover, the observation of spectroscopic features in agreement with the ones predicted assuming the Spin Hamiltonian parameters of Fe_4 molecules in the crystalline phase suggests that the magnetic features of this SMM are very robust. These novel results corroborate the observation of magnetic bistability in self-assembled monolayers by XMCD, or the detection of spectroscopic features in the conductivity inside nano-gap electrodes (Heersche et al. 2006; Zyazin et al. 2010; Zyazin et al. 2011) and open the fascinating perspective of detecting the magnetic bistability, and related memory effect, at the single molecule level by using scanning-probe microscopy techniques.

Section 5
Conclusion

In this work we have presented two molecular systems: the $TbPc_2$ and the Fe_4Ph SMMs. Both of them can be sublimated allowing the preparation of hybrid surfaces employing the ultimate cleanliness of the UHV environment.

$TbPc_2$ is considered the archetypal of sublimable SMMs and the ideal candidate for investigations with scanning probe techniques. However, we have demonstrated that its magnetic properties are strongly influenced by the surrounding environment. We have indeed proven that its slow relaxation of the magnetization depends on the molecular packing. Despite the many experiments performed by us and others a rationalization of its properties and a full comprehension of the role played by the exchange interactions is lacking. Nevertheless, $TbPc_2$, thanks to its relative high blocking temperature, is an interesting candidate for OSPDs. Moving toward this type of applications we have investigated the role played by the presence of a magnetic conducting substrate in the hysteretic behaviour of the $TbPc_2$. Our study has concerned metallic cobalt and LSMO, two of the most employed ferromagnetic electrodes in molecular spin valves. The results we have presented here suggest that no significant polarisation of the $TbPc_2$ magnet moments is induced by the magnetic Co and LSMO substrates. However, this does not diminish the interest in this type of molecules, and magneto-transport experiments on devices embedding $TbPc_2$ molecules are likely to be the focus of this research in a near future.

On the other hand, Fe_4Ph molecules show a more predictable magnetic behaviour and, albeit the low blocking temperature of the system that makes them less appealing for OSPDs, the investigation of its electron transport properties could allow to have a reliable picture of the role played by magnetic molecules at the interface between the ferromagnetic electrodes and the organic semiconductor. Within this framework we have exploited the sublimation of Fe_4Ph in order to investigate the hybrid surfaces by means of STM and STS techniques.

Our characterisation has allowed to address the spin excitation signal of an isolated Fe_4Ph molecule. This first important step opens new possibility for the investi-

Luigi Malavolti, *Single molecule magnets sublimated on conducting and magnetic substrates*,
ISBN 978-88-6655-969-6 (print) ISBN 978-88-6655-970-2 (online)

gation of the magnetic and electronic properties of this rich and versatile class of SMMs at the single molecule level.

References

Abragam, A. & Bleaney, B., (2012) *Electron Paramagnetic Resonance of Transition Ions* Oxford Classic Texts in the Physical Sciences.

Accorsi, S. et al., (2006) Tuning anisotropy barriers in a family of tetrairon(III) single-molecule magnets with an S = 5 ground state. *Journal of the American Chemical Society*, 128(14), 4742–55.

Allmers, T. & Donath, M., (2011) Controlling Cu diffusion in Co films grown on Cu(001). *Surface Science*, 605(21-22), 1875–1880.

Bardeen, J., 1961. Tunnelling from a Many-Particle Point of View. *Physical Review Letters*, 6(2), 57–59.

Barone, A. & Paternò, G., (1982) *Physics and applications of the Josephson effect.* Wiley-interscience.

Barra, A.L. et al., (1999) Single-Molecule Magnet Behavior of a Tetranuclear Iron(III) Complex. The Origin of Slow Magnetic Relaxation in Iron(III) Clusters. *Journal of the American Chemical Society*, 121(22), 5302–5310.

Biswas, I. et al., (2007) Buried interfacial layer of highly oriented molecules in copper phthalocyanine thin films on polycrystalline gold. *The Journal of chemical physics*, 126(17), p.174704.

Biswas, I. et al., (2009) Initial molecular orientation of phthalocyanines on oxide substrates. *Physica status solidi* (a), 206(11), 2524–2528.

Blundell, S.J. et al., (2003) μSR studies of organic and molecular magnets. *Polyhedron*, 22(14-17), 1973–1980.

Bogani, L. & Wernsdorfer, W., (2008) Molecular spintronics using single-molecule magnets. *Nature materials*, 7(Box 1), 179–186.

Branzoli, F. et al., (2011) Low-energy spin dynamics in the [YPc_{2}]^{0} S=1/2 antiferromagnetic chain. *Physical Review B*, 83(17), p.174419.

Branzoli, F. et al., (2010) Spin and charge dynamics in [TbPc_{2}]^{0} and [DyPc_{2}]^{0} single-molecule magnets. *Physical Review B*, 82(13), p.134401.

Branzoli, F. et al., (2009) Spin dynamics in the neutral rare-earth single-molecule magnets [TbPc2]0 and [DyPc2]0 from μSR and NMR spectroscopies. *Physical Review B*, 79(22), p.220404.

Bräuer, B. et al., (2009) Magneto-optical Kerr effect spectroscopy--a sensitive tool for investigating the molecular orientation in organic semiconductor films. *The journal of physical chemistry.* B, 113(45), 14957–61.

Luigi Malavolti, *Single molecule magnets sublimated on conducting and magnetic substrates*,
ISBN 978-88-6655-969-6 (print) ISBN 978-88-6655-970-2 (online)

Brongersma, H. et al., (2007) Surface composition analysis by low-energy ion scattering. *Surface Science Reports*, 62(3), 63–109.

Brongersma, H.H. et al., (1998) A round robin experiment of elemental sensitivity factors in low-energy ion scattering. *Nuclear Instruments and Methods in Physics Research Section B: Beam Interactions with Materials and Atoms*, 142(3), 377–386

Bukel, (1991) *Superconductivity: Fundamentals and Applications.* VCH, Weinheim.

Campo, G., (2012) Magneto-optical investigation on nanostructured magneto-plasmonic materials. PhD thesis.

Car, P.-E. et al., (2011) Giant field dependence of the low temperature relaxation of the magnetization in a dysprosium(III)-DOTA complex. *Chemical communications*, 47(13), 3751–3.

Carra, P. & Altarelli, M., (1993) X-Ray Circular Dichroism and Local Magnetic Field. *Physical Review Letters*, 70(5), 694–697.

Casimir, H.B.G. & du Pré, F.K., (1938) Note on the thermodynamic interpretation of paramagnetic relaxation phenomena. *Physica*, 5(6), 507–511.

Casimir, H.B.G. & du Pré, F.K., (1938) Note on the thermodynamic interpretation of paramagnetic relaxation phenomena. *Physica*, 5(6), p.507.

Chen, C. et al., (1995) Experimental Confirmation of the X-Ray Magnetic Circular Dichroism Sum Rules for Iron and Cobalt. *Physical Review Letters*, 75(1), 152–155.

Choi, T., Ruggiero, C. & Gupta, J., (2008) Incommensurability and atomic structure of c(2×2)N/Cu(100): A scanning tunneling microscopy study. *Physical Review B*, 78(3), p.035430.

De Cian, A. et al., (1985) Synthesis, structure, and spectroscopic and magnetic properties of lutetium(III) phthalocyanine derivatives: LuPc2.CH2Cl2 and [LuPc(OAc)(H2O)2].H2O.2CH3OH. *Inorganic Chemistry*, 24(20), 3162–3167.

Clark, J. & Braginski, A.I., (2004) *The SQUID Handbook.* Wiley-VCH.

Cole, K.S. & Cole, R.H., (1941) Dispersion and Absorption in Dielectrics I. Alternating Current Characteristics. The Journal of Chemical Physics, 9(4), p.341.

Cornia, A. et al., (2011). Chemical strategies and characterization tools for the organization of single molecule magnets on surfaces. *Chemical Society reviews*, 40(6), 3076–91.

Cornia, A. et al., (2004) Energy-Barrier Enhancement by Ligand Substitution in Tetrairon(III) Single-Molecule Magnets. *Angewandte Chemie*, 116(9), 1156–1159.

Cornia, A. et al., (2004) Tuneable energy barriers in tetrairon(III) single-molecule magnets. *Journal of Magnetism and Magnetic Materials*, 272-276, E749–E751.

Dediu, V. et al., (2002) Room temperature spin polarized injection in organic semiconductor. *Solid State Communications*, 122(3-4), 181–184.

Dediu, V.A. et al., (2009) Spin routes in organic semiconductors. *Nature materials*, 8(9), 707–16.

Dirac, P.A.M., 1929. The Quantum Theory of the Electron Proceeding of the Royal Society of London, A123, p.714.

Dunford, C.L., Williamson, B.E. & Krausz, E., (2000) Temperature-Dependent Magnetic Circular Dichroism of Lutetium Bisphthalocyanine. *The Journal of Physical Chemistry A*, 104(16), 3537–3543.

Eckstein, W., (1991). *Computer Simulation of Ion-Solid Interactions*. Springer: Berlin.

Einstein, A., (1905) photoemission. *Annalen der Physik*, 17, p.132.

Ernzerhof, M. & Scuseria, G.E., (1999) Assessment of the Perdew–Burke–Ernzerhof exchange-correlation functional. The Journal of Chemical Physics, 110(11), p.5029.

Feenstra, R. & Mårtensson, P., (1988) Fermi-Level Pinning at the Sb/GaAs(110) Surface Studied by Scanning Tunneling Spectroscopy. *Physical Review Letters*, 61(4), 447–450.

Fu, Y.-S. et al., (2012) Reversible chiral switching of bis(phthalocyaninato) terbium(III) on a metal surface. *Nano letters*, 12(8), 3931–5.

Fudamoto, Y. et al., (2002) Muon spin relaxation in the spin-ring system Cu3WO6: Quasistatic spin freezing at 7.0 K. Physical Review B, 65(17), p.174428.

Funk, T. et al., (2005) X-ray magnetic circular dichroism—a high energy probe of magnetic properties. *Coordination Chemistry Reviews*, 249(1-2), 3–30.

Gatteschi, D., Sessoli, R. & Villain, J., (2006) *Molecular Nanomagnets* Oxford University Press, ed., Oxford.

Goedecker, S., Teter, M. & Hutter, J., (1996) Separable dual-space Gaussian pseudopotentials. *Physical Review B*, 54(3), 1703–1710.

Gonidec, M. et al., (2010) Probing the Magnetic Properties of Three Interconvertible Redox States of a Single-Molecule Magnet with Magnetic Circular Dichroism Spectroscopy. *Journal of the American Chemical Society*, 132, 1756–1757.

Graziosi, P. et al., (2013) Conditions for the growth of smooth La0.7Sr0.3MnO3 thin films by pulsed electron ablation. *Thin Solid Films*, 534, 83–89.

Grillo, S.E. et al., (2002) STM observation of the dissociation of a chromium tris-diketonato complex on Cu (1 0 0). *Chemical Physics Letters*, 355(April), 289–293.

Grimme, S. et al., (2010) A consistent and accurate ab initio parametrization of density functional dispersion correction (DFT-D) for the 94 elements H-Pu. *The Journal of chemical physics*, 132(15), 154104.

Hansma, P.K. & Kirtley, J., (1978) Recent advances in inelastic electron tunneling spectroscopy. *Accounts of Chemical Research*, 11(12), 440–445.

Hayano, R. et al., (1979) Zero-and low-field spin relaxation studied by positive muons. *Physical Review B*, 20(3), 850–859.

Heersche, H. et al., (2006) Electron Transport through Single Mn12 Molecular Magnets. *Physical Review Letters*, 96(20), p.206801.

Heinrich, A.J. et al., (2004) Single-atom spin-flip spectroscopy. *Science*, 306(5695), 466–9.

Hirjibehedin, C.F. et al., (2007) Large magnetic anisotropy of a single atomic spin embedded in a surface molecular network. *Science*, 317(5842), 1199–203.

Hirjibehedin, C.F., Lutz, C.P. & Heinrich, A.J., (2006) Spin coupling in engineered atomic structures. *Science*, 312(5776), 1021–4.

Hofmann, A. et al., 2012. Depth-dependent spin dynamics in thin films of TbPc2 nanomagnets explored by low-energy implanted muons. *ACS nano*, 6(9), pp.8390–6.

Ishikawa, N. et al., (2003) Lanthanide Double-Decker Complexes Functioning as Magnets at the Single-Molecular Level. *Journal of the American Chemical Society*, 125, 8694–8695.

Ishikawa, N. et al., (2004) Upward temperature shift of the intrinsic phase lag of the magnetization of Bis(phthalocyaninato)terbium by ligand oxidation creating an S = 1/2 spin. *Inorganic chemistry*, 43(18), 5498–500.

Ishikawa, N., Sugita, M. & Wernsdorfer, W., (2005) Quantum tunneling of magnetization in lanthanide single-molecule magnets: bis(phthalocyaninato)terbium and bis(phthalocyaninato)dysprosium anions. *Angewandte Chemie*, 44(19), 2931–5.

Jaklevic, R. & Lambe, J., (1966) Molecular Vibration Spectra by Electron Tunneling. *Physical Review Letters*, 17(22), 1139–1140.

Jo, M.-H. et al., (2006) Signatures of molecular magnetism in single-molecule transport spectroscopy. *Nano Letters*, 6(9), 2014–2020.

Kahle, S. et al., (2012) The quantum magnetism of individual manganese-12-acetate molecular magnets anchored at surfaces. *Nano letters*, 12(1), 518–21.

Katoh, K. et al., (2009) Direct observation of lanthanide(III)-phthalocyanine molecules on Au(111) by using scanning tunneling microscopy and scanning tunneling spectroscopy and thin-film field-effect transistor properties of Tb(III)- and Dy(III)-phthalocyanine molecules. *Journal of the American Chemical Society*, 131(29), 9967–76.

Katoh, K., Isshiki, H., et al., (2012) Molecular spintronics based on single-molecule magnets composed of multiple-decker phthalocyaninato terbium(III) complex. *Chemistry an Asian journal*, 7(6), 1154–69.

Katoh, K., Horii, Y., et al., (2012) Multiple-decker phthalocyaninato dinuclear lanthanoid(III) single-molecule magnets with dual-magnetic relaxation processes. *Dalton transactions*, 41(44), 13582–600.

Khajetoorians, A.A. et al., (2011) Realizing all-spin-based logic operations atom by atom. *Science*, 332(6033), 1062–4.

Klar, D. et al., (2013) Antiferromagnetic coupling of TbPc2 molecules to ultrathin Ni and Co films. *Beilstein journal of nanotechnology*, 4(100), 320–4.

Komeda, T. et al., (2011) Observation and electric current control of a local spin in a single-molecule magnet. *Nature communications*, 2, p.217.

Komori, F., Ohno, S. & Nakatsuji, K., (2002) Arrays of magnetic nanodots on nitrogen-modified Cu(001) surfaces. Journal of Physics: *Condensed Matter*, 14(35), 8177–8197.

Kowalewski, M., Schneider, C.M. & Heinrich, B., (1993) Thickness and temperature dpendence of magnetic anisotropies in ultrthin fcc Co(001) structures. *Physical Review B*, 47(14), 8748–8753.

Kramers, H.A.Z., (1926) *Phys.*, 39, 826–840.

Lascialfari, A. et al., (1998) Thermal Fluctuations in the Magnetic Ground State of the Molecular Cluster Mn12O12 Acetate from μSR and Proton NMR Relaxation. *Physical Review Letters*, 81(17), 3773–3776.

Lehmann, J. et al., (2007) Spin qubits with electrically gated polyoxometalate molecules. *Nature nanotechnology*, 2(5), 312–7.

Leibsle, F.M. et al., (1994) STM observations of Cu(100)–c(2×2)N surfaces: evidence for attractive interactions and an incommensurate c(2 × 2) structure. *Surface science*, 317(3), 309–20.

Leuenberger, M.N. & Loss, D., (2001) Quantum computing in molecular magnets. *Nature*, 410(6830), 789–93.

Li, F. et al., (2011) Modified Surface Electronic and Magnetic Properties of La 0.6 Sr 0.4 MnO 3 Thin Films for Spintronics Applications. *The Journal of Physical Chemistry C*, 115(34), 16947–16953.

Lodi Rizzini, A. et al., (2011) Coupling Single Molecule Magnets to Ferromagnetic Substrates. *Physical Review Letters*, 107(17), p.177205.

Lodi Rizzini, A. et al., (2012) Exchange biasing single molecule magnets: coupling of TbPc2 to antiferromagnetic layers. *Nano letters*, 12(11), 5703–7.

Lopez, N. et al., (2009) Heterospin single-molecule magnets based on terbium ions and TCNQF(4) radicals: interplay between single-molecule magnet and phonon bottleneck phenomena investigated by dilution studies. *Chemistry European Journal*, 15(42), 11390–400.

Loth, S. et al., (2012) Bistability in atomic-scale antiferromagnets. *Science*, 335(6065), 196–9.

Loth, S., von Bergmann, K., et al., (2010) Controlling the state of quantum spins with electric currents. *Nature Physics*, 6(5), 340–344.

Loth, S., Etzkorn, M., et al., (2010) Measurement of fast electron spin relaxation times with atomic resolution. *Science*, 329(5999), 1628–30.

Loth, S., Lutz, C.P. & Heinrich, A.J., (2010) Spin-polarized spin excitation spectroscopy. *New Journal of Physics*, 12(12), p.125021.

Luis, F. et al., (2010) Spin-lattice relaxation via quantum tunneling in an Er^{3+}-polyoxometalate molecular magnet. *Physical Review B*, 82(6), p.060403.

Malavolti, L. et al., 2013. Erratic magnetic hysteresis of TbPc2 molecular nanomagnets. Journal of Materials Chemistry C, 1(16), 2935–42.

Malavolti, L. et al., 2013. Magnetism of TbPc2 SMMs on ferromagnetic electrodes used in organic spintronics. Chemical communications, 49(98), pp.11506–8.

Mannini, M. et al., (2009) Magnetic memory of a single-molecule quantum magnet wired to a gold surface. Nature materials, 8(3), 194–7.

Mannini, M. et al., (2010) Quantum tunnelling of the magnetization in a monolayer of oriented single-molecule magnets. *Nature*, 468(7322), 417–21.

Mannini, M. et al., (2008) XAS and XMCD investigation of Mn12 monolayers on gold. *Chemistry European Journal*, 14(25), 7530–5.

Margheriti, L., (2010) *Preparation and characterisation of SMM thin films obtained by UHV evaporation* . PhD thesis.

Margheriti, L. et al., (2009) Thermal deposition of intact tetrairon(III) single-molecule magnets in high-vacuum conditions. *Small*, 5(12), 1460–6.

Margheriti, L. et al., (2010) X-ray detected magnetic hysteresis of thermally evaporated terbium double-decker oriented films. *Advanced materials*, 22(48), 5488–93.

Miguel, J. et al., (2011) Reversible Manipulation of the Magnetic Coupling of Single Molecular Spins in Fe-Porphyrins to a Ferromagnetic Substrate. The Journal of *Physical Chemistry Letters*, 2(12), 1455–1459.

Mugarza, A. et al., (2012) Electronic and magnetic properties of molecule-metal interfaces: Transition-metal phthalocyanines adsorbed on Ag(100). *Physical Review B*, 85(15), p.155437.

Mundy, C.J. et al., CP2K theoretic calculation. CP2K software package.

Niehus, H. & Spitzl, R., (1991) Ion–solid interaction at low energies: Principles and application of quantitative ISS. *Surface and Interface Analysis*, 17(February), 287–307.

Otte, A.F. et al., (2008) The role of magnetic anisotropy in the Kondo effect. *Nature Physics*, 4(11), 847–850.

Paillaud, J. et al., (1991) Radical-based ferromagnetic chain in yttrium diphthalocyanine [YPc_{2}]·CH_{2}Cl_{2}. *Physical Review Letters*, 67(2), 244–247.

Prasad, T.K. et al., (2012) Magnetic and optical bistability in tetrairon(III) single molecule magnets functionalized with azobenzene groups. *Dalton transactions*, 41(27), 8368–78.

Prezioso, M. et al., (2013) A single-device universal logic gate based on a magnetically enhanced memristor. Advanced materials (Deerfield Beach, Fla.), 25(4), 534–8.

Ramsperger, U. et al., (1996) Growth of Co on a stepped and on a flat Cu(001) surface. *Physical review B*, 53(12), 8001–8006.

Rauschenbach, S. et al., (2009) Electrospray ion beam deposition: soft-landing and fragmentation of functional molecules at solid surfaces. ACS nano, 3(10), 2901–10.

Rigamonti, L. et al., (2013) Enhanced vapor-phase processing in fluorinated Fe4 single-molecule magnets. *Inorganic chemistry*, 52(10), 5897–905.

Rinehart, J.D. & Long, J.R., (2012) Slow magnetic relaxation in homoleptic trispyrazolylborate complexes of neodymium(III) and uranium(III). *Dalton transactions*, 41(44), 13572–4.

Rodriguez-Douton, M.J. et al., (2011) One-step covalent grafting of Fe4 single-molecule magnet monolayers on gold. *Chemical communications*, 47(5), 1467–9.

Salman, Z. et al., (2002) Dynamics at T→0 in half-integer isotropic high-spin molecules. *Physical Review B*, 65(13), p.132403.

Salman, Z. et al., (2010) Probing the magnetic ground state of the molecular dysprosium triangle with muon spin relaxation. *Physical Review B*, 82(17), p.174427.

Salman, Z., (2002) Theoretical Calculation for Isotropic High Spin Molecules. Cond-Mat/0209497, p.12.

Sanvito, S., (2011) Molecular spintronics. *Chemical Society reviews*, 40(6), 3336–55.

Scheybal, A. et al., (2005) Induced magnetic ordering in a molecular monolayer. *Chemical Physics Letters*, 411(1-3), 214–220.

Schlegel, C. et al., (2010) Magnetic properties of two new Fe(4) single-molecule magnets in the solid state and in frozen solution. *Chemistry European Journal*, 16(33), 10178–85.

Schwöbel, J. et al., (2012) Real-space observation of spin-split molecular orbitals of adsorbed single-molecule magnets. *Nature communications*, 3, p.953.

Selloni, A. et al., (1985) Voltage-dependent scanning-tunneling microscopy of a crystal surface: Graphite. *Physical Review B*, 31(4), 2602–2605.

Serrate, D. et al., (2010) Imaging and manipulating the spin direction of individual atoms. *Nature nanotechnology*, 5(5), 350–3.

Srivastava, P. et al., (1998) Magnetic moments and Curie temperatures of Ni and Co thin films and coupled trilayers. *Physical Review B*, 58(9), 5701–5706.

Stepanow, S. et al., (2011) Mixed-valence behavior and strong correlation effects of metal phthalocyanines adsorbed on metals. *Physical Review B*, 83(22), p.220401.

Stepanow, S. et al., (2010) Spin and orbital magnetic moment anisotropies of monodispersed bis(phthalocyaninato)terbium on a copper surface. *Journal of the American Chemical Society*, 132(34), 11900–1.

Stöhr, J., (1995) X-ray magnetic circular dichroism spectroscopy of transition metal thin films. *Journal of Electron Spectroscopy and Related Phenomena*, 75(0), 253–272.

Stohr, J. & Siegmann, H.C., (2006) *Magnetism - From Fundamentals to Nanoscale Dynamics*. Springer.

Stroscio, J., Feenstra, R. & Fein, A., (1986) Electronic Structure of the Si(111)2 × 1 Surface by Scanning-Tunneling Microscopy. *Physical Review Letters*, 57(20), 2579–2582.

Takamatsu, S. et al., (2007) Significant Increase of the Barrier Energy for Magnetization Reversal of a Single-4f-Ionic Single-Molecule Magnet by a Longitudinal Contraction of the Coordination Space. *Inorganic chemistry*, 46(18), 7250–7252.

Takamatsu, S. & Ishikawa, N., (2007) A theoretical study of a drastic structural change of bis (phthalocyaninato) lanthanide by ligand oxidation : Towards control of ligand field strength and magnetism of single-lanthanide-ionic single molecule magnet. *Polyhedron*, 26, 1859–1862.

Tersoff, J. & Hamann, D.R., (1983) Theory and Application for the Scanning Tunneling Microscope. *Physical Review Letters*, 50(25), 1998–2001.

Tersoff, J. & Hamann, D.R., (1985) Theory of the scanning tunneling microscope. *Physical Review B*, 31(2), 805–813.

Thole, B. et al., (1992) X-ray circular dichroism as a probe of orbital magnetization. *Physical Review Letters*, 68(12), 1943–1946.

Toader, M. et al., (2011) Initial growth of lutetium(III) bis-phthalocyanine on Ag(111) surface. *Journal of the American Chemical Society*, 133(14), 5538–44.

Troiani, F. et al., (2005) Molecular Engineering of Antiferromagnetic Rings for Quantum Computation. *Physical Review Letters*, 94(20), p.207208.

Uemura, Y. et al., (1985) Muon-spin relaxation in AuFe and CuMn spin glasses. *Physical Review B*, 31(1), 546–563.

Urdampilleta, M. et al., (2011) Supramolecular spin valves. *Nature materials*, 10(7), 502–6.

Villain, J. et al., (1994) Magnetic Relaxation in Big Magnetic Molecules. Europhysics Letters (EPL), 27(2), 159–164.

Voss, S. et al., (2008) A comparative study on the deposition of Mn12 single molecule magnets on the Au(111) surface. *Dalton transactions* , 7(4), 499–505.

Voss, S. et al., (2008) Investigation of the stability of Mn12 single molecule magnets. *Applied Physics A*, 94(3), 491–495.

Weinberg, W.H., (1978) Inelastic Electron Tunneling Spectroscopy: A Probe of the Vibrational Structure of Surface Species. *Annual Review of Physical Chemistry*, 29(1), 115–139.

Wende, H., (2004) Recent advances in x-ray absorption spectroscopy. *Report on Progress in Physics.*, 67(12), 2105–2181.

Wende, H. et al., (2007) Substrate-induced magnetic ordering and switching of iron porphyrin molecules. *Nature materials*, 6(7), 516–20.

Wu, R. & Freeman, A.J., (1994) Limitation of the Magnetic-Circular-Dichroism Spin Sum Rule for Transition Metals and Importance of the Magnetic Dipole Term Ruqian. *Physical Review Letters*, 73(14), 1994–1997.

Yamashita, T. & Hayes, P., (2008) Analysis of XPS spectra of Fe2+ and Fe3+ ions in oxide materials. *Applied Surface Science*, 254(8), 2441–2449.

Yeh, J.J., (1993) *Atomic Calculation of Photoionization Cross-Sections and Asymmetry Parameters*. Gordon and Breach Science Publishers.

Yeh, J.J. & Lindau, I., (1985) *Atomic Data and Nuclear Data Tables*. 32, 1-155.

Zhang, Y. et al., (2009) A Low-Temperature Scanning Tunneling Microscope Investigation of a Nonplanar Dysprosium - Phthalocyanine Adsorption on Au(111). *Journal of the American Chemical Society*, 113(111), 14407–14410.

Zhang, Y. & Yang, W., (1998) Comment on "Generalized Gradient Approximation Made Simple." *Physical Review Letters*, 80(4), 890–890.

Zhu, P. et al., (2004) Comparative Electrochemical Study of Unsubstituted and Substituted Bis(phthalocyaninato) Rare Earth(III) Complexes. *European Journal of Inorganic Chemistry*, 2004(3), 510–517.

Zyazin, A.S. et al., (2010) Electric field controlled magnetic anisotropy in a single molecule. *Nano letters*, 10(9), 3307–11.

Zyazin, A.S. et al., (2011) High-spin and magnetic anisotropy signatures in three-terminal transport through a single molecule. *Synthetic Metals*, 161(7-8), 591–597.

Acknowledgments

Ringrazio la Prof.ssa Sessoli per la grande passione che dedica alla ricerca e per la sua pazienza e disponibilità. Ringrazio i miei colleghi per il loro fondamentale contributo: Dr. Mannini, Dr.ssa Lanzilotto, Dr. Poggini, Cortigiani, Dr. Totti e Dr.ssa Ninova. Ringrazio il Prof. Caneschi per avermi dato la possibilità di far parte del LAboratorio di Magnetismo Molecolare (LAMM) e tutti coloro che del LAMM fanno parte.

I wish to thank Dr. Zaher and Dr. Hofmann of the Paul Scherrer Institute (PSI) for the muon spin relaxation measurements. I am also in debt to those who helped me during beamtimes at the SOLEIL synchrotron: Dr. Sainctavit, Dr. Ohresser, Dr. Otero and Dr. Choueikani. Thanks to Dr. Loth and Dr. Burgess (Max Planck Research Group - Dynamics of Nanoelectronic Systems in Hamburg) for the spin excitation measurements.

Ringrazio tutti gli amici che mi hanno supportato e sopportato in questi anni.

Infine un ringraziamento particolare a mia moglie e alla mia famiglia.

Luigi Malavolti, *Single molecule magnets sublimated on conducting and magnetic substrates*,
ISBN 978-88-6655-969-6 (print) ISBN 978-88-6655-970-2 (online)

PREMIO TESI DI DOTTORATO

ANNO 2007

Bracardi M., *La Materia e lo Spirito. Mario Ridolfi nel paesaggio umbro*

Coppi E., *Purines as Transmitter Molecules. Electrophysiological Studies on Purinergic Signalling in Different Cell Systems*

Mannini M., *Molecular Magnetic Materials on Solid Surfaces*

Natali I., *The Ur-Portrait.* Stephen Hero *ed il processo di creazione artistica in* A Portrait of the Artist as a Young Man

Petretto L., *Imprenditore ed Università nello start-up di impresa. Ruoli e relazioni critiche*

ANNO 2008

Bemporad F., *Folding and Aggregation Studies in the Acylphosphatase-Like Family*

Buono A., *Esercito, istituzioni, territorio. Alloggiamenti militari e «case Herme» nello Stato di Milano (secoli XVI e XVII)*

Castenasi S., *La finanza di progetto tra interesse pubblico e interessi privati*

Colica G., *Use of Microorganisms in the Removal of Pollutants from the Wastewater*

Gabbiani C., *Proteins as Possible Targets for Antitumor Metal Complexes: Biophysical Studies of their Interactions*

ANNO 2009

Decorosi F., *Studio di ceppi batterici per il biorisanamento di suoli contaminati da Cr(VI)*

Di Carlo P., *I Kalasha del Hindu Kush: ricerche linguistiche e antropologiche*

Di Patti F., *Finite-Size Effects in Stochastic Models of Population Dynamics: Applications to Biomedicine and Biology*

Inzitari M., *Determinants of Mobility Disability in Older Adults: Evidence from Population-Based Epidemiologic Studies*

Macrì F., *Verso un nuovo diritto penale sessuale. Diritto vivente, diritto comparato e prospettive di riforma della disciplina dei reati sessuali in Italia*

Pace R., *Identità e diritti delle donne. Per una cittadinanza di genere nella formazione*

Vignolini S., *Sub-Wavelength Probing and Modification of Complex Photonic Structures*

ANNO 2010

Fedi M., *«Tuo lumine». L'accademia dei Risvegliati e lo spettacolo a Pistoia tra Sei e Settecento*

Fondi M., *Bioinformatics of genome evolution: from ancestral to modern metabolism. Phylogenomics and comparative genomics to understand microbial evolution*

Marino E., *An Integrated Nonlinear Wind-Waves Model for Offshore Wind Turbines*

Orsi V., *Crisi e Rigenerazione nella valle dell'Alto Khabur (Siria). La produzione ceramica nel passaggio dal Bronzo Antico al Bronzo Medio*

Polito C., *Molecular imaging in Parkinson's disease*

Romano R., *Smart Skin Envelope. Integrazione architettonica di tecnologie dinamiche e innovative per il risparmio energetico*

ANNO 2011

Acciaioli S., *Il* trompe-l'œil *letterario, ovvero il sorriso ironico nell'opera di Wilhelm Hauff*

Bernacchioni C., *Sfingolipidi bioattivi e loro ruolo nell'azione biologica di fattori di crescita e citochine*

Fabbri N., *Bragg spectroscopy of quantum gases: Exploring physics in one dimension*

Gordillo Hervás R., *La construcción religiosa de la Hélade imperial: El Panhelenion*

Mugelli C., *Indipendenza e professionalità del giudice in Cina*

Pollastri S., *Il ruolo di TAF12B e UVR3 nel ciclo circadiano dei vegetali*

Salizzoni E., *Paesaggi Protetti. Laboratori di sperimentazione per il paesaggio costiero euro-mediterraneo*

ANNO 2012

Evangelisti E., *Structural and functional aspects of membranes: the involvement of lipid rafts in Alzheimer's disease pathogenesis. The interplay between protein oligomers and plasma membrane physicochemical features in determining cytotoxicity*

Bondì D., *Filosofia e storiografia nel dibattito anglo-americano sulla svolta linguistica*

Petrucci F., Petri Candidi Decembrii *Epistolarum iuvenilium libri octo*. A cura di Federico Petrucci

Alberti M., *La 'scoperta' dei disoccupati. Alle origini dell'indagine statistica sulla disoccupazione nell'Italia liberale (1893-1915)*

Gualdani R., *Using the Patch-Clamp technique to shed light on ion channels structure, function and pharmacology*

Adessi A., *Hydrogen production using Purple Non-Sulfur Bacteria (PNSB) cultivated under natural or artificial light conditions with synthetic or fermentation derived substrates*

Ramalli A., *Development of novel ultrasound techniques for imaging and elastography. From simulation to real-time implementation*

ANNO 2013

Lunghi C., *Early cross-modal interactions and adult human visual cortical plasticity revealed by binocular rivalry*

Brancasi I., *Architettura e Illuminismo. Filosofia e progetti di città nel tardo Settecento francese*

Cucinotta E., *Produzione poetica e storia nella prassi e nella teoria greca di età classica*

Pellegrini L., *Circostanze del reato: trasformazioni in atto e prospettive di riforma*

Locatelli M., *Mid infrared digital holography and terahertz imaging*

Muniz Miranda F., *Modelling of spectroscopic and structural properties using molecular dynamics*

Bacci M., *Coarse-grained molecular dynamics and continuum models for the transport of protein molecules*

Martelli R., *Characteristics of raw and cooked fillets in species of actual and potential interest for Italian aquaculture: rainbow trout (Oncorhynchus mykiss) and meagre (Argyrosomus regius)*

ANNO 2014

Lana D., *A study on cholinergic signal transduction pathways involved in short term and long term memory formation in the rat hippocampus. Molecular and cellular alterations underlying memory impairments in animal models of neurodegeneration*

Lopez Garcia A., *Los Auditoria de Roma y el Athenaeum de Adriano*

Pastorelli G., *L'immagine del cane in Franz Kafka*

Bussoletti A., *L'età berlusconiana. Il centro-destra dai poli alla Casa della Libertà 1994-2001*

Malavolti L., *Single molecule magnets sublimated on conducting and magnetic substrates*

Belingardi C., *Comunanze urbane. Autogestione e cura dei luoghi*

Guzzo E., *Il tombeau di Jean-Jacques Rousseau al Pantheon. Dalla capanna rustica di Vitruvio alla sua fortuna iconografica nella trattatistica fra XV e XVIII Secolo*